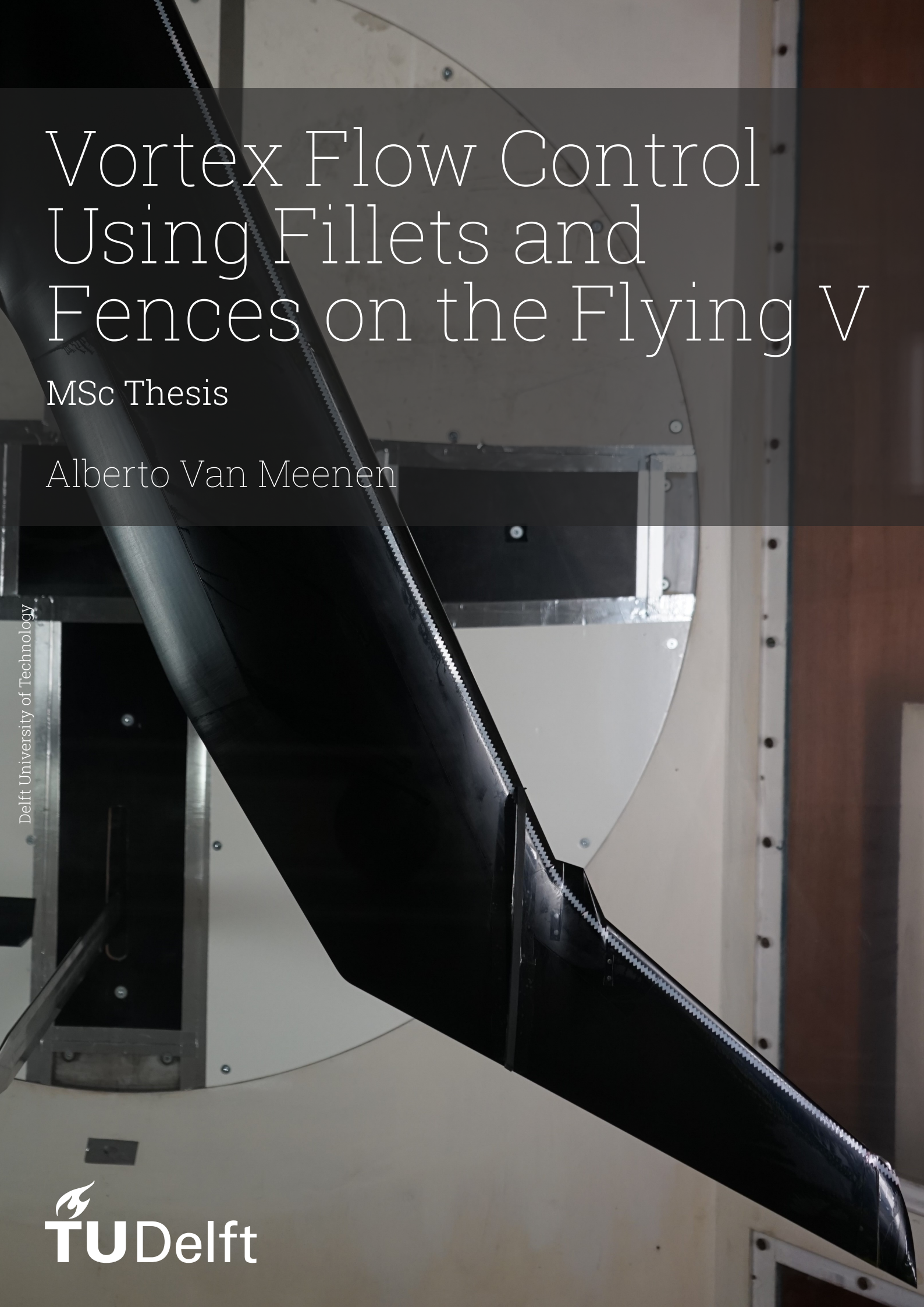

Vortex Flow Control Using Fillets and Fences on the Flying V

MSc Thesis

Alberto Van Meenen

Delft University of Technology

TU Delft

Vortex Flow Control Using Fillets and Fences on the Flying V

MSc Thesis

by

Alberto Van Meenen

To obtain the degree of Master of Science
at the Delft University of Technology,
to be defended publicly on Thursday December 12th, 2024

Student Number: 4674030
Thesis Duration: January, 2024 - December, 2024
Thesis Committee: Dr. F. Oliviero (Chair)
Dr. D. Ragni (Examiner)
Dr. ir. R. Vos (Supervisor)
Ir. N. van Luijk (Supervisor)

Cover: Flying V model in the wind tunnel in a configuration with diamond juncture fillet and fence
A digital version of this thesis is available at `http://repository.tudelft.nl/`

TU Delft

Preface

This research journey is driven by my passion for aviation. Concorde, whose groundbreaking design and supersonic capabilities demonstrated the immense potential of innovative aircraft technologies, inspired my exploration into sustainable aircraft designs like the Flying V. As I near the end of my academic career, this thesis marks a significant milestone in my personal and professional growth. With this work I am happy to contribute to the future of air travel. I would like to thank my supervisors, Dr. ir. R. Vos and N. van Luijk for the immense opportunity to carry out this experimental campaign on the Flying V.

Alberto Alessandro Van Meenen
Delft, December 2024

Abstract

The aviation industry faces increasing pressure to reduce its carbon emissions, with unconventional aircraft configurations like the Flying V emerging as a potential solution. With its passengers and cargo inside a V-shaped wing, the Flying V has the potential to decrease fuel consumption by up to 20%. However, a critical aerodynamic challenge for the Flying V is its unstable nose-up pitch tendency, which reduces the maximum usable lift coefficient and limits the aircraft's operational envelope. The reason for the abrupt change in pitching moment is not fully understood and necessitates wind tunnel experimentation to determine its cause and find ways to postpone the instability to higher angles of attack.

The literature study in this report explores the aerodynamic characteristics of flying wings such as the Flying V. The high sweep angle, blunt leading edge, and distinct kink in the planform of the Flying V results in a complex vortical flow field above the wing. The literature study further reveals that juncture fillets, which determine the transition between the inboard and outboard wing, could be a method to control the flow and help delay the pitch-break instability. Despite extensive research on double-delta wings, the application of juncture fillets to blunt-wing designs, such as the Flying V, remains unexplored, presenting an important research gap. Additionally, the installation of a full-chord fence in the kink region renews the boundary layer on the outboard wing, but could also realign the trajectory of leading edge vortices and reduce the interaction thereof. This could prove beneficial to increase lift on the wing outboard of the kink. This study thus aims to investigate the effects of juncture fillets and full-chord fences on the pitching moment behaviour and vortical flow structures, with the aim of delaying the pitch-break.

In the scientific article, parabolic and diamond juncture fillets, as well as full-chord fences at three spanwise locations in the kink region, are experimentally studied using a modular wind tunnel model. Stereoscopic Particle Image Velocimetry (SPIV) and oil flow visualization are used to analyse vortex behaviour and flow topology at high angles of attack. The results reveal that the parabolic fillet outperforms the diamond fillet at angles of attack above 15° by generating up to 7% more lift, maintaining stronger vortex structures and delaying vortex breakdown. While the diamond fillet reduces drag at lower angles of attack due to decreased flow separation on the outboard wing, it is less effective at improving lift at higher angles due to disrupted vortex feeding sheets. A full-chord fence reduces the outboard movement of inboard vortices by up to 11% span and promotes a stable vortex above the outboard wing. This, combined with a renewed boundary layer, improves lift on the outboard wing and leads to less fluctuations in the pitching moment. However, none of the tested configurations postpone the pitch-break angle. The results suggest that the instability at high angles of attack is primarily related to the forward movement of the inboard leading edge vortices.

The experimental measurements are limited by the use of a single SPIV plane, which limits the ability to observe the entire flow topology and vortex interactions. Future research could benefit from using multiple chordwise SPIV stations to better capture these phenomena and enhance the understanding of vortex interactions in the kink region of the wing. Further exploration of alternative leading edge geometries could provide insights into reducing the forward movement of the leading edge vortices inboard of the kink, improving the overall stability of the aircraft. Additionally, incorporating slats on the outboard wing could increase the stall angle and improve the maximum lift coefficient, helping to counteract the forward movement of the centre of pressure and improve the aircraft's operational capabilities. Overall, this research provides valuable insights into vortex control methods for unconventional aircraft designs and emphasises the importance of continued exploration into the complex flow phenomena surrounding blunt-nosed crescent wings.

Contents

List of Figures

Nomenclature

Abbreviations

Abbreviation	Definition
BWB	Blended Wing Body
CAD	Computer Aided Design
CFD	Computational Fluid Dynamics
CTW	Conventional Tube-and-Wing aircraft
CG	Center of Gravity
DOC	Direct Operating Cost
LEV	Leading Edge Vortex
LTT	Low Turbulence Tunnel
MAC	Mean Aerodynamic Chord
MTOW	Maximum Take-off Weight
NASA	National Aeronautics and Space Administration
OEW	Operative Empty Weight
RANS	Reynolds Averaged Navier-Stokes

Symbols

Symbol	Definition	Unit
a	Speed of Sound	[m/s]
c	chord length	[m]
c_{MAC}	Mean Aerodynamic Chord length	[m]
C_D	Drag coefficient	[-]
C_L	Lift coefficient	[-]
C_M	Moment coefficient	[-]
Re	Reynolds Number	[-]
S	Surface Area	[m^2]
S_{wet}	Wetted Surface Area	[m^2]
v	Velocity	[m/s]
v_{app}	Approach velocity	[m/s]
α	Angle of attack	[deg]
β	Angle of sideslip	[deg]
ρ	Density	[kg/m^3]
μ	Dynamic viscosity	[m^2/s]

Part I

Scientific Article

Vortex Flow Control Using Fillets and Fences on the Flying V

A.A. Van Meenen*
Delft University of Technology, Delft, 2629HS, The Netherlands

The aviation industry is exploring unconventional aircraft designs like the Flying V in its drive to reduce carbon emissions and improve fuel efficiency. The Flying V, featuring a crescent wing with leading edge kink, currently suffers from an unstable nose-up pitch tendency. This study investigates vortex control methods within this kink region to increase lift on the outboard wing and delay the pitch-break. A full-span, modular wind tunnel model is used to investigate the effects of parabolic and diamond juncture fillets, as well as full-chord fences, on the pitching moment characteristics. Stereoscopic Particle Image Velocimetry (SPIV) and oil flow visualization are used to analyse vortex behaviour and flow topology. Results reveal that the parabolic fillet outperforms the diamond fillet in generating lift at higher angles of attack due to its ability to promote vortex formation and delay breakdown. The installation of full-chord fences increases lift on the outboard wing and positively influences the pitching moment, though none of the tested configurations increased the pitch-break angle.

Nomenclature

α	=	Angle of attack [°]
$\bar{c}$	=	Mean aerodynamic chord [m]
b	=	Semi span [m]
C_D	=	Drag Coefficient [-]
C_L	=	Lift Coefficient [-]
C_M	=	Pitching Moment Coefficient (+ up) [-]
M	=	Mach Number [-]
Re	=	Reynolds Number [-]
u_∞	=	Free-stream velocity $[m/s]$
ω_x	=	Vorticity in x-direction $[s^{-1}]$
x	=	Chordwise coordinate [m]
y	=	Spanwise coordinate [m]
z	=	Normal coordinate [m]

Abbreviations

DF	=	Diamond Fillet
LEV	=	Leading edge vortex
OBV	=	Outboard wing vortex
PF	=	Parabolic Fillet

I. Introduction

The aviation sector, responsible for up to 3.5% of global carbon emissions, faces increasing regulatory pressure to meet net-zero targets worldwide [1, 2]. Up to 149 countries have set net-zero targets and given this legal climate, the need for sustainable aircraft is larger than ever [3]. Conventional tube-and-wing aircraft have reached a plateau in terms of aerodynamic efficiency, with efficiency gains in the order of a few percent over the last two decades [4, p 125]. In order to substantially reduce carbon emissions, researchers have turned to new, unconventional configurations such as flying wings and blended-wing-bodies [5]. One of these, the Flying V, is a novel flying wing design developed at the Delft University of Technology. The aircraft has the potential to reduce fuel consumption and carbon emissions by up to 20% compared to tube-and-wing aircraft [6]. This is achieved through a V-shaped configuration that integrates the passenger cabin and cargo space within the wing structure. However, the aircraft's unique shape and configuration introduce aerodynamic challenges, particularly in terms of stability and control. At pitch angles above 19°, the Flying V experiences an unstable nose-up pitch tendency [6, 7]. This reduces the maximum usable lift coefficient and results in a longer take-off and landing field length, harming the aircraft's operational capabilities.

The reason for the abrupt change in pitching moment is not fully understood and necessitates wind tunnel experimentation to determine its cause and find ways to postpone the instability to higher angles of attack. Based on previous research by Viet [7], numerous leading edge vortices dominate the flow field around the Flying V. It is suspected that vortex breakdown over the wings may contribute to the pitch-break phenomenon, yet conclusive evidence is lacking. Therefore, there is a need for research to delve into the origins of this issue and propose possible solutions.

*MSc Student, Flight Performance and Propulsion, Delft University of Technology

The Flying V's unique crescent wing results in a distinct kink in the leading edge. Based on literature, a geometric modification in this kink region, a so-called wing juncture fillet, could be a solution to postpone this pitch-break [8]. The shape of this fillet, which defines the transition between the inboard and outboard wing, could affect vortex breakdown phenomena. The effects of juncture fillets on vortex behaviour have been studied extensively for sharp-edged, double-delta wings, by Kern [8] and Hebbar [9–11]. Their findings indicate that shapes like parabolic and diamond fillets can increase lift and delay vortex breakdown. However, the Flying V features a blunt leading edge, driven by the required space within the passenger cabin. The impact of such modifications on blunt-nosed, crescent wings remains unexplored. This study addresses this gap by examining the effects of both parabolic and diamond juncture fillets on vortex structures and pitching moment behaviour for blunt-nosed crescent wings.

Additionally, the Flying V experiences a significant spanwise flow component along the surface [7]. This spanwise cross-flow affects the lifting capability of the outboard wing and could also contribute to the pitch-break. Therefore, in previous research, van Uitert [12] experimented with multiple spanwise locations and fence types. Only the installation of a full-chord fence in the kink region resulted in an increase in lift on the outboard wing and a favourable pitching moment behaviour. However, the effects on the vortical flow field over the Flying V were not investigated. Based on literature, a fence in the wing kink could re-align the trajectory of vortices and reduce the coupling between inboard and outboard vortices, as was found in research on the F16-XL [13, 14]. In order to further examine the effects of a full-chord fence on the flow field, three different spanwise fence locations are tested in the vicinity of the optimal location identified by van Uitert. This determines the relationship between fence location, pitch-break angle and vortical flow topology.

By understanding the effects of these geometric modifications on the vortical flow structures, the study seeks to identify configurations that can increase the maximum usable lift coefficient and delay pitch-break, ultimately improving the stability and performance of the Flying V. Given the novelty of applying juncture fillets to wings with blunt leading edges, the outcome of this research is vital to the feasibility and sustainability of flying wing configurations. This paper begins with presenting the model and experimental techniques in section II, followed by a discussion of the results in section III and ending with the conclusions in section IV.

II. Experimental Setup

A. Wind Tunnel Model

For experimentation with different wing geometries, a full-span modular wind tunnel model was made. The wind tunnel model is based on the aerodynamic optimisation of the FV-1000 by Laar [15, 16]. It has a scale of 1/54 and features interchangeable leading and trailing edges. The dimensions of the wind tunnel model are presented in Figure 1, including the juncture fillet and fence geometries.

1. Wing Juncture Fillets

The unmodified wing features a parabolic juncture fillet. The experimentation with different juncture fillets has been carried out extensively on double delta wings with sharp leading edges such as in the works of Kern, Gonzalez and Hebbar [8–11, 17–19]. There, the parabolic fillet (PF) and diamond fillet (DF) were found the most promising in terms of delaying vortex breakdown and increasing the lift coefficient. In order to compare the performance of these on a blunt-nosed crescent wing, a new diamond fillet is designed and manufactured. The geometry of the diamond fillet is presented in Figure 1 and is based on the geometry of Kern [17]. The diamond fillet has a 50% smaller leading edge radius compared to the parabolic fillet and adds 0.65% extra planform surface area in total. The juncture fillet was interchanged during the wind tunnel test campaign to evaluate the relative changes in the vortical structures for the parabolic and diamond fillets.

2. Boundary Layer Fences

The experimentation with wing fences on the Flying V is documented in the work of van Uitert [12] and serves as the baseline for this work. In that study, multiple fences with different geometry, height and spanwise location were tested. Of all the tested configurations, only a full-chord fence in the kink of the wing resulted in an improvement in lift and a smoothening of the pitching moment irregularities. Therefore, in order to further examine the effects of fences on

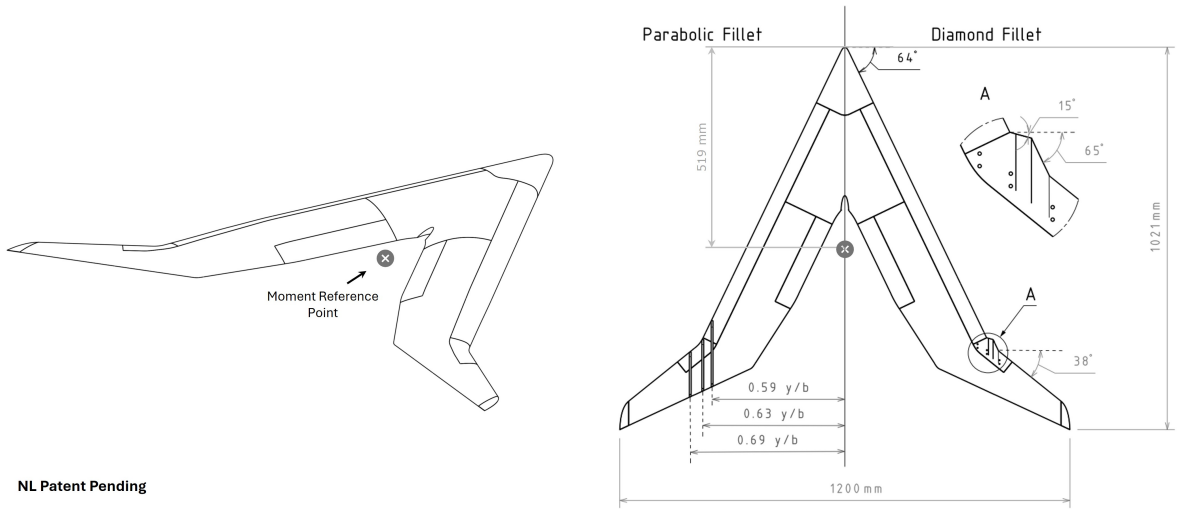

Fig. 1 Top View of the Flying V wind tunnel model with fences and interchangeable juncture fillet (base geometry from Laar et al [16]).

the vortical flow structures in this study, three full-chord fences were installed in this kink region. The fence locations are positioned slightly inboard and outboard of the optimal fence location identified by van Uitert with the locations documented in Figure 1.

The fences are fabricated using a 3D print and are installed on the model. They have a height of 60% thickness-to-chord ratio, similar to fences used in other experiments [20, 21], and a width of 5 mm for structural rigidity. The fence is expected to stop the boundary layer cross-flow to the tip region, thereby renewing the boundary layer and reducing separation which consequently increases the stall angle and enhances the lifting capability of the outboard wing [22]. Furthermore, the wing fence could also realign the trajectory of the vortices and sweep those downstream, thereby leaving more room for an outboard vortex to grow or make the outboard vortex less dependent on the inboard vortices. This could also result in an increase of vortex lift over the outboard wing. [13, 23]

B. Experimental Techniques

Wind tunnel tests are conducted at the low turbulence tunnel (LTT) at the Delft University of Technology. This low speed low turbulence wind tunnel operates as a closed-throat, single-return atmospheric tunnel. The tunnel has a divergent test section that is 2.60 m long with a 1.80 m x 1.25 m octogonal cross section. The tunnel's contraction ratio of 17.8 yields minimal free-stream turbulence levels as little as 0.015% at 20 m/s and 0.07% at 75 m/s [24]. The test section is interchangeable, which allows for the test section to be prepared while the tunnel remains operational. The facility is equipped with a 6-component force balance and Particle Image Velocimetry (PIV) systems. The measurements were conducted at 35 m/s ($M = 0.1$), resulting in a MAC based Reynolds number of $Re \approx 8 \cdot 10^5$. The maximum angle of attack is restricted by balance limits to 27°. All force balance measurements are repeated at least twice with good measurement agreement. No wall corrections are applied to the force balance results since no accurate corrections are available. Trip strips are installed on the model at 5% of the chord on the suction side and at 10% of the chord on the pressure side.

1. Surface Oil Flow Visualisation

Oil flow visualisation experiments are used to identify and characterise the different flow structures on the wing's suction surface. A thin film of paraffin oil is applied to the model's suction side using a paintbrush. A small amount of fluorescent droplets are dispersed into the oil prior to application. The oil is illuminated using three ultraviolet (UV) lamps positioned under the test section. Images are captured using a UV filter to reduce the glare and reflections of the UV lights into the lens. Three images are acquired per measurement, starting 3 minutes after the tunnel has reached its free-stream velocity of 35 m/s, with intervals of 30 s. This timing is determined from trial runs to evaluate the settling

time of the flow and the oil. The oil is redistributed for every measurement and the model is wiped clean and a new oil film is applied every 2 measurements. Since oil has a large viscosity, the oil flow is dominated by the viscous forces between the air and oil. The oil flow provides a qualitative representation of the flow features such as attached flow, separated flow and vortices in close proximity of the wing's surface. It allows to trace the trajectory of these vortices and could potentially show signs indicative of vortex breakdown should that occur close to the wing surface [25].

2. Stereoscopic Particle Image Velocimetry

Stereoscopic Particle Image Velocimetry (SPIV) is used to determine the flow field in the wake of the model. The method is capable of measuring both in-plane as well as out-of-plane velocity components. These are used to quantify the vorticity and detect breakdown based on vortex detection criteria (Q-criterion, Lambda2-criterion) and the velocity deficit in the vortex core. The velocity components are used to quantify the differences in vortex topology between model configurations. Figure 2 presents the PIV setup as seen from within the test section. Since the model hangs upside down in the test section, the region of interest lies under the wing (red). The measurement plane is aligned normal to the free-stream flow and positioned 10 mm behind the wingtip and 120 mm inboard of the tip, placing it centrally behind the kink region (Figure 3). An Evergreen double-pulse Nd:YAG laser with wavelength of 532 nm is placed under the test section to cast a laser beam upwards illuminating the seeding particles. The PIV setup is fixed with respect to the test section and does not rotate with increasing angle-of-attack. This limitation means the model is tilted and displaced with respect to the measurement plane for increasing α.

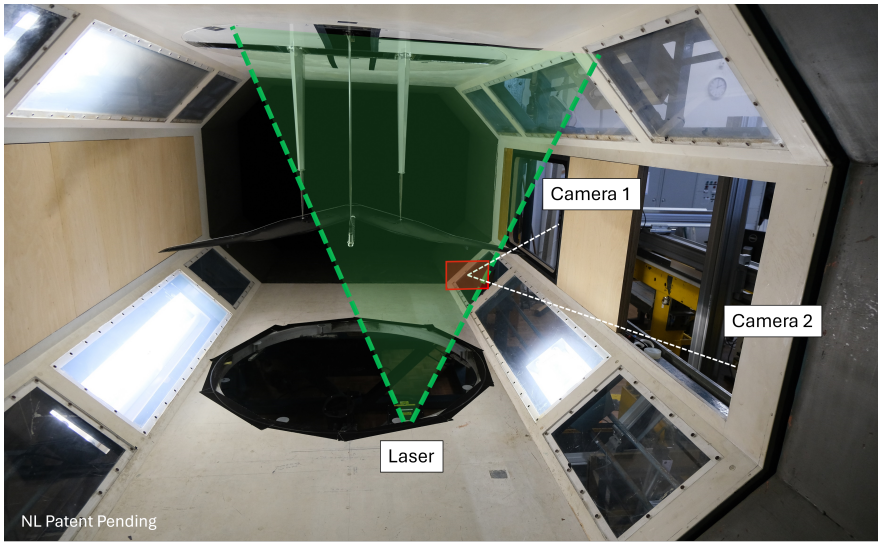

Fig. 2 Test Section with Stereoscopic PIV layout. Red region is the measurement plane.

Up- and downstream of the measurement plane, two scientific complementary metal oxide semiconductor (sCMOS) cameras with a resolution of 2560 × 2160 pixels are installed. The sCMOS camera sensors are tilted by Scheimpflug adapters to ensure the entire measurement plane remains in focus. Seeding particles, approximately $\approx 1\mu m$ in diameter, are introduced into the flow downstream of the test section to achieve uniform dispersion. Each camera captures 200 image pairs for each measurement point at a sampling frequency of f=15 Hz. The image pairs are processed using a 16-pixel interrogation window with 75% overlap. The presented results are based on the averaged flow fields determined by these 200 samples. The standard deviations of the mean free-stream velocity components are found to be smaller than 0.05 U_∞ with this setup.

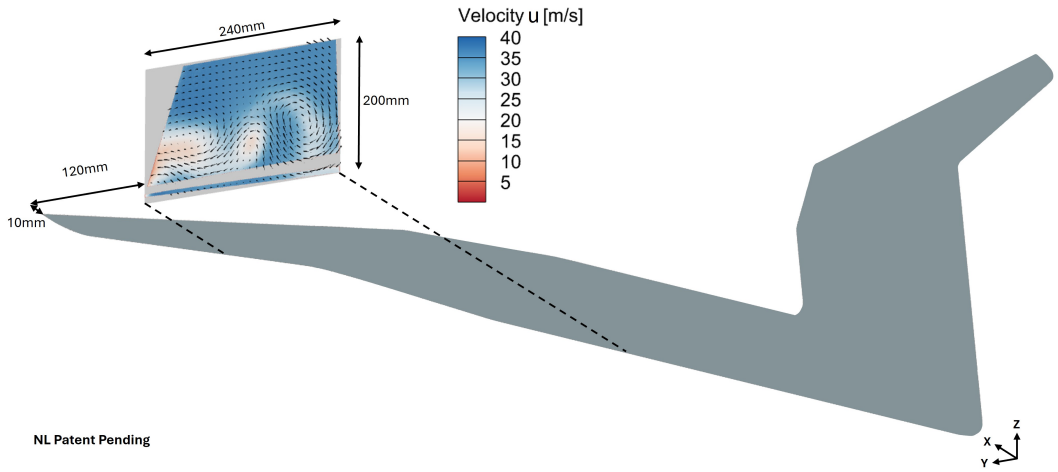

Fig. 3 Location of the PIV measurement plane with through-plane velocity contours for Parabolic Fillet at $\alpha = 15°$ (geometry from Laar et al [16]).

III. Results & Discussion

The flow topology over a highly swept, blunt-nosed wing is dominated by an intricate interaction of vortical flow structures [26]. The crescent wing has a distinct kink in the leading edge and the effects of this shape on the flow have not yet been thoroughly investigated. In this section the effects of the juncture fillet and wing fences on the flow in this kink region are analysed with the help of oil flow visualisation and particle image velocimetry using the Flying V geometry. Differences in the pitching moment are subsequently connected to changes in the flow topology for each configuration. The origin of the coordinate system for all contour plots is located at the aircraft's nose as presented in Figure 3. It is fixed with the wind tunnel test section and does not rotate with changing α. All PIV results are presented in front view. First, the results for the unmodified wing are discussed. Then, the results of the diamond fillet and wing fences are compared to this case.

A. Baseline Wing: Parabolic Juncture Fillet

Figure 4 presents the normalised axial vorticity fields for the baseline wing at $\alpha = 12.5°$ and $\alpha = 15°$ in the wake of the model. This shows the presence of two leading edge vortices; V1 and V2. V1 forms gradually starting from $\alpha = 10°$ out of a region of high vorticity midchord above the inboard wing, and its vorticity grows with increasing α. V2 originates just before the leading edge kink and has a smaller core radius compared to V1 as evident from the PIV results. In the oil flow, V2 can also be distinguished thanks to its separation line (S_2) as seen in Figure 5 (top left). This resulting double-vortex system on the inboard wing has also been identified on other blunt nosed, highly-swept wings [26–28]. The flow topology over the baseline wing is thus dominated by two co-rotating primary vortices above the inboard wing. Between those vortices, there is a trailing edge vortex (TEV). This vortex forms along the trailing edge of the inboard wing and rotates in opposite direction to the leading edge vortices. It is hypothesized that the TEV detaches from the wing at the kink of the trailing edge and passes underneath V1 resulting in its position between V1 and V2 as seen in Figure 4 and all consecutive PIV results. Additionally, all vortices move outboard with increasing angle of attack.

As evident from the oil flow in Figure 5, at $\alpha = 12.5°$, a clear footprint of a vortex becomes visible above the outboard wing. This outboard vortex (OBV) leaves an S-shaped pattern on the surface with its vorticity fed from the leading edge just after the kink. Moving to $\alpha = 15°$ (Figure 6), the footprint of the OBV is now gone, either because the OBV is no longer close to the surface, or because it has burst. The PIV data does not capture this outboard vortex as its trajectory falls outside the measurement plane.

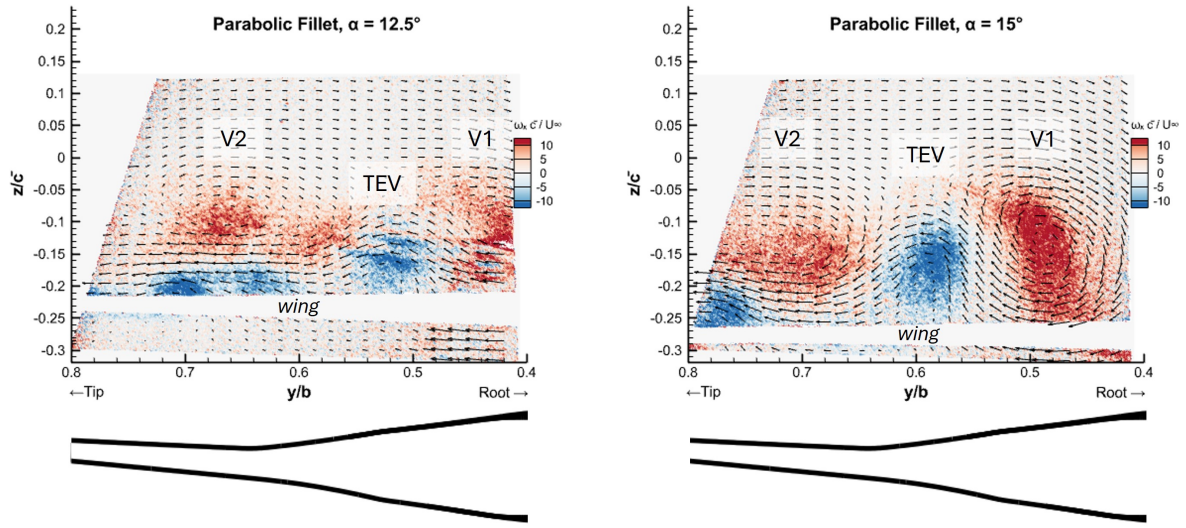

Fig. 4 Vorticity contour for the baseline wing at $\alpha = 12.5°$ and $\alpha = 15°$.

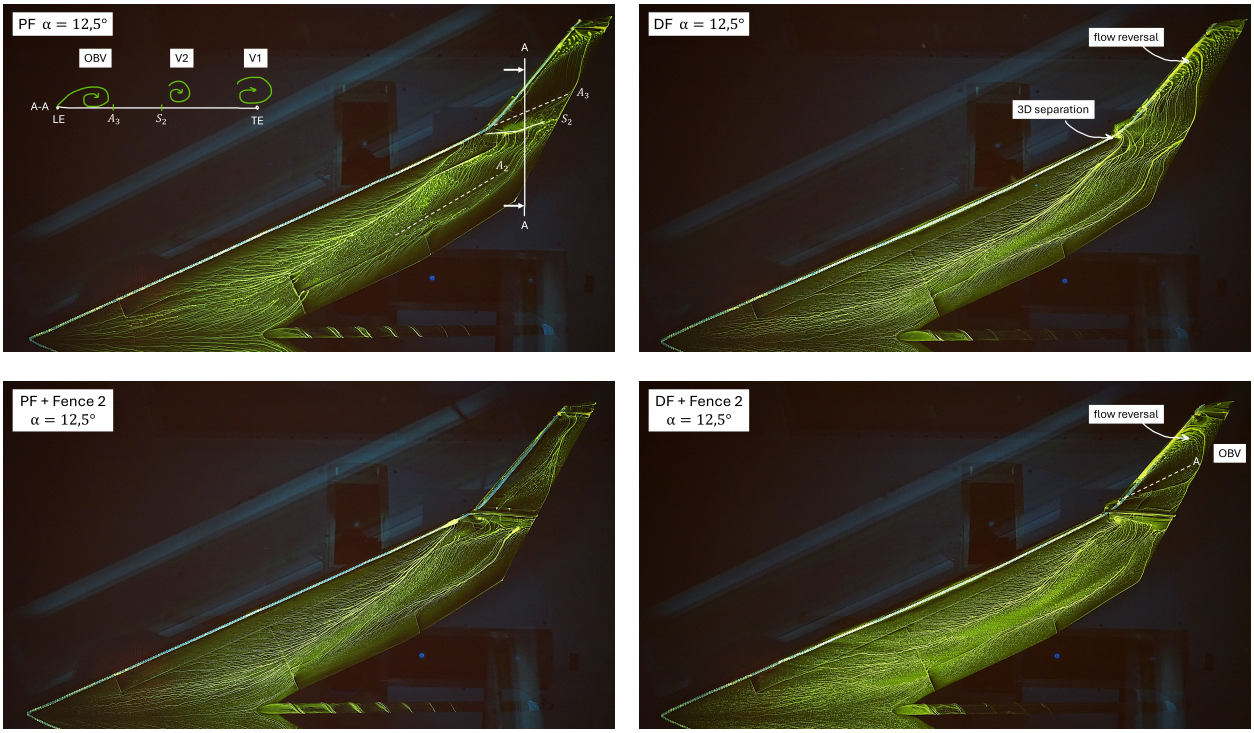

Fig. 5 Oil flow visualisation for all configurations at $\alpha = 12.5°$.

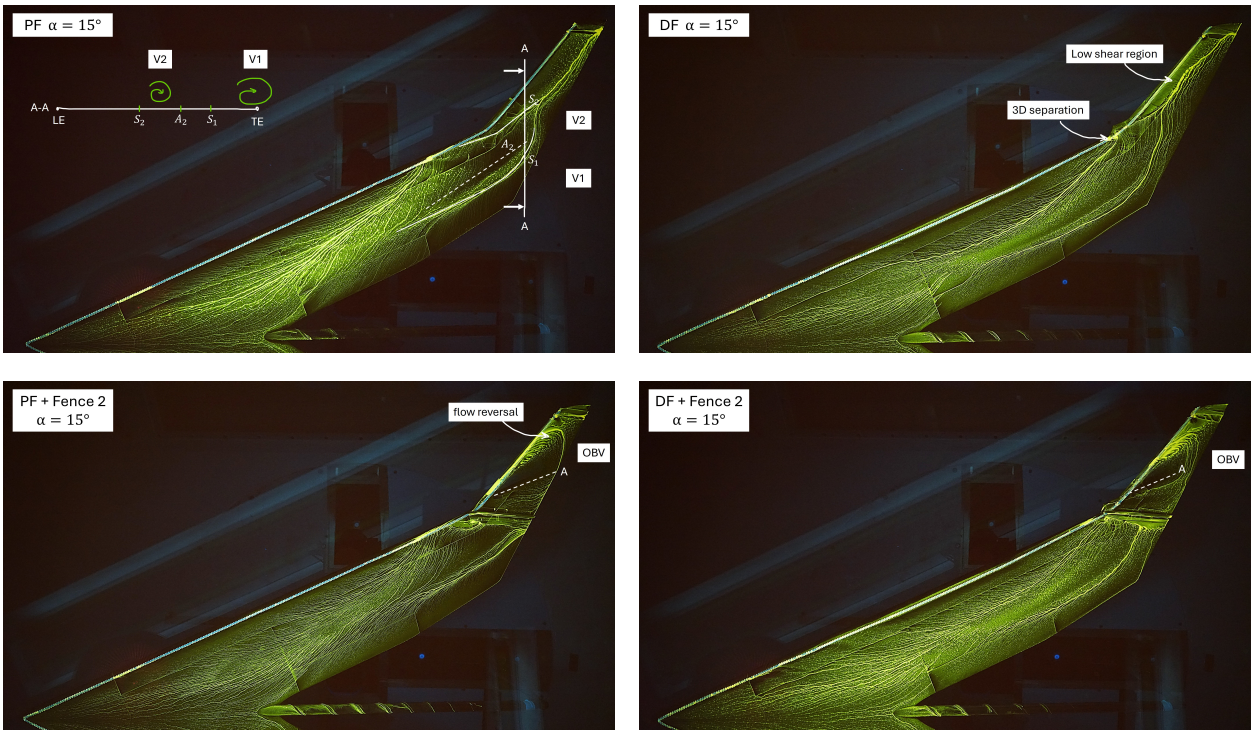

Fig. 6 Oil flow visualisation for all configurations at $\alpha = 15°$.

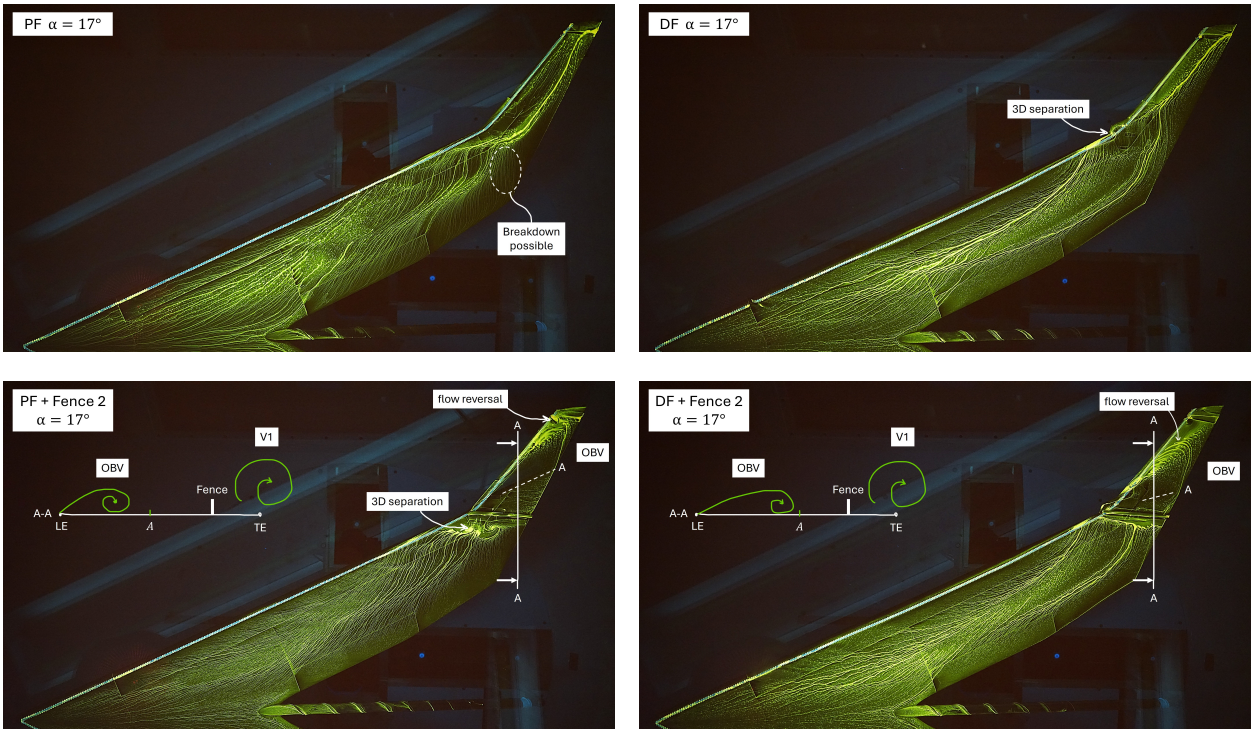

Fig. 7 Oil flow visualisation for all configurations at $\alpha = 17°$.

With increasing α, the inboard vortices are found to move forward both towards the nose of the aircraft and forward towards the leading edge, until at $\alpha = 17°$, there is a change in the topology (Figure 7). V1 is assumed to be undergoing vortex breakdown, supported by the sudden decelerated axial velocity from $1u_\infty$ to $0.2u_\infty$ and the movement of the vortex core away from the wing surface as visible in Figure 8. With the onset of vortex breakdown, the vorticity of V1 disperses over a larger region (Figure 9), reducing its ability to generate significant shear stress on the wing surface. This is evident in the oil flow visualisation, where the dark region above the kink fades. It is likely that V2 is affected by the breakdown of V1, and that these vortices are potentially merging behind the wing. This cannot be concluded with certainty given the obtained data. It is likely that breakdown moves forward with increasing α and affects an increasingly larger region of the wing.

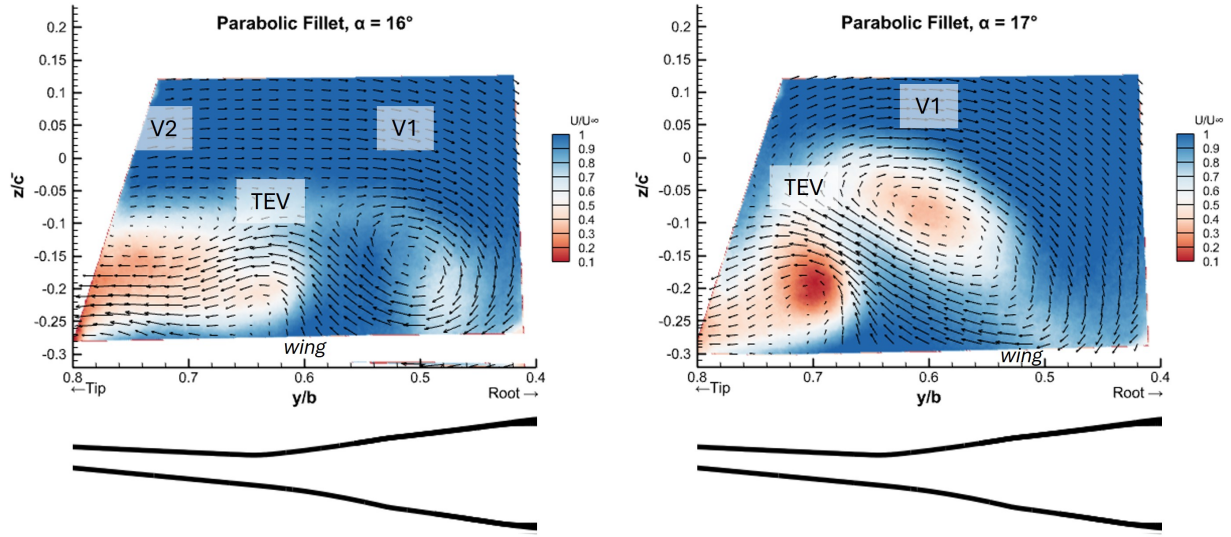

Fig. 8 Out-of-plane velocity contour at $\alpha = 16°$ and $\alpha = 17°$.

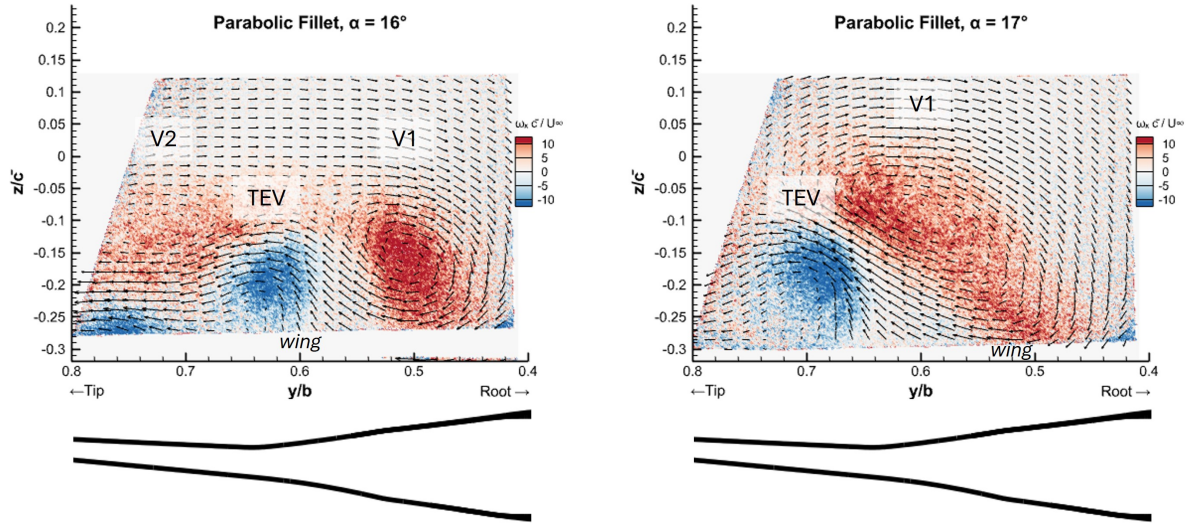

Fig. 9 Vorticity contour for the baseline wing at $\alpha = 16°$ and $\alpha = 17°$.

On the outboard wing, at $\alpha = 17°$, a dark region extends from the kink towards the tip, approximately at quarter-chord (see Figure 7). Dark regions in the oil flow visualisation indicate areas of increased shear stress between the oil and the airflow, resulting from a high local flow velocity. It is uncertain if this increased velocity along the surface is the result of a leading-edge vortex in this region, or simply due to attached flow. However, it is likely that a vortex resides above the outboard wing given slight traces of an attachment line in the oil flow photos at $\alpha = 19°$ and $\alpha = 20°$ (Figure 10). Regardless of its origin, the dark area is indicative of an area of low pressure and thus likely to increase lift.

Increasing α to 20°, the breakdown location of the inboard vortices moves forward and simultaneously all vortices move away from the wing surface as seen by the reduced vortex footprint in the oil flow. Post-breakdown, the core velocity of V1 recovers to the free-stream velocity in the wake of the wing. On the oil flow in Figure 10, the region of high-shear surface flow in streamwise direction over the leading edge of the inboard wing is no longer identifiable compared to lower angles of attack ($\alpha < 17°$). This, combined with typical s-shaped streamlines, could be indicative of one large leading edge vortex that spans the entire suction surface with its separation starting at the leading edge. On the outboard wing, the region of high shear remains in place.

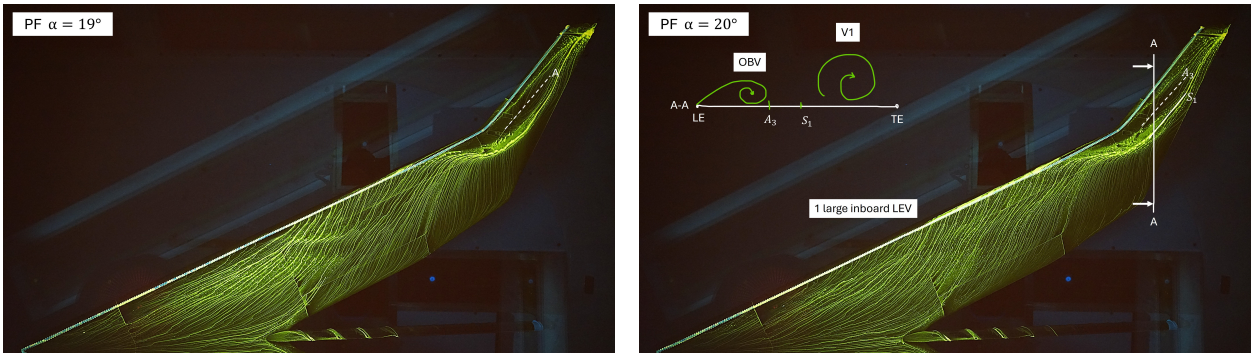

Fig. 10 Oil flow visualisation for Parabolic Fillet at $\alpha = 19°$ and $\alpha = 20°$.

B. Effects of Diamond Fillet

The diamond fillet, characterized by its sharper leading-edge geometry compared to the parabolic fillet, introduces aerodynamic effects on the Flying V. This section first explores how the diamond fillet influences the vortex topology, followed by its effects on the forces and moments data. The results are compared to the baseline case.

1. Flow Topology

The addition of the diamond fillet impacts the flow characteristics on both the inboard and outboard wing regions. On the inboard wing, the diamond fillet influences the location, vorticity and core velocities of the leading edge vortices. Firstly, it reduces V2's core velocity and disperses its vorticity compared to the parabolic fillet, resulting in a weaker vortex. This difference is evident at $\alpha = 12.5°$, where the core velocity of V2 with the diamond fillet is only 20% of the freestream velocity (u_∞) as opposed to 50% of u_∞ for the wing with parabolic fillet (see Figure 11). Due to its reduced core velocity, the trajectory of V2 is more affected by the low pressure field above the wing and is consequently located more outboard by +6.5% y/b compared to the wing with parabolic fillet. Secondly, the location of V1 is moved outboard by 2% y/b and its vorticity is more dispersed compared to the parabolic fillet. This is visible in the vorticity distribution at $\alpha = 15°$ (Figure 12). At $\alpha = 16°$, the diamond fillet results in an earlier breakdown of V1 than the parabolic fillet as supported by the sudden change in velocity and vorticity distributions in Figure 13 and Figure 14 which are further supported by vortex detection criteria. This change is similar to the breakdown of the parabolic fillet, but at $\alpha = 16°$ instead of $\alpha = 17°$.

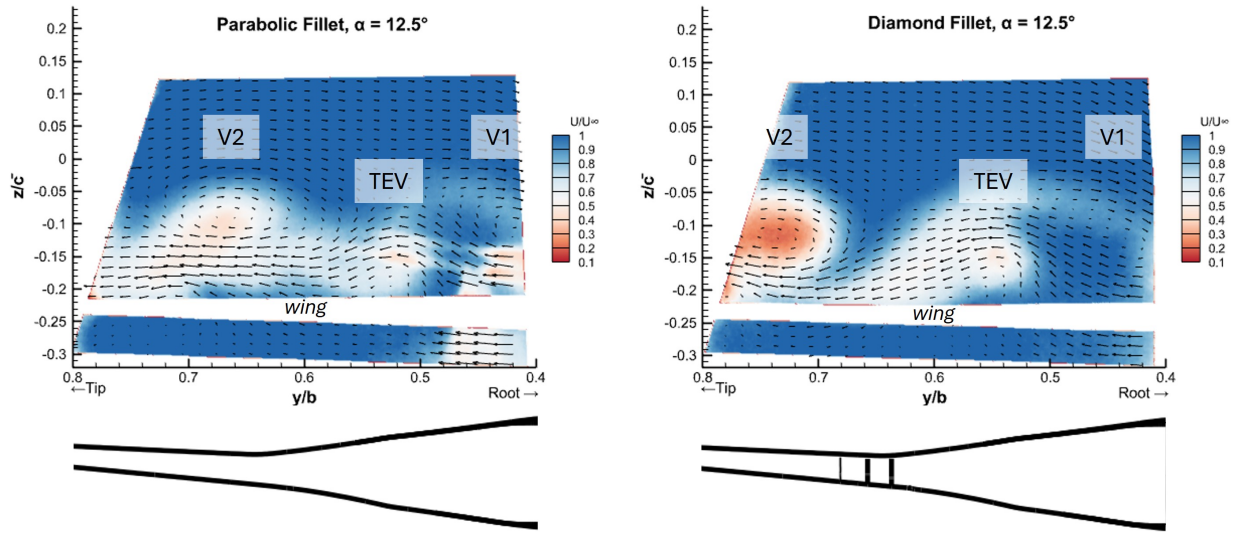

Fig. 11 Out-of-plane velocity contour for parabolic fillet and diamond fillet (α = 12.5°).

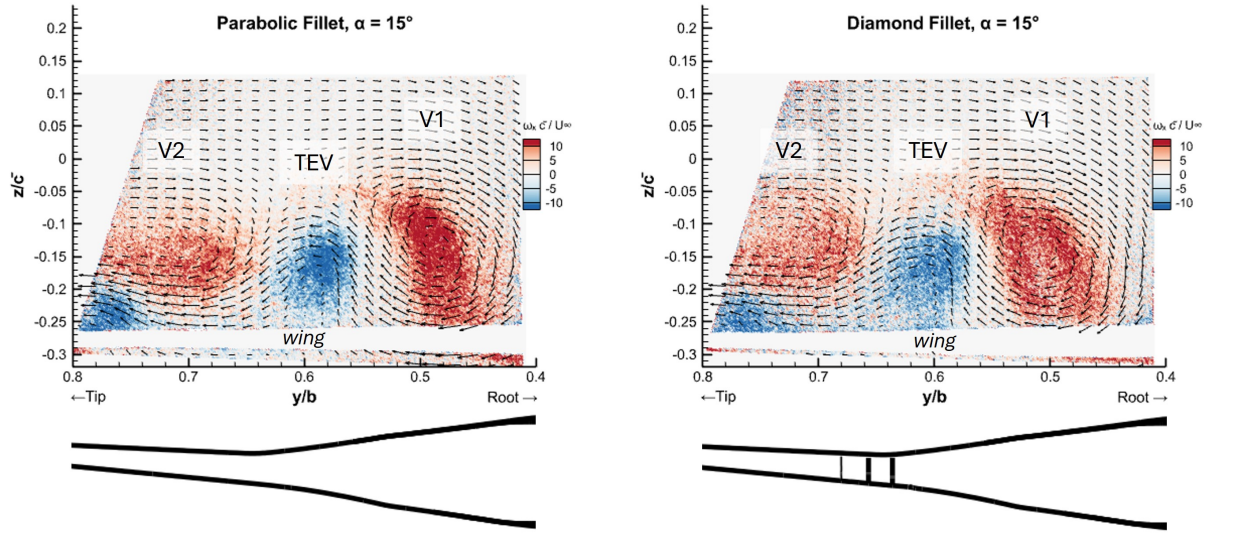

Fig. 12 Vorticity contour for parabolic fillet and diamond fillet (α = 15°).

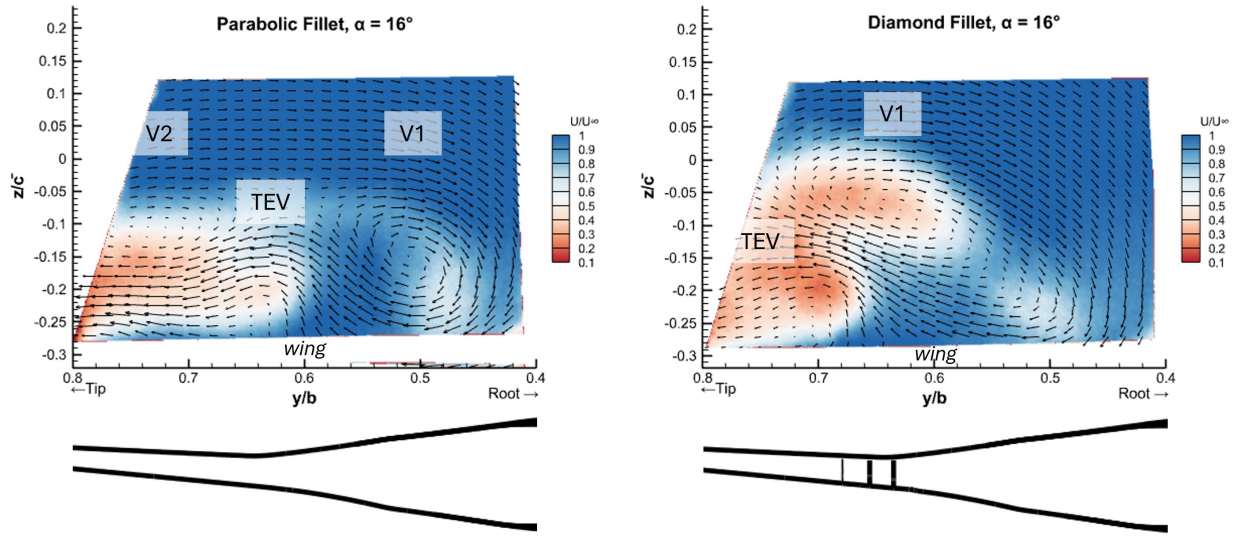

Fig. 13 Out-of-plane velocity contour for parabolic fillet and diamond fillet ($\alpha = 16°$).

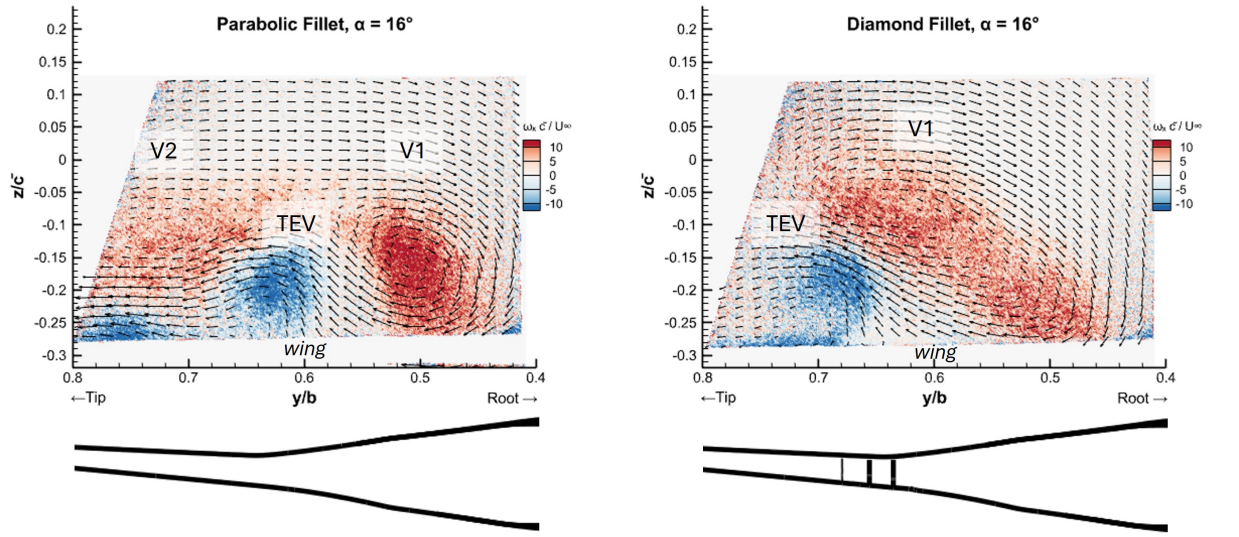

Fig. 14 Vorticity contour for parabolic fillet and diamond fillet ($\alpha = 16°$).

In addition to the effects on the leading edge vortices, the wing with diamond fillet features a 3D-type separation which appears at the location where there is an abrupt change in sweep angle. There, the flow along the leading edge of the inboard wing hits the sharp change in sweep of the diamond fillet, and locally leaves the surface as seen in the oil flow in Figure 15. The formation of this 3D-type separation occurs at approximately $\alpha = 10°$ and removes a portion of the boundary layer flow of the inboard wing. As a result of this disposition of boundary layer material, the outboard wing experiences less boundary layer cross-flow towards the tip compared to the wing with parabolic fillet at moderate angles of attack ($\alpha < 15°$). This reduction in boundary layer cross-flow is clearly distinguishable in the oil flow photos at $\alpha = 10°$ (Figure 15), where only one-third of the chord on the wing with the diamond fillet is affected by cross-flow at the kink region, compared to three-quarters of the chord with the parabolic fillet. The combined effects of this 3D separation and the diamond fillet's reduced thickness-to-chord ratio result in a larger portion of attached flow on the outboard wing. This results in an increase in lift for the wing with diamond fillet for $7° < \alpha < 13°$ as shown by the lift coefficient data in Figure 16.

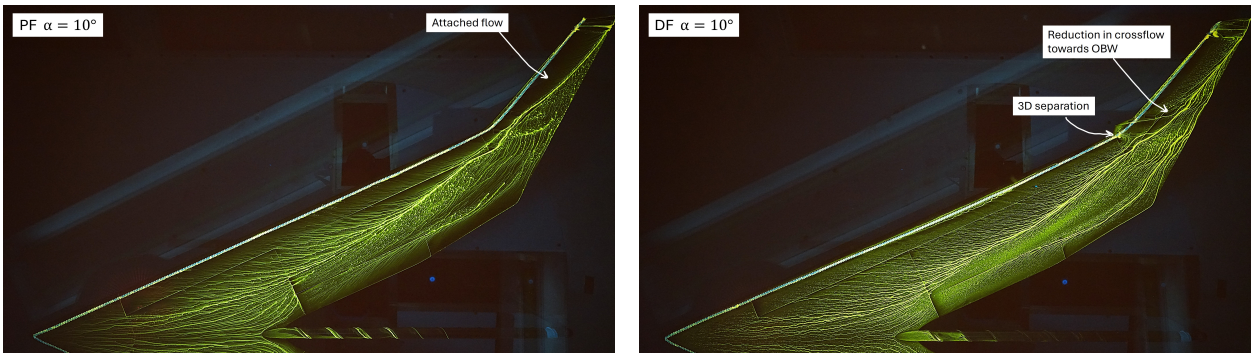

Fig. 15 Oil flow visualisation for Parabolic Fillet and Diamond Fillet at $\alpha = 10°$.

At higher angles of attack ($\alpha > 17°$), the diamond fillet suppresses the formation of a high-shear region on the outboard wing, unlike the parabolic fillet (see Figure 7). This could be caused by the disruption of the vortex feeding sheet from the inboard wing to the outboard wing. Subsequent oil flow photos with increasing α show no clear outboard wing vortex. This stands in strong contrast to the flow around the parabolic fillet. There, the smooth transition of wing sweep ensures that the leading edge vortex near the kink (V2) is swept outboard and potentially strengthens any weak vortex above the outboard wing. The resulting dark high-shear region spans a large portion of the wing surface. This behaviour aligns with findings from Kern [8, 17], which indicate that the parabolic fillet enhances lift over the outboard wing by combining vortex feeding sheets from both the inboard and outboard leading edges. As a result, the parabolic fillet generates more lift above the outboard wing at large angles of attack ($\alpha > 15°$), as reflected in the lift curve (Figure 16). Thus, while the wing with diamond fillet features a larger portion of attached flow over the outboard wing for moderate angles of attack, it is not capable of producing the same amount of lift as the parabolic fillet at large angles of attack.

2. Lift, Drag & Pitching Moment

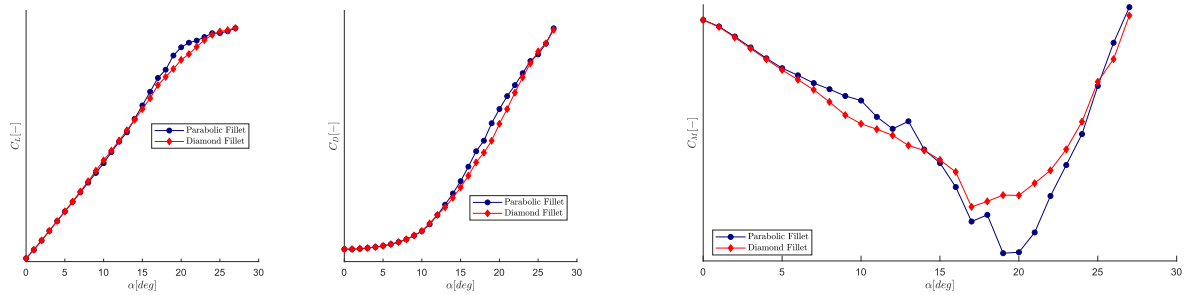

Fig. 16 Lift, Drag and Pitching Moment Coefficient for Parabolic and Diamond Fillet.

Figure 16 presents the forces measured with the force balance. The leading edge of the mean aerodynamic chord serves as the pitching moment reference point ($x_{ref} = x_{LEMAC}$). The lift coefficient is slightly larger for the diamond fillet between $7° < \alpha < 13°$ but is larger for the parabolic fillet between $13° < \alpha < 25°$ by up to 7% at $\alpha = 19°$. The diamond fillet performs better at lower α due to its reduction in flow separation on the outboard wing. This results in more lift on the outboard wing and a steeper moment coefficient gradient initially. The parabolic fillet however outperforms the diamond fillet at higher α due to the formation of a high-lift region near the kink as evident by the dark region in the oil flow, either due to additional vorticity or due to high-speed attached flow. This could not be confirmed with the captured data. The high-lift is also reflected in the pitching moment, where the parabolic fillet attains the smallest C_M. The diamond fillet generates less drag between $4° < \alpha < 25°$ due to a reduction in pressure drag associated with the smaller region of separated flow. However, at zero lift, there is 0.75% more parasite drag due to the increase in wetted surface area of the diamond fillet. Overall, the maximum lift-to-drag ratio of the diamond fillet is 1.5% higher than the parabolic fillet in the tested conditions.

The temporary decrease in the pitching moment coefficient for the parabolic fillet at $\alpha = 12.5°$ is most likely related to the formation of the outboard vortex at this angle as seen on the oil flow (Figure 5) for which the footprint is absent on the diamond fillet. In the case of no juncture fillet such as in the works of Viet [7] (abrupt change in wing sweep), the presence of an outboard wing vortex remained steady throughout the considered angle of attack range and formed earlier at $\alpha = 11°$. This is thus different to the parabolic fillet and diamond fillet. Besides the symmetric forces, the diamond fillet generates a maximum rolling moment that is twice as high, suggesting that the diamond fillet likely exhibits a more sensitive flow behaviour. In conclusion, the parabolic fillet forms an OBV briefly at $\alpha = 12.5°$ and permanently after $\alpha = 17°$ (until possible breakdown). The diamond fillet features 3D separation and no clear OBV footprint. Overall, both parabolic and diamond fillets attain the same pitch-break angle of 17°. The steeper reduction in C_M for the parabolic fillet at $\alpha \approx 15°$ is most likely due to a stronger V1 and a delayed breakdown thereof (as demonstrated by Figure 14). The cause for the temporary increase in C_M at $\alpha = 18°$ has not been found, but could be related to vortex interaction of V1 and V2.

C. Effects of Wing Fences

Full-chord fences are tested at three spanwise locations in the kink region to determine their influence on pitching moment characteristics and vortex behaviour. First, the forces and moment data are discussed. They have been measured for all three fences on both the wing with parabolic fillet and the wing with diamond fillet. Then, the changes in flow topology are described. This was carried out for the middle fence (Fence 2) only.

1. Lift, Drag & Pitching Moment

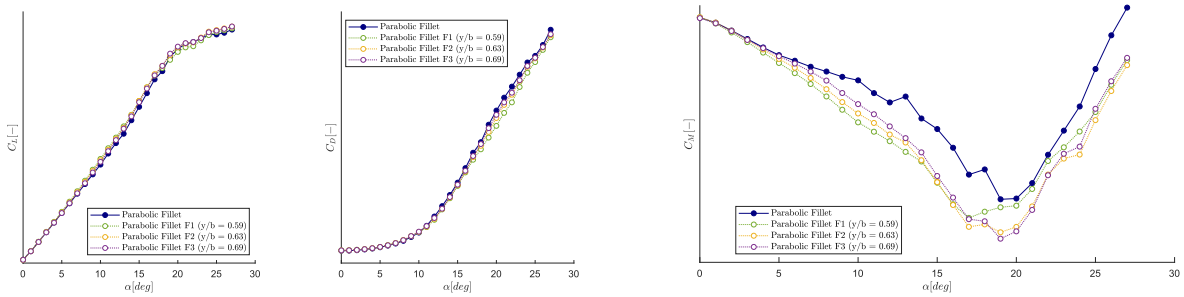

Fig. 17 Lift, Drag and Pitching Moment Coefficient for Parabolic Fillet wing with fences.

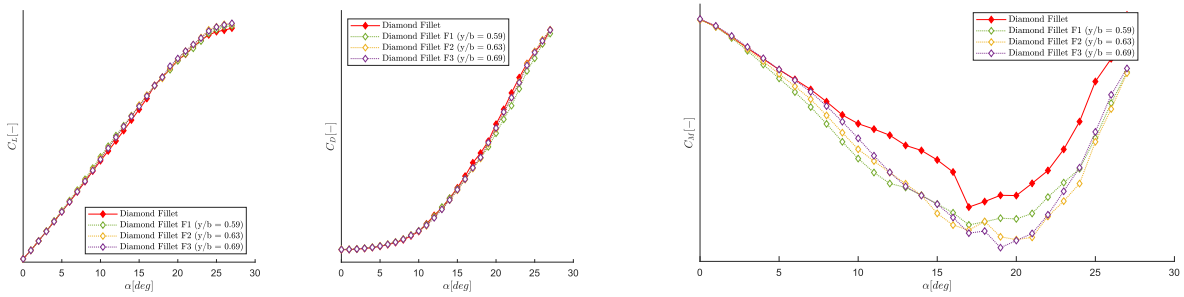

Fig. 18 Lift, Drag and Pitching Moment Coefficient for Diamond Fillet wing with fences.

Figure 17 presents the lift, drag and pitching moment coefficient for different fence configurations on the wing with parabolic fillet. All full-chord fences are found to increase the lift coefficient by reducing the flow separation on the trailing edge of the outboard wing. Only for $18° < \alpha < 25°$, the most inboard fence (F1) reduces the lift coefficient. This could be caused by the spanwise obstruction of the vortex trajectory of the inboard LEVs, leading to a reduction in vortex lift. F1 increases the lift coefficient the most at moderate angles of attack ($\alpha < 18°$), with a lift increase of up

to 5.8% compared to the clean wing. The wing with the most outboard fence (F3) attains the highest maximum lift coefficient. Hussain reported similar findings on a swept wing with multiple spanwise fence locations. He notes that the spanwise placement of boundary layer fences involves a trade-off between lift improvement and stall angle [21].

Fence 1 is not capable of continuing the same lift increase after $\alpha = 18°$ and consequently causes a smaller nose-down pitching moment, probably because the separated region re-establishes sooner for fence 1. Fence 3 increases the lifting capabilities of the outboard wing the most for large angles of attack, resulting in the smallest C_M at $\alpha = 19°$. However, the pitch-break instability for this fence also begins at $\alpha = 17°$ as evident by the break in slope at this angle. The pitch-break angle thus remains unchanged compared to the baseline case. Therefore, none of the fences successfully postpone the pitch-break compared to the clean wing, despite the increase in lift. This suggests that the cause of the pitch-break might not be related to the outboard wing performance.

In terms of drag, the fences contribute to increases in parasite (zero-lift) drag of +2.9%, +2.4%, and +2.6% for fences 1, 2, and 3, respectively. However, due to the reduction in trailing edge separation at high α, the fences reduce the pressure drag. As a result, the total drag coefficient is reduced by up to 9.2% (at $\alpha = 21°$). Among the configurations, fence 1 results in the lowest total drag for $\alpha > 11°$ since it results in the smallest separated region.

Figure 18 presents the forces and moment data on the diamond fillet. While the observed trends are the same, the lift coefficient for F1 is reduced for $16° < \alpha < 24°$, thus happening slightly earlier. This further supports the hypothesis that the inboard fence interferes with the trajectory of the LEVs at high α, given that V1 is 2% more outboard on the diamond fillet compared to the parabolic fillet (see Figure 12) and thus faces the fence obstruction earlier. F1 increases the lift coefficient the most, by up to 4.4% compared to the clean wing with diamond fillet (at $\alpha = 12°$). F3 achieves the highest lift coefficient. The combination of F3 with the diamond fillet results in a drag reduction of up to 16.9% compared to the baseline wing (at $\alpha = 19°$). However, the installation of fences in combination with the diamond fillet do not postpone the pitch-break beyond $\alpha = 17°$.

These obtained results are consistent with van Uitert's findings for a full-chord fence at the kink location of the Flying V [12]. Van Uitert also found that the fences remove the erratic pitching moment behaviour that is noticed around $\alpha \approx 12.5°$. According to van Uitert, this could be the result of increased vortex strength of the kink vortex over the outboard wing, which seems to be the case, and that the pitch-break is most likely related to the forward movement of inboard vortices. Finally, van Uitert described that the maximum usable lift coefficient was increased thanks to the fence installation. In this study this was not necessarily the case, given that the instabilities in the moment curve begin at the same angle of attack as the pitch-break of the baseline wing. Since Fence 2 shows the flattest pitch-break behaviour and achieves the same pitch-break angle as fence 1, the flowfield around this fence was chosen for further examination with PIV.

2. Flow Topology

Fence 2 promotes the formation of a leading edge vortex above the outboard wing (OBV) regardless of the installed juncture fillet. Its presence remains steady over the considered angle of attack range as evident by the oil flow photos in Figure 5, Figure 6 and Figure 7. This OBV leaves an identifiable footprint at $\alpha \approx 12.5°$ for the Diamond Fillet and $\alpha \approx 15°$ for the parabolic fillet. The footprint of the OBV on the fenced wing is larger than on the clean wing, and its distinct s-shaped streamlines are clearly visible. The OBV then remains close to the surface for the entire range of considered angles, likely resulting in the disappearance of the erratic behaviour of the moment coefficient at $\alpha \approx 12.5°$. This is in contrast with the temporary appearance of the OBV that was seen on the clean wing with parabolic fillet. On the oil flow, the OBV spans a greater portion of the wing surface for the wing with parabolic fillet and fence compared to that on the wing with diamond fillet and fence. Additionally, the fence produces a sink-like accumulation of oil inboard of the fence. This is a form of three-dimensional separation and has also been observed by Rambacher [29]. It is believed to be caused by the overpressure inboard of the fence.

In addition to the vortex above the outboard wing, the fence produces its own fence vortex (FV) which can be seen in the vorticity contours obtained with PIV in Figure 19. This fence vortex rotates in opposite direction compared to the LEVs and forms due to the spanwise flow component over the top of the fence. At low angles of attack such as $\alpha = 12.5°$, the trailing edge vortex (TEV) and fence vortex (FV) can be identified individually. By $\alpha = 15°$, the fence

vortex seems to have merged with the TEV due to their close relative position and same sense of rotation (see Figure 20). As α increases, the combined TEV+FV moves further outboard, moving from 65% span at $\alpha = 15°$ to 70% span at $\alpha = 20°$.

The fence has a considerable effect on the positioning and strength of the leading edge vortices. With the fence in place, V2 shifts further away from the wing surface (from -0.09 to -0.03 $z/\bar{c}$, or by +20mm, at $\alpha = 12.5°$). V2 is also shifted inboard from 66.5% y/b to 61% y/b (or -33mm) at $\alpha = 12.5°$ and from 72% y/b to 61% y/b (or -66mm) at $\alpha = 15°$. Unlike the clean wing, where V2 moves outboard with increasing angle of attack, the spanwise location of V2 is thus fixed on the fenced wing. This most likely has a significant effect on the outboard wing vortex, which shows a clearer footprint in oil flow on the fenced wing than on the clean wing (see Figure 6). The effects on the outboard vortex are however difficult to quantify due to its location outside the PIV measurement window. Meanwhile, V1 shifts only slightly inboard by +2% y/b due to the fence. V1 and V2 thus move towards each other before merging at $\alpha \approx 16°$. The vorticity of V2 intensifies while V1's vorticity is more confined (Figure 20) compared to the clean wing (Figure 12).

The fence's influence on vortex positioning and intensity dominates over the juncture fillet effects. The vorticity and velocity contours appear nearly identical for both the parabolic and diamond fillets when the fence is present and do not show the fillet-specific effects seen on the clean wing. In summary, the fence bends the vortex trajectories of the inboard vortices downstream and promotes interactions between them, irrespective of the juncture fillet type. The fence also promotes the formation of a vortex above the outboard wing and halts the boundary layer cross-flow towards the tip.

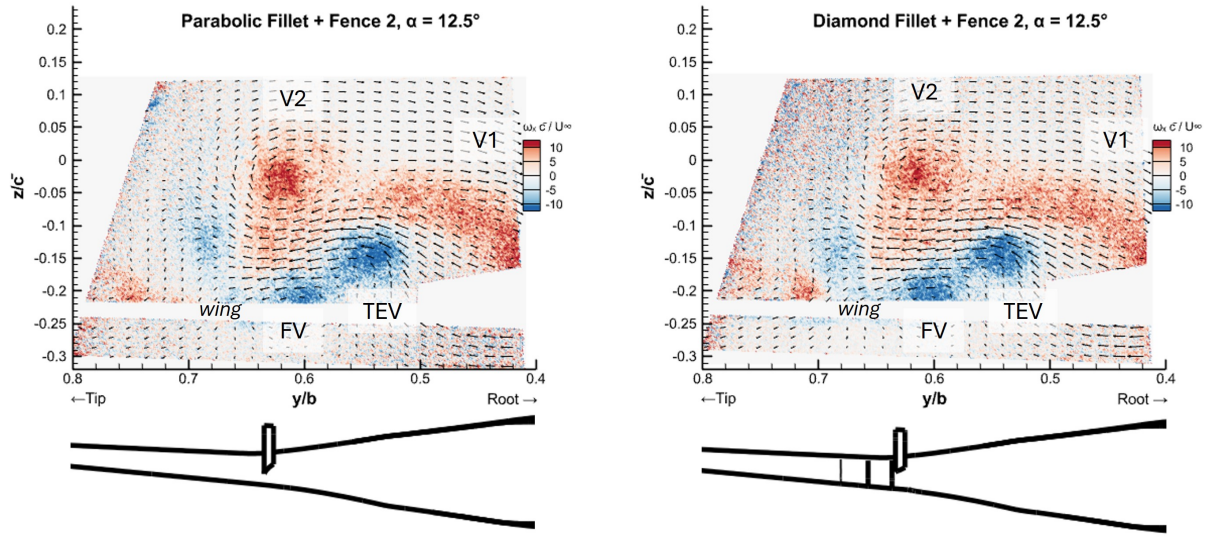

Fig. 19 Vorticity contour for parabolic fillet and diamond fillet with fence 2 ($\alpha = 12.5°$).

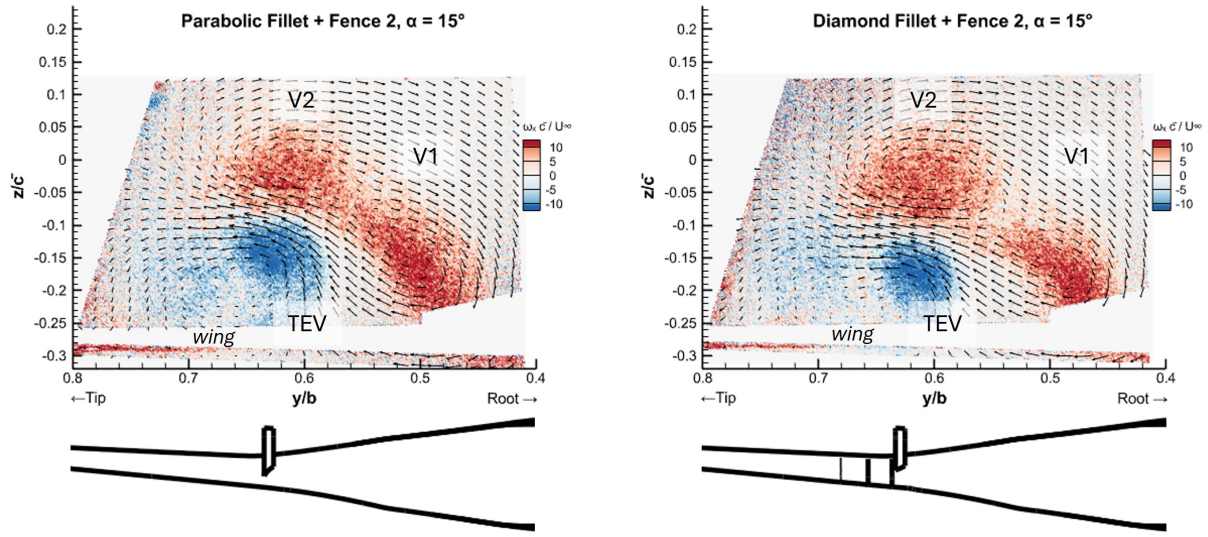

Fig. 20 Vorticity contour for parabolic fillet and diamond fillet with fence 2 ($\alpha = 15°$).

IV. Conclusion

This study examines the effects of juncture fillets (parabolic and diamond) and full-chord fences on vortical flow structures and pitching moment characteristics for the Flying V. The experimental results reveal that the parabolic fillet outperforms the diamond fillet at angles of attack above 15° by generating up to 7% more lift, maintaining stronger vortex structures and delaying vortex breakdown. In contrast, the diamond fillet reduces drag at lower angles due to decreased flow separation on the outboard wing. Full-chord fences contribute positively by increasing lift on the outboard wing by up to 5.8% and improving the pitching moment response. Despite the increase in lift, none of the tested configurations postponed the pitch-break angle. The results suggests that the primary instability at high angles of attack is largely due to the forward movement and potential breakdown of inboard vortices, rather than a loss of lift on the outboard wing.

The interpretation of the results is limited by the use of a single Particle Image Velocimetry (PIV) plane location and its small window size, which restricts the ability to capture the flow topology close to the wing's kink region or above the outboard wing. Further research could benefit from employing PIV across multiple chordwise stations to gain a better understanding of the complex flow phenomena. Additionally, experimenting with different leading edge geometries could help to stabilise the position of leading edge vortices and reduce the forward shift of the centre of pressure. Testing slats on the outboard wing could also prove beneficial in increasing its stall angle to partly counter the forward movement of the centre of pressure and increase the maximum usable lift coefficient. More fundamental investigations into the flow over a blunt-nosed crescent wing, with a specific focus on the kink region, could be beneficial as this area presents particularly complex and influential vortex interactions. This research contributes valuable insights into vortex control methods for unconventional aircraft designs and highlights the need for further exploration of the flow topology over blunt-nosed crescent wings to optimize the stability of such configurations at high angles of attack.

References

[1] ICAO, "On Board a Sustainable Future," , 2016. URL https://www.icao.int/environmental-protection/Documents/ICAOEnvironmental_Brochure-1UP_Final.pdf.

[2] Ritchie, H., "Climate change and flying: what share of global CO2 emissions come from aviation?" , 2020. URL https://ourworldindata.org/co2-emissions-from-aviation.

[3] Tracker, N. Z., "Net Zero Stocktake 2023," , 2023. URL https://www.zerotracker.net/analysis/net-zero-stocktake-2023.

[4] Torenbeek, E., *Advanced Aircraft Design: Conceptual Design, Technology and Optimization of Subsonic Civil Airplanes.*, 1st ed., Wiley, 2013.

[5] Bravo-Mosquera, P. D., Catalano, F. M., and Zingg, D. W., "Unconventional aircraft for civil aviation: A review of concepts and design methodologies," *Progress in Aerospace Sciences*, Vol. 131, 2022. https://doi.org/10.1016/j.paerosci.2022.100813.

[6] Benad, J., and Vos, R., "Design of a Flying V Subsonic Transport," *33rd Congress of the International Council of the Aeronautical Sciences*, 2022. Available at http://resolver.tudelft.nl/uuid:95ea413d-d5b1-4cb2-a650-828cb106dbbd.

[7] Viet, R., "Analysis of the flight characteristics of a highly swept cranked flying wing by means of an experimental test," , 3 2019. Available at http://resolver.tudelft.nl/uuid:90de4d9e-70ae-4efc-bd0a-7426a0a669c3.

[8] Kern, S., "Vortex Flow Control Using Fillets on a Double-Delta Wing," *Journal of Aircraft*, Vol. 30, No. 6, 1993. https://doi.org/10.2514/3.46422.

[9] Hebbar, S., M., and Khozam, A., *Investigation into the effects of juncture fillets on the vortical flow over a cropped, double-delta wing*, 1994. https://doi.org/10.2514/6.1994-626.

[10] Hebbar, S., Platzer, M., and Khozam, A., *Experimental investigation of vortex flow control using juncture fillets on a cropped double-delta wing*, 1995. https://doi.org/10.2514/6.1995-649.

[11] Hebbar, S., Platzer, M., and Chang, W., "Juncture fillets for vortex flow control on double-delta wings undergoing sideslip," *34th Aerospace Sciences Meeting and Exhibit*, 1996. https://doi.org/10.2514/6.1996-663.

[12] van Uitert, J., "Experimental Investigation into the Effect of Aerodynamic Add-ons on the Aerodynamic Characteristics of the Flying V," , 1 2021. Available at http://resolver.tudelft.nl/uuid:fdfff622-792c-4d54-a048-b59abf477a11.

[13] Lamar, J., Obara, C., Fisher, B., and Fisher, D., "Flight, Wind-Tunnel, and Computational Fluid Dynamics Comparison for Cranked Arrow Wing (F-16XL-1) at Subsonic and Transonic Speeds," Tech. Rep. NASA/TP-2001-210629, NASA, Langley Research Center Hampton, Virginia 23681-2199, 2001.

[14] Obara, C., and Lamar, J., "Overview of the Cranked-Arrow Wing Aerodynamics Project International," *NASA Langley Research Center*, 2015.

[15] Laar, Y., "Aerodynamic Design of a Flying V Aircraft in Transonic Conditions," , 10 2023. Available at http://resolver.tudelft.nl/uuid:591093b2-5cdc-41c5-b564-3786f43d51db.

[16] Laar, Y., Atherstone, D., Benad, J., and Vos, R., "Aerodynamic Design of a Flying V Aircraft in Transonic Conditions," *AIAA SCITECH 2024 Forum*, 2024. https://doi.org/10.2514/6.2024-2669.

[17] Kern, S., "Numerical Investigation of Vortex Flow Control Through Small Geometry Modifications at the Strakewing Junction of a Cropped DoubleDelta Wing," *30th Aerospace Sciences Meeting & Exhibit*, 1992.

[18] Gonzalez, H., McLachlan, B., Erickson, G., and Bell, J., "Effects of Various Fillet Shapes on a 76/40 Double Delta Wing from Mach 0.18 to 0.7," *RTO AVT Symposium on Advanced Flow Management*, 2003.

[19] Gonzalez, H., and Erickson, G., "Pressure-Sensitive Paint Investigation of Double-Delta Wing Vortex Flow Manipulation," *43rd AIAA Aerospace Sciences Meeting and Exhibit*, 2005. https://doi.org/10.2514/6.2005-1059.

[20] Walker, M., and Bons, J., "The Effect of Passive and Active Boundary-Layer Fences on Swept-Wing Performance at Low Reynolds Number," *AIAA SciTech 2018 Forum*, 2018. https://doi.org/10.2514/6.2018-0793.

[21] Hussain, A., and Bons, J., "The Effect of Active Boundary Layer Fence Spanwise Location on Swept Wing Performance," *AIAA SciTech 2019 Forum*, 2019. https://doi.org/10.2514/6.2019-3684.

[22] McFadden, E., Brandt, P., and Bons, J., "Swept Wing Active Flow Control Using a Streamwise Row of Vortex Generating Jets," *AIAA SciTech 2022 Forum*, 2022. https://doi.org/10.2514/6.2022-1546.

[23] Hitzel, S., "Sub- and Transonic Vortex Breakdown Flight Condition Simulations of the F-16XL Aircraft," *Journal of Aircraft*, Vol. 54, No. 2, 2017. https://doi.org/10.2514/1.C033246.

[24] Faculty of Aerospace Engineering, "Low Turbulence Tunnel," , ???? URL https://www.tudelft.nl/lr/organisatie/afdelingen/flow-physics-and-technology/facilities/low-speed-wind-tunnels/low-turbulence-tunnel.

[25] Kumar, V., Mandal, A., and Poddar, K., "An experimental investigation on the aerodynamic characteristics and vortex dynamics of a flying wing," *The Aeronautical Journal*, 2023.

[26] Schütte, A., Hummel, D., and Hitzel, S., "Numerical and experimental analyses of the vortical flow around the SACCON configuration," *28th AIAA Applied Aerodynamics Conference*, 2010. https://doi.org/10.2514/6.2010-4690.

[27] Konrath, R., Schröder, A., and Kompenhans, J., "Analysis of PIV Results Obtained for the VFE-2 65° Delta Wing Configuration at Sub- and Transonic Speeds," *24th AIAA Applied Aerodynamics Conference*, 2006. https://doi.org/10.2514/6.2006-3003.

[28] Luckring, J., "A Survey of Factors Affecting Blunt-Leading-Edge Separation for Swept and Semi-Slender Wings," *28th AIAA Applied Aerodynamics Conference*, 2010. https://doi.org/10.2514/6.2010-4820.

[29] Rambacher, C., Butler, E., and Bons, J., "Analysis of a Passive vs. Active Boundary Layer Fence on a Low Aspect Ratio Swept Wing in Subsonic Flow," *AIAA SciTech 2024 Forum*, 2024. https://doi.org/10.2514/6.2024-1936.

Part II

Literature Study

**This part has been assessed for the course AE4020 Literature Study.*

1

Introduction

The aviation sector, responsible for up to 3.5% of global carbon emissions, faces increasing regulatory pressure to meet net-zero targets worldwide [1, 2]. Up to 149 countries have set net-zero targets, and given this legal climate the need for sustainable aircraft is larger than ever [3]. Conventional tube-and-wing aircraft have reached a plateau in terms of efficiency, with efficiency gains in the order of a few percent over the last two decades [4, p 125]. In order to substantially reduce carbon emissions, researchers have turned to new, unconventional configurations such as flying wings and blended wing bodies [5]. While the flying wing concept has been around since the early days of aviation, their application remains predominantly limited to only a handful of military aircraft. The concept of a commercial flying wing that carries passengers was quickly abandoned in the 1950s due to control and stability issues [6]. However, with the advance in systems and control technology and the environmental drive to make aviation more sustainable, flying wings have regained interest by numerous research institutions and aerospace companies alike. Flying wings could reduce aviation emissions by up to 50% thanks to their high aerodynamic efficiency, posing a promising solution to reduce the aviation carbon emissions [5].

One of these, the Flying V, is a prototype long-haul flying wing developed at the TU Delft. With the passengers and cargo housed inside the wing, the aircraft is said to reduce fuel consumption and carbon emissions by up to 20% compared to tube-and-wing aircraft [7]. In order to determine the aircraft's feasibility, a lot of research is ongoing. Consequently, the aircraft was found to be statically unstable at pitch angles above 19° [7, 8]. This results in an unsafe and undesired flight handling quality, limiting the usable pitch angle of the aircraft. This, in turn, reduces the maximum allowable lift coefficient and results in a longer take-off and landing field length, harming the aircraft's operational capabilities. The reason for the abrupt change in pitching moment is not fully understood and necessitates wind tunnel experimentation to determine its cause. Furthermore, based on literature, the addition of a wing juncture fillet could be a solution to postpone the pitch-break to larger angles of attack [9]. In order to investigate this, different juncture fillet designs are to be tested in the wind tunnel to determine their effects on the vortex structures and aircraft pitching moment.

This literature review begins with detailing the research gaps and research relevance, objective and research questions in chapter 2. Then, in chapter 3, the Flying V is presented and its aerodynamic characteristics are discussed. Chapter 4 dives into the intricate topic of vortex aerodynamics, discussing its formation, breakdown and example work on flying wings and blended wing bodies. The chapter also includes a discussion on the numerical solvers that could be used to simulate leading edge vortices. Then, chapter 5 specifically addresses the wing juncture fillet and its effects on the forces and vortical flow patterns. The literature study ends with important principles on wind tunnel experimentation in chapter 6 followed by the research methodology in chapter 7.

2

Research Formulation

This chapter forms the basis of the research that will be conducted during this thesis. The chapter begins with explaining the relevance and research gaps related to this thesis in section 2.1. Then, the objective is formulated in section 2.2, followed by the research questions in section 2.3.

2.1. Research Gaps

While the flying V is in essence a flying wing, its planform is distinctly different to other flying wings. At high angles of attack, the vortex aerodynamics of the highly swept crescent wing has not been fully understood. This is because little research has been conducted particularly on kinked wings with round leading edges. The lack of understanding of the vortical flow patterns on these wings forms the first notable research gap. Moreover, at angles of attack in excess of 19 degrees, the Flying V loses its static equilibrium about its center of gravity [7]. This phenomenon is referred to as a pitch-break and has been observed in wind tunnel tests [8]. The pitch-break significantly impacts the aircraft's maximum usable lift coefficient, thereby restricting its operational capabilities. However, the underlying cause of this phenomenon remains unexplored. This forms the second research gap.

It is suspected that vortex breakdown over the wings may contribute to this phenomenon, yet conclusive evidence is lacking. Therefore, there is a need for research to delve into the origins of this issue and propose possible solutions. One of these solutions might be a modification referred to as a juncture fillet. The shape of this fillet is known to affect the vortical flow patterns over wings at high angles of attack, as studied by Kern [9] and Hebbar [10, 11, 12]. However, little is known about its effects over wings with blunt leading edges. This forms the last research gap. The research conducted during this thesis aims to address this gap by investigating the effects of the juncture fillet shape on the vortical flow structures and the pitching moment of the Flying V. Given the novelty of applying juncture fillets to wings with rounded leading edges, the outcome of this research might be vital to the feasibility and sustainability of flying wing configurations like the Flying V.

2.2. Research Objective

The primary objective of this research is:

"To understand the influence of the juncture fillet shape on the vortical flow structures over the Flying V at high angles of attack."

2.3. Research Questions

The main research question guiding this study is as follows:

What is the relationship between the juncture fillet design and the vortical flow structures over the Flying V at high angles of attack?

The main research question is further supported by four sub-questions which form a guidance throughout the literature study and the experimental research of the thesis:

- How does a wing juncture fillet affect the lift generation mechanisms of highly swept wings at high angles of attack?
- What is the influence of the wing juncture fillet design on the lift and pitching moment of the Flying V at high angles of attack?
- What wind tunnel measurement and visualisation techniques can be used to determine and demonstrate the vortex aerodynamics of the Flying V?
- What flow solver is best suited for a medium fidelity, fast evaluation of the junction fillet design?

3

The Flying V

With the scope of the research well-defined, this chapter explores the design of the Flying V. First, section 3.1 introduces the concept of a flying wing and explains what makes a flying wing such a promising concept to make aircraft more fuel-efficient. Then, the design of the Flying V is presented in section 3.2, followed by a more detailed look into the design optimisation and aerodynamic characteristics in section 3.3 and section 3.4.

3.1. Flying Wings

Flying wings are aircraft where the payload, structural components and lifting wing are combined. This classes the Flying V as a flying wing. Flying wings have been trialed as early as the 1910s, but flying wings were quickly found to be difficult to control [6]. During and after World War II, interest in flying wings in the military sector grew due to their ability to fly higher while carrying a large amount of payload. This lead amongst others to the development of the propeller powered YB-35 which was soon followed by the jet powered YB-49 in Figure 3.1. Northrop, the company who built the YB-49, believed that flying wings would soon become the future of air travel [13, p 173]. However, after many stability issues and a fatal crash during its test campaign in 1948, the concept was abandoned [14]. With the advancements in technology in the 1980s, new flying wings such as the B-2 bomber in Figure 3.2 were developed and entered service.

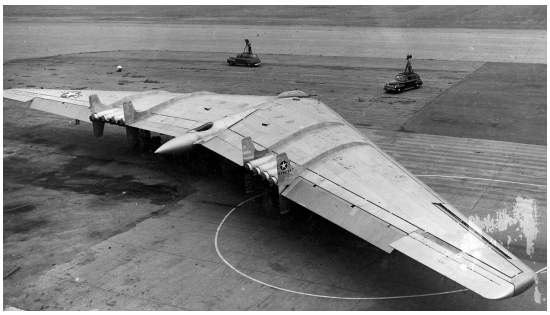

Figure 3.1: The Northrop YB-49 prototype bomber first flew in 1947 but never entered service. [1]

Figure 3.2: The Northrop Grumman B-2 Spirit entered service in 1997 as a US Air Force strategic stealth bomber. [2]

[1] Retrieved from: https://media.defense.gov/2006/Oct/25/2000538599/-1/-1/0/061025-F-1234S-021.JPG
[2] Retrieved from: https://www.af.mil/About-Us/Fact-Sheets/Display/Article/104482/b-2-spirit/

Flying wings are now regaining interest in the commercial aviation sector, due to their ability to drastically lower fuel consumption and emissions. Flying wings could revolutionise air travel thanks to their high aerodynamic efficiency, as explained by Bravo-Mosquera [5] and Martinez [15]. Flying wings have three main advantages:

- The lack of a horizontal tailplane and fuselage reduces the wetted surface area, thereby reducing the parasite drag.
- Due to its larger wing chord compared to conventional tube-and-wing aircraft, a flying wing flies at a higher Reynolds number, which reduces the skin friction coefficient.
- The mass of the payload and fuel are better distributed within the wing to offset the lift force. This span-loading reduces the bending moment and in conjunction with a missing tail lowers the structural mass.

While flying wings have a higher aerodynamic efficiency than tube-and-wing aircraft, they suffer from one large setback; control and stability. Because of the lack of a horizontal stabilizer, the flying wing is more difficult to trim. The elevons that are usually found on a flying wing are positioned closer to the center of gravity compared to a tube-and-wing aircraft. This reduces the moment arm which makes the elevons less effective. Consequently, flying wings have a smaller static margin and thus require careful positioning of the center of gravity. In addition to static stability, flying wings do not exhibit sufficient damping in the dutch roll eigenmode. Due to these setbacks, flying wings have not been commercially successful besides a handful of military applications [6].

However, things are bound to change. Due to advancements in digital controls such as fly-by-wire, stability augmentation systems and a careful positioning of the aerodynamic center with respect to the center of gravity [16], the aircraft's stability drawbacks can be overcome. Due to their high aerodynamic efficiency, flying wings could lead to environmental and financial benefits such as lower fuel-burn at equal payload capacity, which could lower the direct operating cost (DOC) for airlines. In light of this, the flying wing is again seen as one of the solutions to make aviation more sustainable [5]. Nevertheless, several potential issues still require extensive research and development efforts as outlined next.

3.2. The Flying V's Anatomy

The Flying V is a flying wing concept designed to transport 361 passengers at a cruise Mach number of 0.85, while offering a more energy efficient alternative to conventional tube-and-wing (CTW) aircraft. This is achieved by fitting the passengers, cargo and fuel into the wing which increases the aerodynamic efficiency and decreases the structural weight. The Flying V has a design range of 15000km, making the aircraft similar to the Airbus A350-1000 in terms of operational capabilities. The Flying V was originally conceived by J. Benad [17] in 2015. The concept has been under development at the TU Delft since 2016, and as it stands now, promises a 20% lower fuel consumption for the same payload-range combination with current engine technology [7].

The Flying V, presented in Figure 3.3, features a crescent wing. A crescent wing has a larger sweep angle on the inboard wing compared to the outboard wing, complemented by a swept trailing edge. This large inboard sweep angle allows for a sufficiently high critical Mach number given the 13% thickness-to-chord ratio of the wing. This thickness is necessary to provide enough interior space to accommodate the passengers. The outboard wing has less sweep to increase the aircraft's stability and effectiveness of the control surfaces. The improved lift distribution and reduced wetted surface area result in a lift-to-drag ratio (L/D) of 24.2, 26% higher compared to the NASA Common Research Model [18, 19]. The latter being a benchmark for current CTW aircraft. In conclusion, the crescent wing enables substantial aerodynamic improvements while allowing for effective outboard control surfaces to trim the aircraft.

The aircraft is controlled using elevons fitted at the trailing edge of the outboard wing. Elevons effectively combine the functions of the elevators and ailerons into one surface for pitch and roll control. The wings are extended with two vertical surfaces (winglets) which house the rudders. The Flying V does not strictly require any high-lift devices (HLD) for take-off and landing thanks to its intricate vortex lift (explained in next section) and a lower wing loading (W/S) compared to conventional aircraft. This,

however, requires a high pitch attitude during landing which obstructs the pilot's field of view and also requires a long landing gear to provide enough tail clearance at rotation. Eftekhar [20] therefore recommends to install HLD to tackle those issues and lower the pitch angle at landing by 3 degrees. Finally, a large pitching moment is required to rotate the aircraft, because the moment arm between gear and elevons is small.

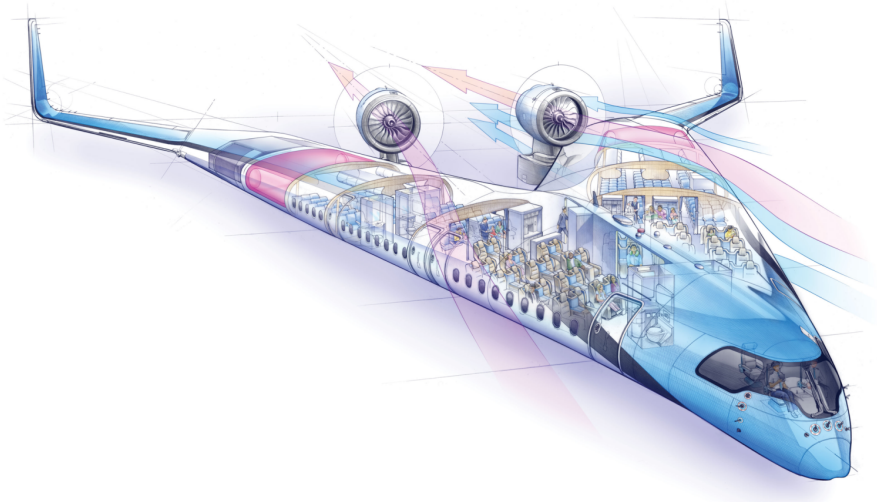

Figure 3.3: Passengers are seated within the wings. Cargo holds are situated behind the cabin. Artist impression by Bruce Morser [21].

Looking at the propulsion system, the Flying V has been developed to run on jet fuel or hydrogen. While the hydrogen propulsion system yields no carbon emissions, its need for high-volume tanks drastically eats away from the usable cargo space, reducing its capacity by 70% and reducing the aircraft's range by 35% [21]. Moreover, the storage of hydrogen introduces additional safety concerns [5, p 20]. Regardless of the energy source, the aircraft is propelled by two large turbofan engines located above the wing, slightly behind the cabin. Their location helps to reduce the noise footprint at airports thanks to the fan noise being partially shielded by the wing and the exhaust noise no longer reflecting from the lower surface of the wing [22]. While the engines are reachable from behind for maintenance, their location might place them in the wake of the wing during a stall. These challenges are still to be resolved for the aircraft to become reality.

Besides the wing and propulsion system, research has been conducted on the structural feasibility of the design. In the paper by Claeys [23] the Flying V was found to be 17% lighter than reference CTW aircraft. As the aircraft model was refined and the engine and landing gear were integrated, the structural sizing needed further research. The work was continued by Dotman [24] who estimated the operative empty weight (OEW) to be between 65 and 67 tonnes depending on the chosen spar configuration, assuming an aluminium wing structure. While the Flying V promises to be lighter than CTW aircraft, the structural sizing of the aircraft poses a number of issues. First and foremost, since the passengers are seated in the wing, the conventional two-spar configuration is difficult to implement without obstructing the interior space. Secondly, pressurisation loads are higher because the cabin sections are not circular. This requires a larger bending stiffness of the frames. Additionally, due to the novel structural layout, the crashworthiness of the aircraft is found worse than that of CTW aircraft. Desiderio [25] explained that the crashworthiness would be barely sufficient to pass requirements by regulators, even with current results likely being overly-conservative due to structural simplifications. Further structural challenges remain at the kink and nose-fuselage intersection [23]. Overall, the structural design is more complicated, prone to become heavier as more design issues need to be overcome, and might require changes to manufacturing processes.

To make the Flying V more versatile and commercially attractive, a family concept has been conceived. In the paper by Oosterom [26, 27] three variants of the Flying V are presented; the FV-800, FV-900 and FV-1000. These have a passenger capacity between 293 and 361 for the smallest and largest variant

respectively. The largest variant has a wingspan of 65m, which enables the Flying V to use the same airport infrastructure as current CTW. The FV-1000 is also the most critical in terms of fuel consumption and aerodynamic efficiency due to its larger wetted area compared to the other family members. It was found that the MTOW of the FV-1000 would be 15% smaller compared to the equivalent Airbus A350-1000. However, the family design comes at a penalty of up to 8.9% increased fuel burn compared to an individually optimised aircraft.

Besides the structural challenges, more research needs to be conducted into the passenger comfort and potential increased likelihood of motion sickness. The passengers seated furthest outboard experience more movement when banking and flying in turbulence. This was long seen as the primary reason why flying wings have not been used for passenger service [5, p 8]. Additionally, the passengers are not aligned with the direction of travel which also still necessitates further investigation. In conclusion, the novel configuration of the Flying V requires a large amount of additional research to tackle its design challenges, but might revolutionise air travel thanks to its reduced emissions and operating costs.

3.3. Optimisation of the Aerodynamic Design

In order to refine the aerodynamic design of Benad, Faggiano et al [28] carried out a multi-fidelity optimisation where the planform, airfoils and winglets were parameterised and their shape was optimised. In total, 56 design variables were used in both a dual-step and single-step optimisation. It was found that the maximum attainable L/D ratio is 23.7, a 25% improvement with respect to the NASA Common Research Model. While this paper focused on the aerodynamic performance in cruise conditions, the low-speed high angle of attack aerodynamics were not taken into account in the optimisation. Faggiano's design updates are visualised in Figure 3.4.

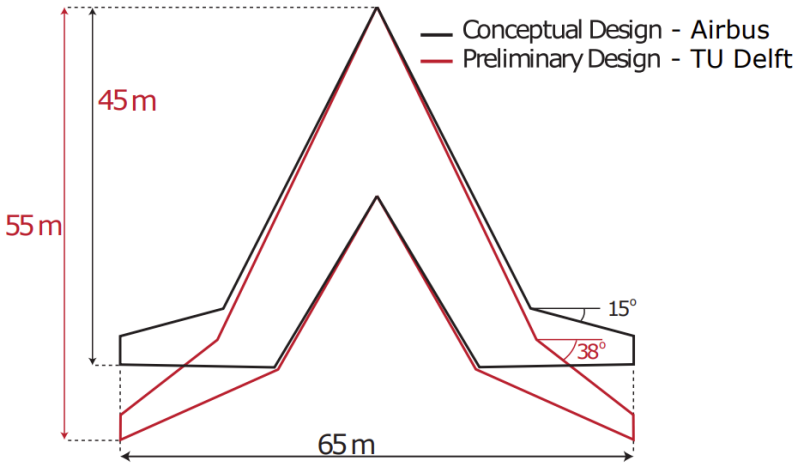

Figure 3.4: The planform was optimised by Faggiano et al [28]

After Faggiano's changes, Hillen [29] introduced a new parametrisation that allows for more design flexibility, especially in terms of the cabin dimensions. The cockpit integration was then studied by van der Pluijm [30]. Hillen's parametrisation was subsequently used by van Luijk [31, 32] for an aerodynamic optimisation of the outboard wing. Laar [18, 19] further refined the design made by van Luijk to achieve an even higher L/D ratio of 24.2 which was determined using a high accuracy CFD approach. The aircraft's excessive wave drag at the outboard wing was reduced and special attention was paid to the wing-winglet intersection where the interference drag was reduced. Figure 3.5 shows the Mach contour lines for the manually optimised wing by Laar. The highest Mach numbers occur at the leading edge kink, which further emphasises the importance of the wing design at this location. The effects of a reshaped wing kink need careful consideration not to induce new strong shocks which could lead to shock-induced separation on the upper surface during cruise.

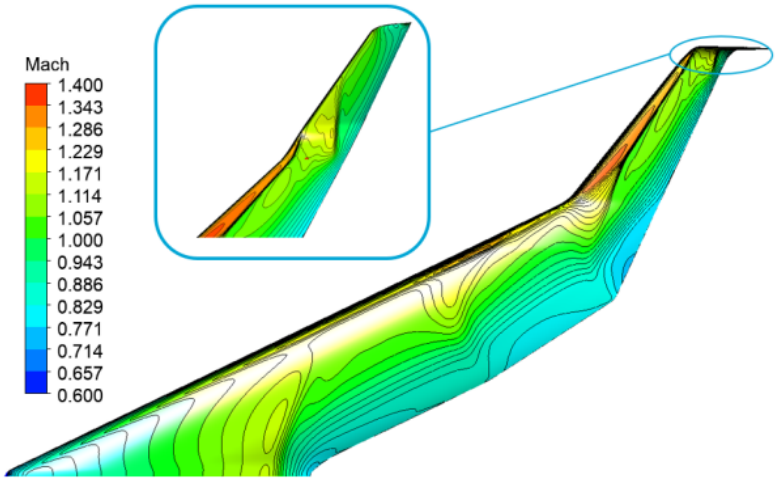

Figure 3.5: Mach contours for the optimised design by Laar. Shockwaves are still present at cruise conditions. (Mach =0.85, Re = 88.3 million, C_L = 0.26)[18]

3.4. The Flying V's Aerodynamic Characteristics

Based on the work of Faggiano, a wind tunnel half-model in 4.6% scale was made and tested under various conditions in the open jet facility at the TU Delft by Viet, Palermo and van Uitert [8, 33, 34] (Figure 3.6). While Viet investigated the air flow patterns at high angles of attack, Palermo focused on the control surface effectiveness and longitudinal balance. Van Uitert explored the effects of installing aerodynamic add-ons such as fences and vortilons on the wing.

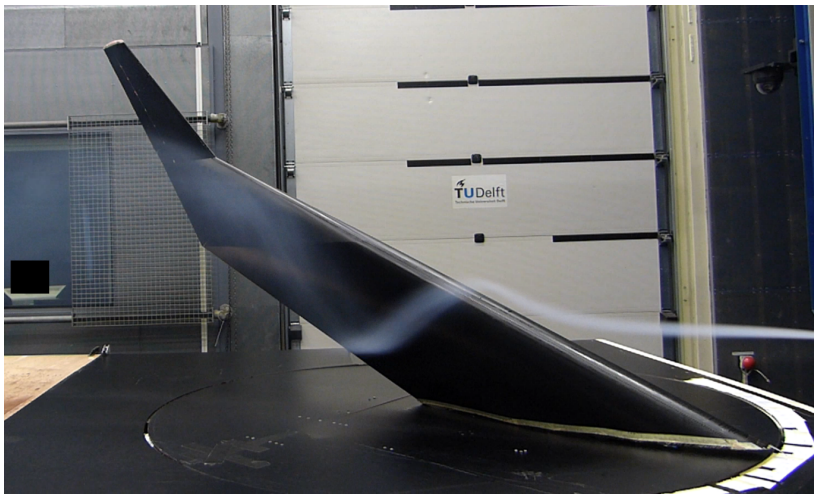

Figure 3.6: The Flying V half-wing model in the Open Jet Facility. The large leading edge vortex is visualised with smoke. [8]

3.4.1. Vortex Lift

All three experiments describe the formation of leading edge vortices (LEVs) over the upper surface of the wing at large angles-of-attack (α > 10°). The LEVs are a type of separated flow in which the air flow separates at the leading edge and rolls into a vortex such as visualised in Figure 3.8. The vortices are promoted by the large sweep angle and have strong effects on the lift generation of the Flying V's wing, as seen in Figure 3.7. The lift curve slope slightly increases after 10 degrees, a distinct sign of leading edge vortices developing above the upper surface. This additional lift component is referred to as vortex lift. As the angle-of-attack is further increased, the primary vortex moves forward, which also moves the aerodynamic center forward. This results in an increasingly larger area of separation on the trailing edge, decreasing the lift until stall occurs.

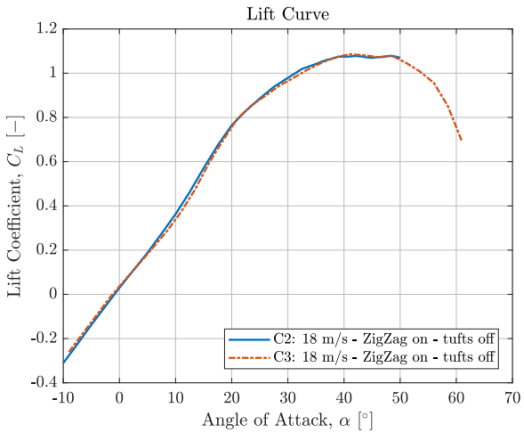

Figure 3.7: Lift curve as measured by Viet [8]

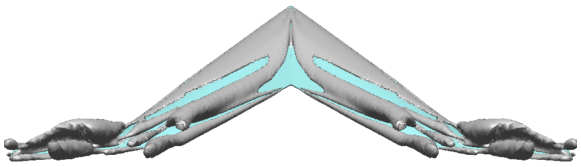

Figure 3.8: Vortical structures over the Flying V simulated using CFD at α = 20° [35]

Viet investigated and documented the flow characteristics around the Flying V's wing. Viet found a maximum lift coefficient of 1.09 at 41 degrees angle-of-attack. Contrarily to Viet, Palermo measured an untrimmed maximum lift coefficient of 1.02 at 35 degrees angle-of-attack despite being measured on the same model. According to Palermo, using the control surfaces, the aircraft could be trimmed until a maximum lift coefficient of 0.66 [33]. Using tufts, oil flow and smoke, Viet visualised the large leading edge vortices that act on the upper surface, such as in Figure 3.6. One large leading edge vortex is formed along the inboard wing and another smaller vortex is formed at the wing kink. The latter one stretches over the outboard wing. However, further work is required to fully understand the effects on the vortices caused by the transition from the inboard wing to the outboard wing.

3.4.2. Flow Patterns

Viet [8] traced the streamlines on the wing surface using an oil visualization technique in the wind tunnel. This process was carried out for various angles of attack, as illustrated in Figure 3.11 for α = 22°. Starting with small angles of attack, the airflow over the wing is attached and follows a typical structure seen on highly swept wings (Figure 3.12). Due to the wing sweep, the streamlines follow an S-shaped path over the wing surface, as seen in Figure 3.9. This is governed by the local pressure gradient which first sucks the fluid particles inboard and later outboard again as demonstrated in Figure 3.10. This curvature results in a region of accelerated flow at the trailing edge of the root, where streamlines come closer together due to symmetry. This lowers the pressure which increases pressure drag on the wing. This undesired effect is the so-called root effect [36].

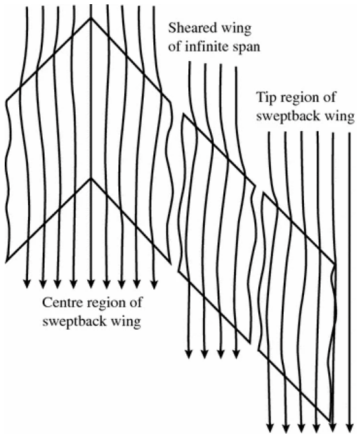

Figure 3.9: Top view of streamlines over a symmetric wing with zero lift [36]

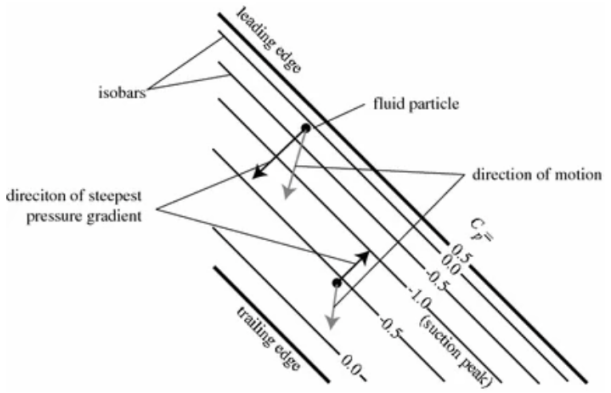

Figure 3.10: Isobar pattern over an infinitely long swept wing [36]

On the Flying V, these S-curve streamlines are found too. On the outboard wing, the S-curves are less pronounced due to the smaller sweep angle. While the oil visualisation gives a good indication of the flow patterns, the oil movement is affected by gravity as the model was in the upright position in the wind tunnel setup. The deflections are therefore exaggerated towards the trailing edge where the velocity in the boundary layer is small. Finally, a small portion of detached flow is seen too on the trailing edge in Figure 3.12. Moving to larger angles-of-attack, such as for 20 degrees in Figure 3.13, the flow over the wing is more complex. Many separation and attachment lines dominate the streamline pattern, originating from up to 7 different vortical structures. These structures quickly merge into one large leading edge vortex above the wing surface and a smaller above the outboard wing. This specific case for α = 20° is right at the pitch-break, which will be explained later. A small portion of detached flow is seen on the trailing edge, but not much more than the 5 degree case. While the streamlines derived from the oil visualisation form a basis for understanding the flow patterns over the Flying V, they are not sufficiently accurate due to model leakage at the root and the gravity effect on the oil flow. Also Reynolds number effects (explained in subsection 4.3.2) have substantial effects on the flow patterns. These results should thus be treated with the necessary caution.

Figure 3.11: Windtunnel oil visualisation at α = 22° [8]

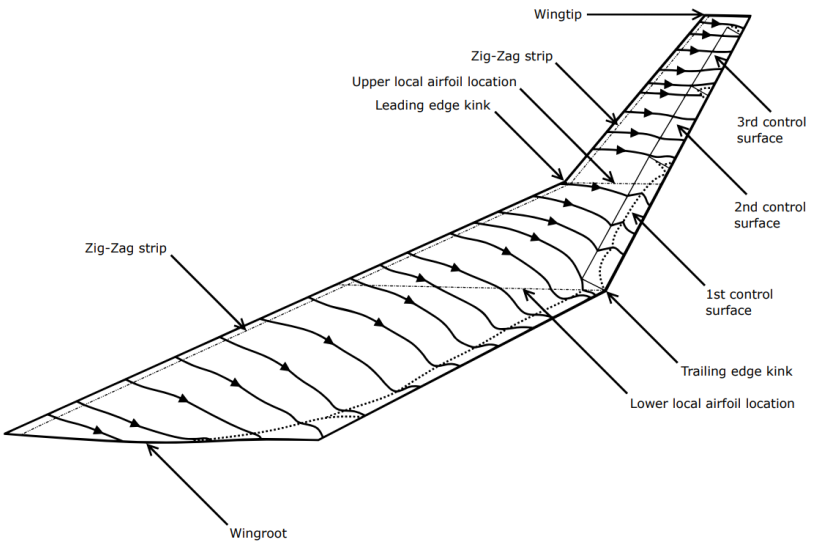

Figure 3.12: Streamlines on the upper surface for α = 5° [8]

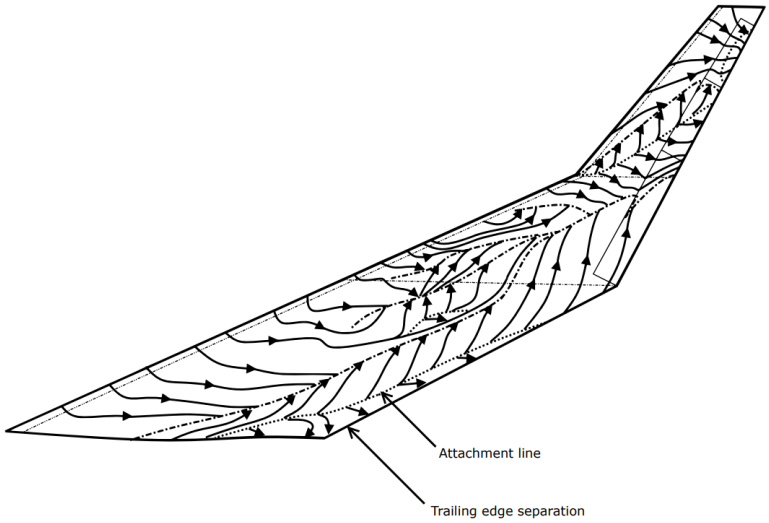

Figure 3.13: Streamlines on the upper surface for α = 20° [8]

3.4.3. Trim and Longitudinal Static Stability

In further windtunnel tests carried out by Palermo [33], the elevons of the Flying V were deflected and their effectiveness was measured for a large range of angles of attack at a Reynolds number of 1 million. The estimated effects of the thrust force were added using a flight mechanics model. Using this, the most forward and most aft center-of-gravity positions for which the aircraft could be balanced using the control surfaces were determined. Those are between -6% and 0.5% of the MAC, resulting in a static margin of 4.4%. Viet also looked into the longitudinal stability of the flying V wing, and found that the aircraft has a static margin between 1.5% MAC and 11% MAC for the most aft and most forward position of the CG respectively. Since the center of pressure moves forwards for α > 15°, the static margin quickly decreases and becomes negative. The aircraft can be trimmed until α = 32° and α = 20° for the most forward and most aft CG respectively [8].

Next to the wind tunnel experiments, a 3m span flight test model was built (Figure 3.14). The goal of the scaled flight test was to extract the stability and control derivatives of the Flying V and assess the handling qualities. This was done using system-identification techniques to extract a state-space model from the retrieved flight data [37]. While results showed similar pitching moment changes with angle-of-attack as obtained by wind tunnel experimental results, the lift curve slope and induced drag were found to be different, with the reasons still to be studied. It could be related to the aforementioned leakage of the half-model.

In approach conditions, the Flying V was found to be statically stable until an angle-of-attack of 20 degrees, after which a so-called pitch-break was observed ($dC_m/d\alpha > 0$) [33]. As seen in Figure 3.15 and Figure 3.16, the slope of the pitching moment curve is negative until an angle-of-attack of 20 degrees. Thereafter, an increase in angle-of-attack would further lead to an increase in pitching moment. This pitch-break was confirmed by Viet, Palermo and van Uitert [8, 33, 34]. It is not yet certain what causes the pitch-break, but it could be related to the vortex aerodynamics around the Flying V. It was found that the effectiveness of the control surfaces did not deteriorate until the stall angle of 35 degrees, indicating that the airflow on the control surfaces remained attached after the pitch-break. Therefore separation at the trailing edge of the outboard wing is not believed to be the reason for the pitch-break. Viet believes the pitch-break is caused by the suction peak (center of pressure) moving within the vortex due to changing vortex location and strength. The exact phenomena are unknown and form a research gap till this day.

Figure 3.14: The scale flight test model of the Flying V in summer 2020. [22]

Van Uitert [34] performed an investigation to find ways to postpone the pitch-break to higher angles-of-attack. While Viet and Palermo observed a pitch-break at α = 20°, van Uitert observed the pitch-break at α = 22.5° using the same model. The differences were argued to be caused by small structural damage to the model as well as alignment on the turntable. Different methods were trialed to change the airflow, such as trip strips, vortilons and wing fences. The installation of trip strips deteriorated the wing design by increasing the magnitude of the moment coefficient and introducing a horizontal moment curve instead of a decreasing one. The vortilons did not affect the pitch-break. Finally, the wing fence placed at the leading edge kink and spanning the entire upper surface yielded the best results, postponing the pitch-break to a 0.35 higher C_L. Since the leading edge kink was found to be the most influential location during his research, van Uitert recommends to investigate the effects of shape of the leading edge kink on the pitching moment coefficient. The research work to be conducted with this thesis is tightly linked to this pitch-break problem.

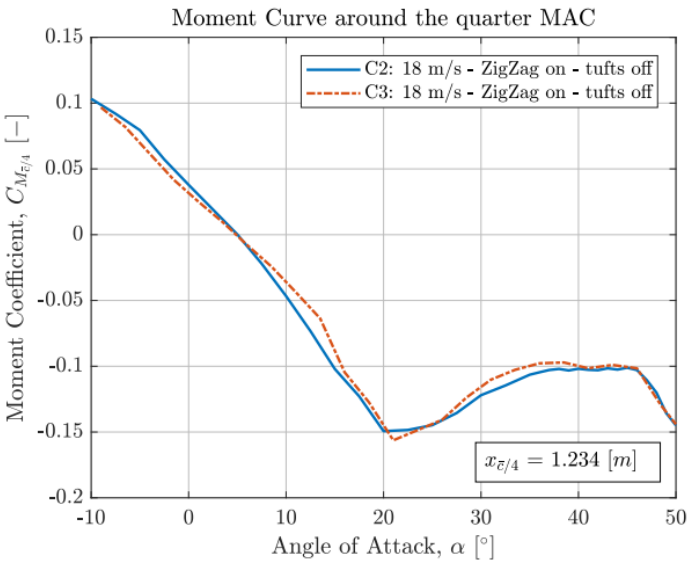

Figure 3.15: Moment curve as measured by Viet [8]

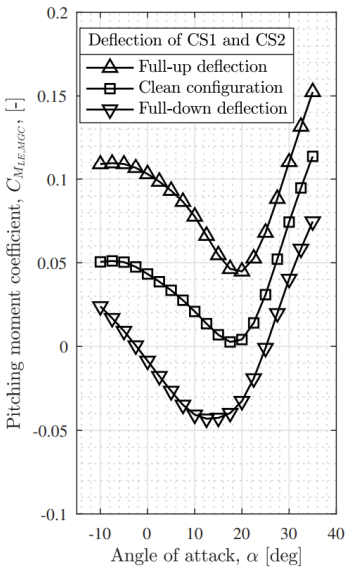

Figure 3.16: Moment curve as measured by Palermo [33] (note different moment reference point)

4

Vortex Aerodynamics

Since the Flying V's low speed aerodynamics are dominated by the interaction of vortices, this chapter begins with studying how vortices are formed in section 4.1 followed by section 4.2 which covers the aspects of vortex breakdown. Subsequently, the leading edge vortices on wings with blunt leading edges such as flying wings will be investigated in section 4.3. Furthermore, it is important to have a solid understanding on how the vortices can be better controlled and how their breakdown can be postponed. This is examined in section 4.4. The chapter concludes with section 4.5 which covers the available numerical solvers suited to determine vortical flow over blunt wings. The contents of this chapter are thus crucial to understanding the pitch-break phenomenon on the Flying V.

4.1. Formation of Leading Edge Vortices

Along the leading edge of a highly swept wing at moderate angles of attack, a pair of counter rotating leading edge vortices (LEVs) forms. The vortices form due to separation from the leading edge of the wing (which is usually sharp on delta wings). The streamlines along the wing roll up into two large vortices due to the spanwise pressure gradient. The LEVs are strengthened by the inflow of mass and vorticity from the leading edge, which expands the vortices with downstream distance. As the angle of attack is increased, secondary vortices appear as illustrated in Figure 4.1. They are caused by separation of the spanwise boundary layer flow as explained by Luckring [38]. Each abrupt change in wing sweep forms a new LEV such as on the double delta wing illustrated in Figure 4.2.

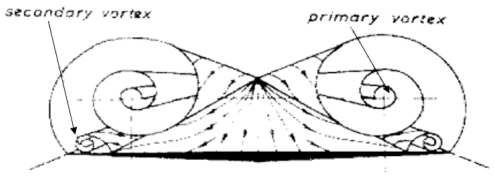

Figure 4.1: Primary and Secondary vortex over a sharp-edged delta wing. [38]

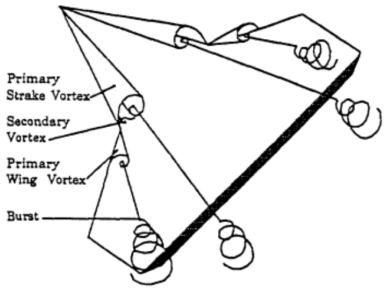

Figure 4.2: Typical vortex structures on a highly swept wing with a leading edge kink. [9]

Each vortex changes the streamline pattern on the wing surface. The primary and secondary vortices create separation and attachment lines. Those can be seen on the top surface as illustrated in Figure 4.3. According to Hall [39] each vortex has two distinct parts. A rotational outer part which is mostly inviscid and an inner viscous core. The outer part, also referred to as annulus, has approximately a constant rotational swirl velocity. In contrast, in the inner part the swirl velocity goes to zero at the axis. Within the vortex, the variations of pressure and velocity are small in the axial direction compared to the radial direction. Furthermore, the LEVs are formed at an angle with respect to the inflow velocity.

Downstream of the wing, they re-align with the free stream [40]. The LEVs are beneficial because they create additional nonlinear vortex lift, which can increase the lift coefficient C_L by up to 25% [41]. Thanks to this, LEVs have been a fundamental lift generation mechanism on many delta winged aircraft such as the F-16 Fighting Falcon and Concorde.

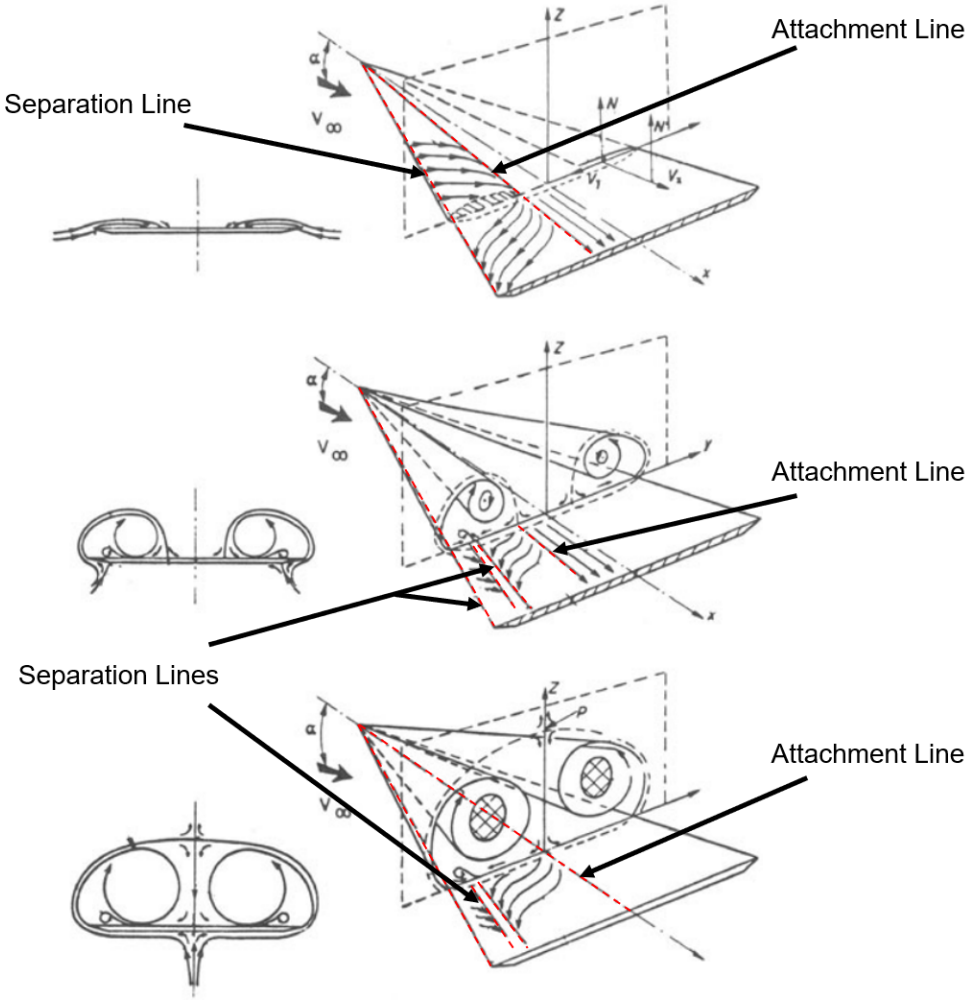

Figure 4.3: Topology of leading edge vortices for small, moderate and large angles of attack. [42]

On thick delta wings with rounded leading edges, a more complicated flow topology is observed. The flow is affected by the strong interaction between the viscous layers and the outer flow. Leading edge vortices will form further downstream, no longer separating at the leading edge. The vortex layers roll up into a three-dimensional separation structure in the shape of a spiral, but the rounded leading edge also causes the formation of secondary separation layers. As the angle of attack increases, the flow becomes more complicated by the generation of multiple vortex structures [42]. Those will be further examined in section 4.3.

4.2. Breakdown of Leading Edge Vortices

At high angles of attack, the leading edge vortices become large and move upstream until they become unstable and burst. This is characterised by an abrupt change in structure as seen in Figure 4.4 and a large deceleration of the core flow along the axis. When bursting occurs above the wing surface, it is paired with a loss in lift. The center of pressure moves forward and influences the aerodynamic forces and moments on the aircraft. In sideslip conditions, the vortices become asymmetric with the vortex at the windward side breaking up sooner. This leads to a loss of lift on the wing facing the direction of the turn, further increasing the bank angle. These characteristics determine to a large extent the

longitudinal, lateral and directional instabilities of highly swept aircraft at high angles of attack [41]. These phenomena are so important that Gutmark states that the greatest limitation to the performance of a highly-swept wing at high angles of attack is vortex breakdown [43].

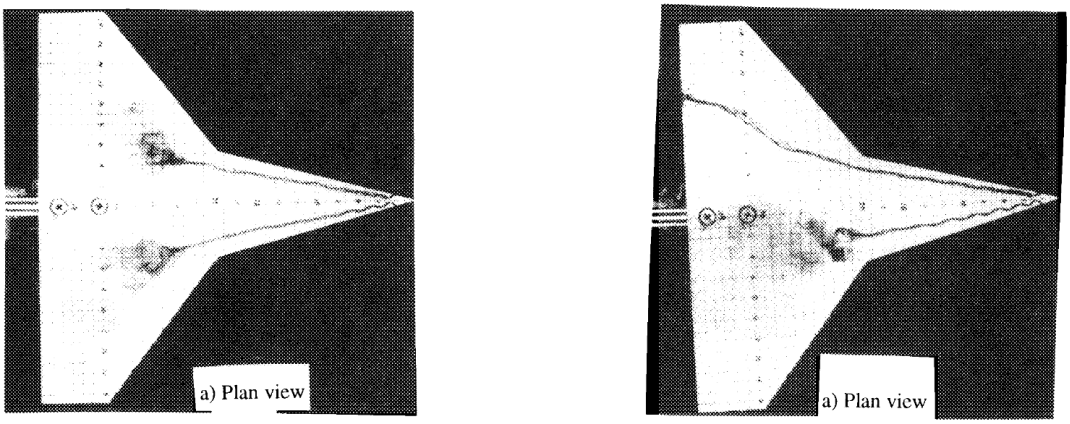

Figure 4.4: Vortex breakdown on a double delta wing (a) and the effect of sideslip on vortex trajectory (b) [12]

The bursting mechanism is complex and is strongly related to the core of the vortex, as stated by Chang [40] and Lambourne [44]. The axial flow within the core is very sensitive to the outside pressure gradient and retardation of the external flow velocity. Observations of bursting tell that when the axial velocity drops suddenly, breakdown occurs, and turbulent flow from outside the vortex enters the core. When the airflow outside the vortex is very turbulent, it has enough energy to penetrate the core. Additionally, measurements have shown that the total pressure within the core stays constant along the axis after the initial steep drop at the apex. Due to the large viscous diffusion at the inner core, the total pressure at the axis is low. Summarising, breakdown is caused by the adverse pressure gradient along the axis coupled with a low total pressure within the vortex core and occurs as follows.

1. Sudden deceleration of the fluid in the axial direction, caused by the adverse pressure gradient
2. Sometimes, at low velocity, the vortex deflects and enters a whirling motion about the central axis for a few turns.
3. The vortex breaks down to large-scale turbulence after external turbulent air enters the weakened vortex.

The most dominant factors that determine vortex bursting above a wing surface are the ratio of the swirling to the axial velocity component, the wing pressure gradient, wing sweep and incidence angle. The shape of the nose of the wing (for wings with sharp edges) appears to have little effect on the incidence at which breakdown occurs. Furthermore, the breakdown location for wings with sharp edges was found to be not very much dependent on the Reynolds number. For wings with blunt leading edges, the opposite holds.

On a surface streamline plot such as Figure 4.5 and 4.6 the vortex breakdown can be seen. At 10 degrees angle-of-attack, the vortex bursting occurs behind the trailing edge. The separation line is straight with a slight inboard curvature at the tip. For the condition at 20 degrees, the burst occurs above the wing ahead of station C (Figure 4.7). The secondary separation line is no longer straight but curves slightly outboard first before curving inboard.

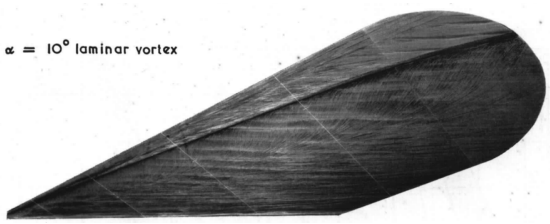

Figure 4.5: Streamlines on a 65 degree swept wing at α = 10° [44]

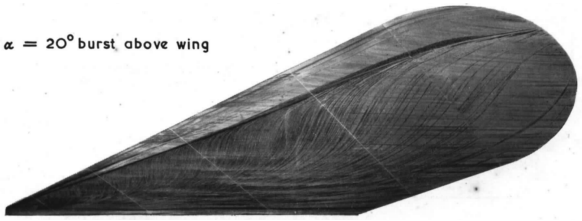

Figure 4.6: Streamlines on a 65 degree swept wing at α = 20° [44]

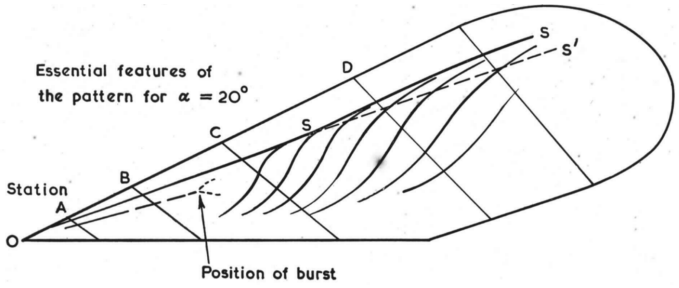

Figure 4.7: Effects of burst on surface lines [44]

The vortex breakdown can have large effects on the forces and moments around the aircraft. Breakdown location moves upstream with increasing angle-of-attack. Therefore, as stated by Pfnur [41], in the medium angle-of-attack range the increase in lift is gradually reduced due to the beginning of the vortex breakdown over the wing. However, this is contradicted by Kegelman, who states that there is only a weak coupling between vortex burst and lift. Kegelman measured the lift and burst location for thin sharp-edged delta wings with sweep angles of 55, 60, 65 and 70 degrees. He found that even with vortex burst as close as the apex of the wing, lift is still increased linearly [45]. When the breakdown leads to a reduction in lift on the rear wing sections, a considerable pitchup tendency is often observed.

If multiple vortices are acting on the wing, such as on a wing with discontinuity in wing sweep, usually the most inboard vortex breaks down first since it was formed first and has expanded the most [41]. This affects the stability of the remaining vortices, which merge with the wake of the burst inboard vortex. They consequently break down too. Note that while these results as observed by Pfnur are generally true for double delta wings, they might be different for a crescent wing. On crescent wings, very little research has been performed with regards to vortex bursting.

4.3. Leading Edge Vortices on Blunt Wings and Flying Wings

Since the geometry of the wing plays a crucial role in the formation, structure and breakdown of leading-edge vortices, it is important to investigate how they develop on flying wings in particular. This is especially necessary since flying wings have rounded leading edges which alter the way vortices are formed compared to wings with sharp leading edges.

4.3.1. Vortex Principles on Blunt Wings

The difference between the formation of the LEVs on wings with sharp leading edges and wings with blunt leading edges is illustrated in Figure 4.8. The vortices on the wing with blunt leading edge are formed further downstream compared to the wing with sharp leading edge. This can be attributed to the increase in upwash in spanwise direction typically found on delta wings. Further towards the wingtip, the upwash will result in a larger effective angle of attack which initiates the leading edge vortex. Besides the displacement of the origin, the LEVs are formed slightly after the leading edge (instead of precisely on the leading edge). This is because the flow remains attached longer due to the bluntness of the leading edge. Finally, the LEV does not originate strictly near a point, but rather it is gradually shaped along a longer portion of the leading edge. Thus, for a given angle of attack, the wing will feature attached flow near the root and separated vortex flow near the tip [46].

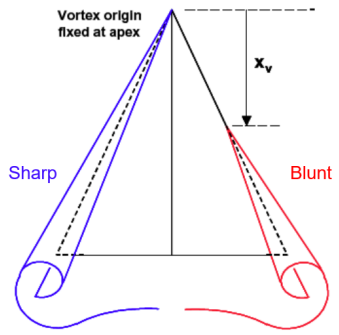

Figure 4.8: Comparison of sharp and blunt leading edge separation. [46]

Besides these topological changes in the formation of the LEVs, the vortex lift they generate is typically smaller compared to that formed by sharp wings. This is because the vortices are positioned over a smaller portion of the wing surface and their strength is weakened due to the blunt leading edge. Additionally, the LEVs are formed at higher angles of attack compared to wings with sharp edges. The sharp edge will promote separation quickly whereas for the same angle of attack the flow would remain attached over the wing with blunt edges. Because the principles of separation are influenced by the boundary layer over the blunt nose, there are also strong Reynolds number dependencies which were absent on LEVs formed by a sharp leading edge [46].

4.3.2. Reynolds Number Effects

While on sharp leading edges separation occurs almost instantaneously, blunt leading edges see a delay in separation in chordwise direction. The results of Crippa [47] indicate that the separation onset is dependent on the Reynolds number. The larger the Reynolds number, the later the flow separates from the surface to form the vortex. This can be seen in Figure 4.9 which presents the separation location as a function of angle of attack, with numerical and experimental data. This is also confirmed by Luckring [38], who investigated the Reynolds number effects. He found that for low Reynolds numbers (Re = 6 million) the flow remained attached until the 30% chord station. At 40%, the typical leading edge suction peak disappeared, and separation started. At high Reynolds numbers (Re = 60 million), this was observed at a 2° higher α. For the same α the flow remained attached until the 50% chord station. Luckring also noted that the leading edge suction peak increased with Reynolds number, until separation.

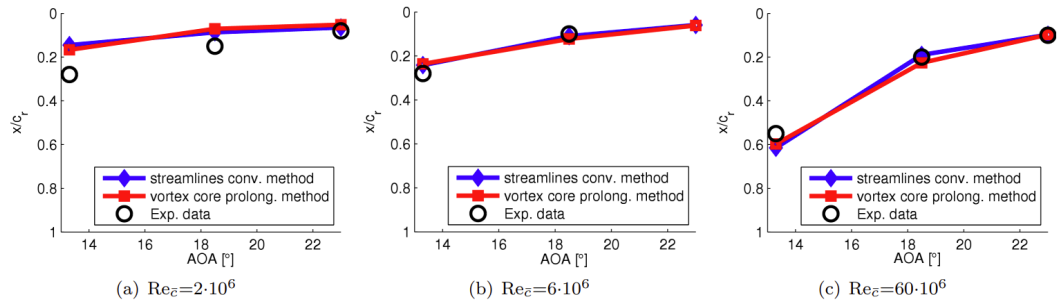

(a) $\mathrm{Re}_{\bar{c}}$=2·10^6 (b) $\mathrm{Re}_{\bar{c}}$=6·10^6 (c) $\mathrm{Re}_{\bar{c}}$=60·10^6

Figure 4.9: Vortex separation onset as function of angle of attack and Reynolds number for a blunt delta wing. [47]

4.3.3. Mach Number Effects

Besides the Reynolds number, there is also a Mach number effect. With increasing Mach number, the separation of the leading edge vortex is promoted. This is similar to the Mach effect on leading edge separation on an airfoil. Due to compressibility the pressure coefficients are increased over the airfoil. This results in a larger adverse pressure gradient after the point of minimum pressure. This promotes separation of the flow. The Mach number effect can be seen from Figure 4.10, where the LEV is already well developed over the wing at Mach 0.6, but just starting to develop at the rear of the wing at Mach 0.4. The Mach number thus has the opposite effect of the Reynolds number [46].

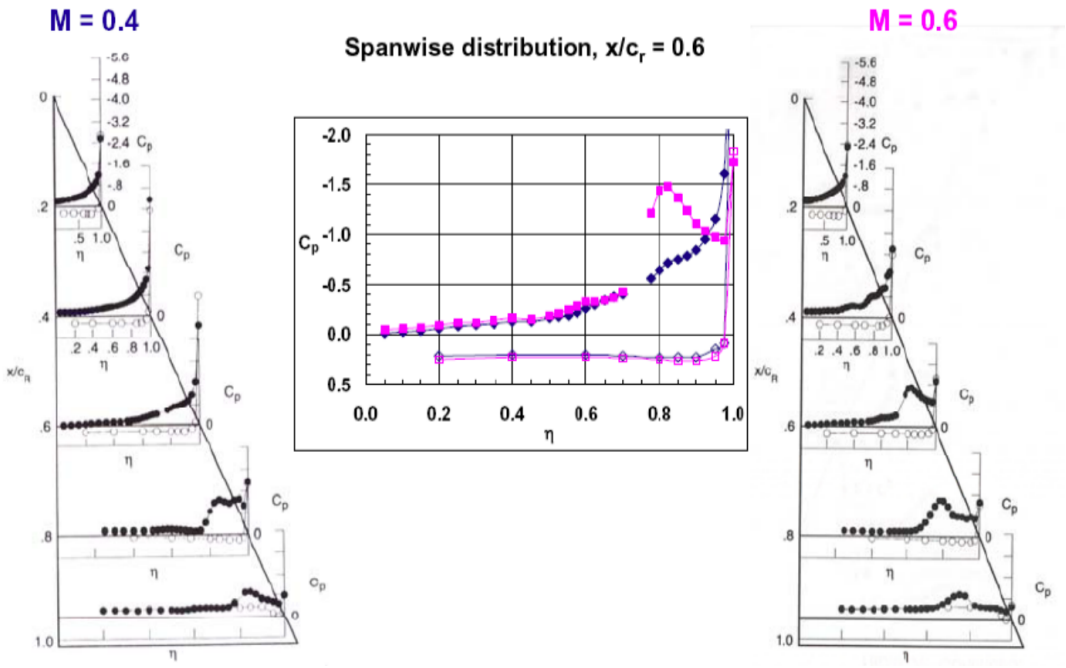

Figure 4.10: Compressibility effect on the formation of leading edge vortices for medium radius at $Re = 60 \cdot 10^6$ and α = 13°. [38]

4.3.4. Leading Edge Bluntness Effects

The roundness of the leading edge also influences the formation of the LEVs. The larger the leading edge curvature, the later the flow separation occurs. This can be seen from the data in Figure 4.11 which demonstrates this leading edge radius effect on the onset and progression of leading edge separation. The delay in separation due to Reynolds number is also shown. For large Reynolds numbers, the medium curvature and large curvature separation locations are nearly coincident. For a given angle of attack, the formation of the leading edge vortex thus happens at a larger chordwise position for increasing radius. While these results give some indication on the effects of the leading edge radius, the curvature on the Flying V wing might be larger and thus affect formation differently. This needs further examination.

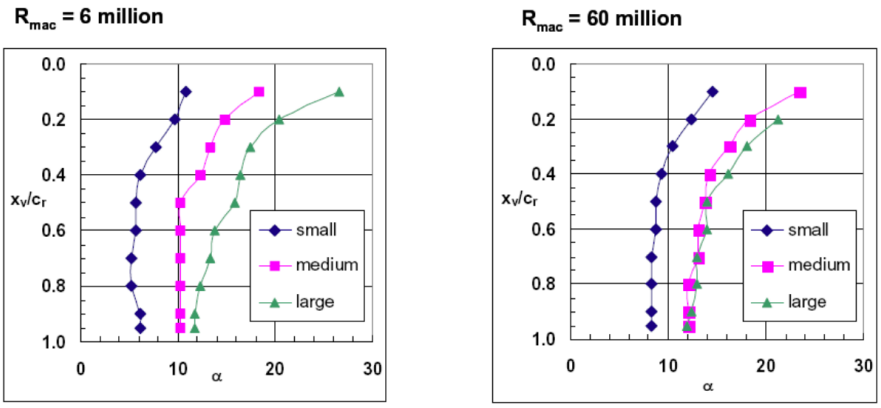

Figure 4.11: Leading edge radius effects for the onset and progression of leading edge separation at low and high Reynolds numbers at M = 0.4. [46]

4.3.5. Application to Flying Wings

While research on the topic of leading edge vortices on flying wings is scarce, several studies have been performed on blended wing body (BWB) configurations. Blended wing bodies are closely related to flying wings, with the main difference being a clearer distinction between fuselage and wing, while both function as a lifting surface [6]. Since these BWBs often feature blunt leading edges, they are a good topic of study to understand the vortical flow around flying wings. One popular example of these BWBs are the Uninhabited Combat Air Vehicles (UCAVs). Those have been developed in recent years and feature swept wings with rounded leading edges [46]. Since the wings are thicker than most delta wings, these configurations are referred to as 'semi-slender' in literature. For these semi-slender wings, the onset and progression of separated flow features distinctly different characteristics than those for sharp-edged slender wings. Therefore, numerous experimental and numerical simulations were carried out on such models.

The first of these models to highlight is the VFE-2 (Vortex Flow Experiment 2) model. This is a model of a delta wing with 65° sweep featuring four interchangeable leading edges with different radius of curvature. Different researchers such as Luckring [38] [48], Crippa [47], Hummel [49] and Konrath [50] have performed numerical and/or experimental simulations on this model. Crippa confirmed Luckring his hypothesis that wings with blunt leading edges under high angles of attack often feature multiple primary vortices above the wing surface. Using CFD, he also observed a double vortex system consisting of an inner and outer primary vortex as seen in Figure 4.12 which was first observed in wind tunnel experiments by Luckring.

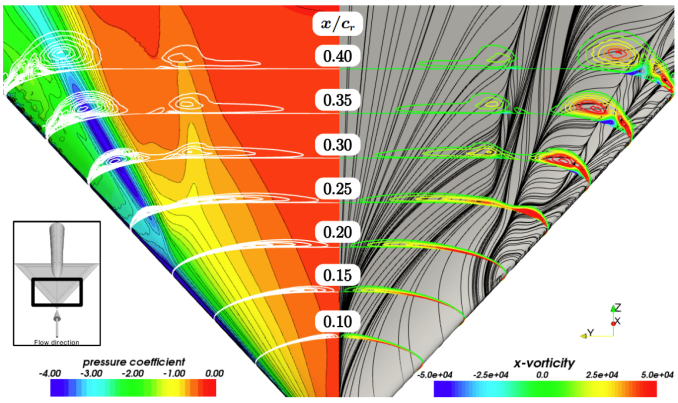

Figure 4.12: Surface pressure coefficient, x-vorticity and skin friction lines on the VFE-2 model at α = 18.5°, $Re = 60 \cdot 10^6$. [47]

The next research model is the SACCON, a blended wing body with a 53° sweep presented in Figure 4.13. The SACCON model is special because of its spanwise distribution of leading edge radius. The leading edge is very sharp at the root, then the radius is very large near the mid-span and again reduced towards the tip. This geometry leads to a complicated vortical flow. Towards the inboard, a primary inboard vortex is formed which is very similar to those found on sharp delta wings. Then, a second vortex is formed further mid-span at a higher angle of attack. Those two vortex systems interact with each other and cause severe nonlinear trends in the measured forces and moments [46, 51].

The pitching moment curve of the SACCON in Figure 4.14 is characterised by many nonlinear effects due to vortex formation and interaction. Since the wingtip has a sharper leading edge than midspan, a tip vortex is formed early. This increases local lift behind the center of gravity and causes the first decrease in pitching moment derivative. This tip vortex initially does not change location for 14°< α < 16° due to the increase of leading edge radius upstream. Hence a linear increase in pitching moment. Then, the formation of this tip vortex moves upstream with increasing angle of attack, which changes the sign of the pitching moment derivative. This happens simultaneously with the reduction of attached flow midboard. As the angle is further increased, the outboard leading edge vortex breaks down above the wingtip. This again increases the pitching moment derivative. From here, the breakdown location moves upstream. The wing loses lift and the pitching moment reduces [52].

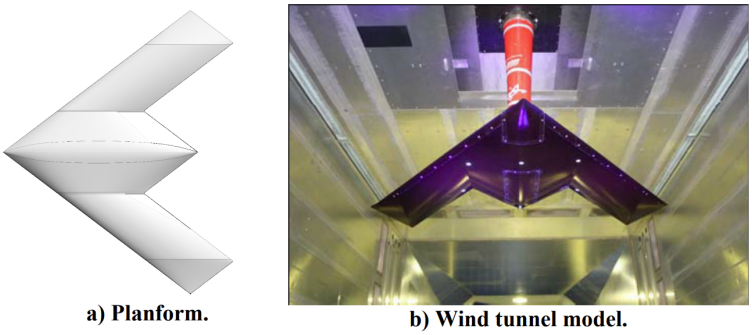

Figure 4.13: SACCON model [46]

In Figure 4.15, the intricate vortex aerodynamics at α = 15° are seen. Inboard, a large primary vortex (apex vortex) is present which is fed by vorticity coming from the sharp leading edge, up to the 35% chord station. Then, a second vortex (thickness vortex) is formed over the blunt part of the leading edge with its separation line clearly visible in black. Its vorticity sheet is connected to the apex vortex. On the wing tip, a relatively strong tip vortex is present due to the sharper leading edge. This vortex also pushes the thickness vortex inboard [52].

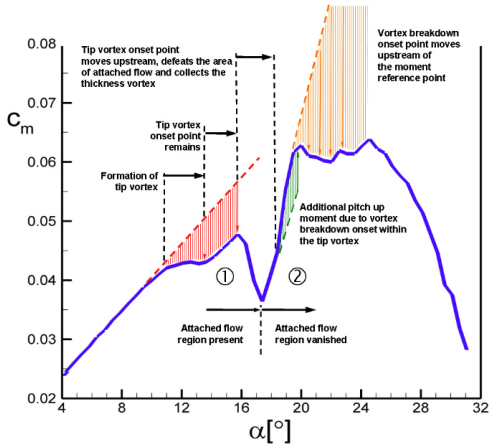

Figure 4.14: Pitching moment coefficient indicating different vortex effects. [52]

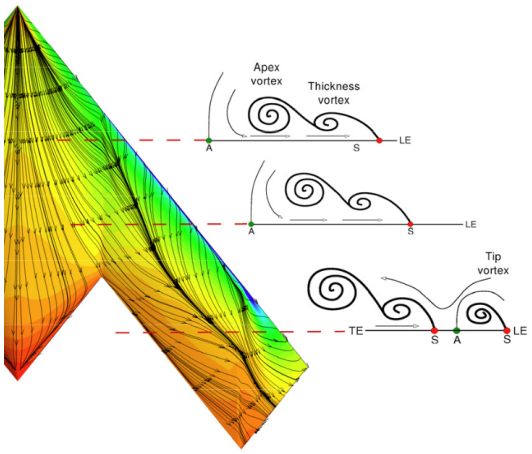

Figure 4.15: Flow topology at α = 15° obtained with CFD with pressure distribution and skin friction lines. M = 0.15, $Re = 1.6 \cdot 10^6$ [52]

The final model under research is a flying wing very similar to the SACCOON model, presented in Figure 4.16. While the wing sweep is the same as on the SACCON model, the leading edge radius is decreasing along the span. Kumar et al. [53] performed numerical and experimental simulations on this flying wing with 53° sweep and specifically addressed the breakdown phenomena of the LEVs on this wing. The results of Kumar et al. indicate that two strong primary leading edge vortices are formed above the upper surface for α > 10°. These vortices grow in size and strength with increasing angle-of-attack until an angle of α = 20°. At this point, the vortices suddenly lose a large part of their vorticity at the spanwise position of 0.5 x/c_r (Figure 4.16), indicating that the vortices have burst. A sudden enlargement of the LEV and a strongly decreased axial velocity was observed. The breakdown can also be seen on the surface streamlines in Figure 4.17 where the streamlines show a wave-like pattern.

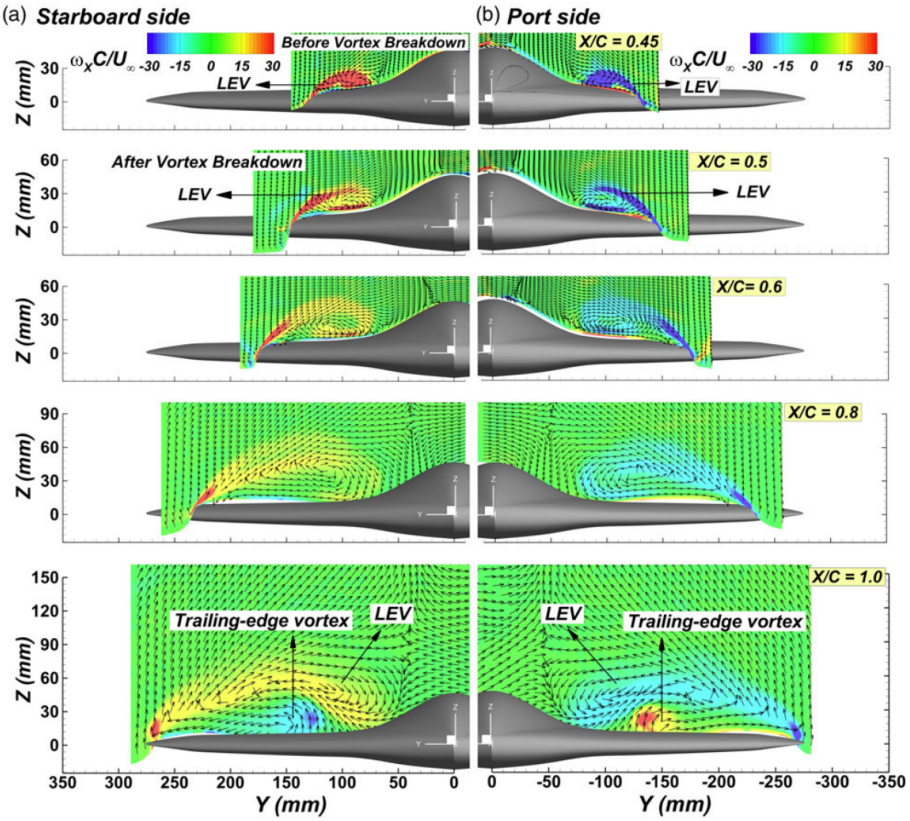

Figure 4.16: Velocity vectors and axial vorticity at different chordwise stations for a flying wing at α = 20° for $Re = 2.5 \cdot 10^5$ [53]

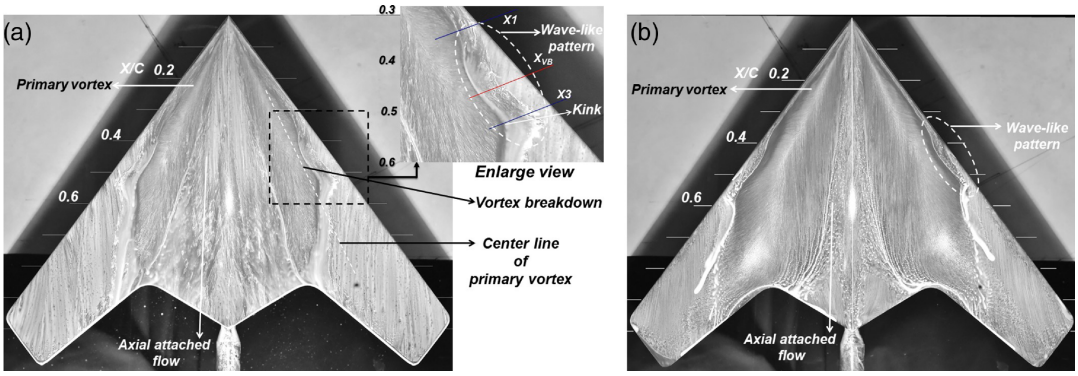

Figure 4.17: Surface oil visualisation on a flying wing at α = 20° for $Re = 2.5 \cdot 10^5$ (a) and $Re = 7.5 \cdot 10^5$ (b) [53]

Because of the LEV formation and breakdown, the lift curve of this model is nonlinear too (Figure 4.18). In fact, for every change in the topology of the LEV, the lift curve shows a change in slope and simultaneously the pitching moment derivative changes sign. First at α = 6°, there is some separation on the trailing-edge, reducing the lift curve slope. This reduction of lift at the rear of the wing results in an increase in pitching moment. Then at α = 10°, the LEV have fully developed with the addition of vortex lift. The increase in lift results in a decrease in pitching moment for this aircraft. Then for α > 15°, the lift curve slope reduces and the pitching moment increases due to flow separation and vortex breakdown approximately half-chord over the wing. Summarising, the pitching moment coefficient features a number of peaks and valleys which are interlinked with a change in topology of the LEV.

While the aforementioned research models all had blunt leading edges, none featured a kink in the leading edge like the Flying V. Therefore, the flow field is expected to be different on the Flying V. However, similar non-linear pitching moment behaviour can be expected. The effect of the wing kink, along

with its shape, is further explored in chapter 5. For now, it suffices to understand that the radius of the leading edge has severe consequences on the flow pattern at high angles of attack, leading to more but weaker vortices and complex flow interaction patterns that are very aircraft and planform dependent.

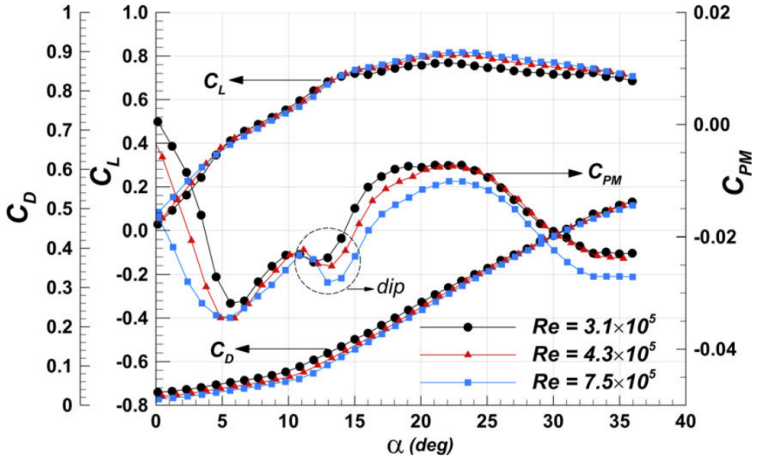

Figure 4.18: Aerodynamic coefficients on the flying wing tested by Kumar et al. [53]

4.4. Flow Control of Vortices

This section explores different techniques to counteract the negative effects of vortex breakdown and postpone these to larger angles of attack to increase the aircraft stability and controllability. Certain aircraft modifications such as an increased size of the vertical tail, leading edge flaps, aerodynamic add-ons, wing strakes and forebody modifications are all commonly used [41]. Most notably the wing strake, or leading edge extension, is featured on many fighter aircraft to help form stable leading edge vortices.

Additionally, there are active flow control techniques. Those effectively energise the vortical flows, for example by blowing a small jet into the vortex. This increases the momentum inside the vortex and delays breakdown. It gives the vortex greater stability and resistance to overcome the adverse pressure gradient. These active methods have been tried by Gutmark on delta wings and their results are documented in [43]. The active techniques have thus been extensively researched but are not used on aircraft due to their associated complexity, cost and safety risks.

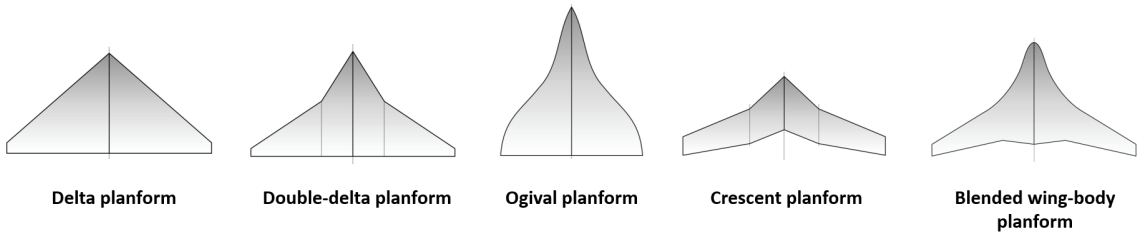

Figure 4.19: A selection of common and in development planforms with highly swept wings.

The final approach is one where the interaction of different leading edge vortices can be used to stabilise the primary leading edge vortex. Vortices will interact if they are in close proximity to one another. This can be achieved by modifying the wing planform and leading edge of the wing, as to promote the formation of a system of multiple vortices. Especially the variation in wing sweep plays a crucial role [41]. This can be smooth such as the ogival wing on Concorde or abrupt such as on the crescent wing of the Flying V [54]. Alternatively the leading edge shape can be changed. The wing juncture fillet is a geometric wing modification at a wing kink. A lot of research has been done on the effects of the wing planform on the vortex aerodynamics, especially the location of wing kinks [12, 55].

For example, recent research conducted by Ghoreyshi et al. investigated the effects of geometry changes on a double delta wing. The wing kink location was moved (x/c_r) as well as the sweep angles were varied. Results from experimental and numerical simulations showed that a high sweep angle and large chord ratio (kink moved forward) lead to a strong interaction between the IBV and OBV. Those wrap around one another immediately after the kink, causing a stabilisation of the stronger IBV. This results in a higher $C_{L_{max}}$ and delays breakdown to larger angles of attack [56]. The kink in the leading edge causes the formation of an outboard vortex of different vorticity. The two co-rotating vortices influence each other. In some cases, when the primary leading edge vortex has weakened, the outboard vortex pulls the inboard vortex towards the wingtip as can be seen on the first wing in Figure 4.20. This does not happen for the stronger primary vortex in the second wing which has a longer inboard wing.

The third wing (bottom left) features vortex breakdown at an x/c_r location of 0.25. This can be detected in two ways. Firstly, there is a change of the typical S-curved streamlines into diverging streamlines. Secondly, the attachment line curves outboard and then inboard again. Besides the visual indentification, Ghoreyshi et al also noted abrupt changes in the forces. A gradual lift force reduction is seen from α = 20° onwards, comparable to the separation behavior on thick airfoils. The breakdown location moves aft when the kink location moves aft. A pitch break was observed at α = 30°. In conclusion, the geometry of the wing planform plays a crucial role in the development, interaction and breakdown of LEVs.

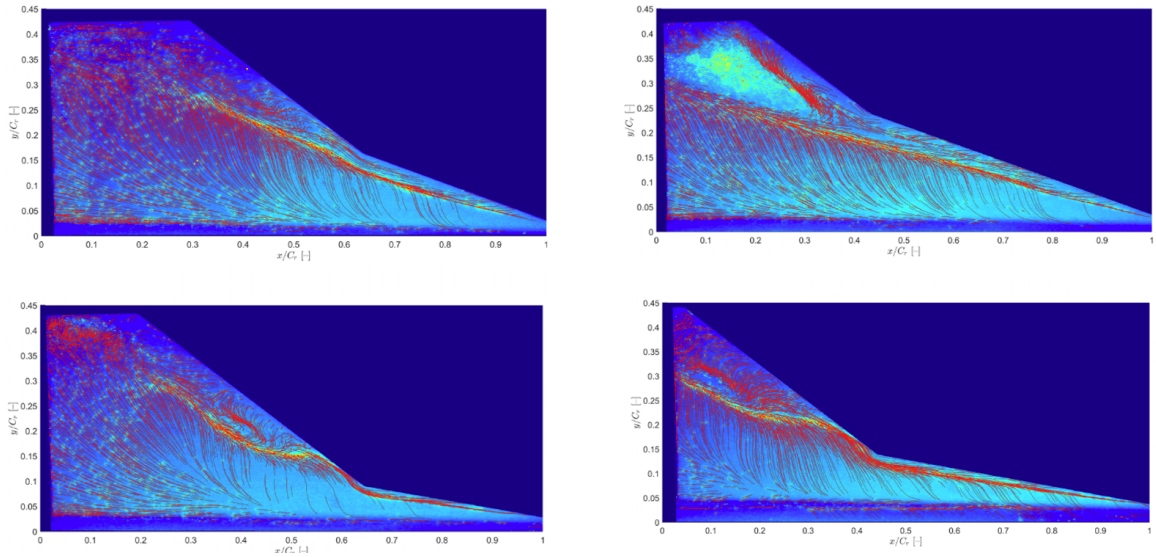

Figure 4.20: Surface oil flows on four different double delta wings at α = 20°. The upper two wings have 70° sweep, the lower wings have 80° sweep. The kink location changes from left to right. [56]

4.5. Numerical Solvers for Vortex Aerodynamics

This section explores different numerical methods that can be used to predict leading edge flow separation and breakdown of the LEVs. This is important to estimate the vortex topology and aircraft pitching moment of the Flying V, for different juncture fillet designs. This section begins with panel methods, followed by Euler, RANS, LES and hybrid RANS/LES methods, intended to give an overview of the possibilities and limitiations of each type.

Panel methods lie on the basis of numerical methods. They are based on potential flows and are not suited for vortical flow because they assume the flow is irrotational. Despite this, some researchers such as McCormick [57] have tried to implement semi-empirical corrections to account for vortex formation and bursting on very basic delta wings. These are based on the Polhamus equation to estimate the vortex lift. Those methods are meant for a quick and early assessment of the vortex lift and their validity is therefore very limited [57].

Next, there are Euler solvers which are based on the Euler equations. While those assume the flow is inviscid, the flow can be rotational. Since the effects of viscosity are neglected, Euler methods cannot accurately predict boundary layer behaviour or separation. Since the largest part of LEVs can be assumed to be primarily inviscid, Euler solvers can be used to model LEVs. This has been performed by numerous researchers such as Hsu, Hoeijmakers, Kern and Modiano [58, 59, 60, 61] on wings with sharp leading edges. In these cases the flow is known to separate on the leading edge and thus Euler solvers are capable of simulating the vortical flow patterns and vortex breakdown with good agreement to experimental data, given the grid is sufficiently fine. This idea is supported by O'neil's simulations [62], as shown in Figure 4.21, confirming that the formation and breakdown of LEVs are mostly influenced by factors that don't involve viscosity.

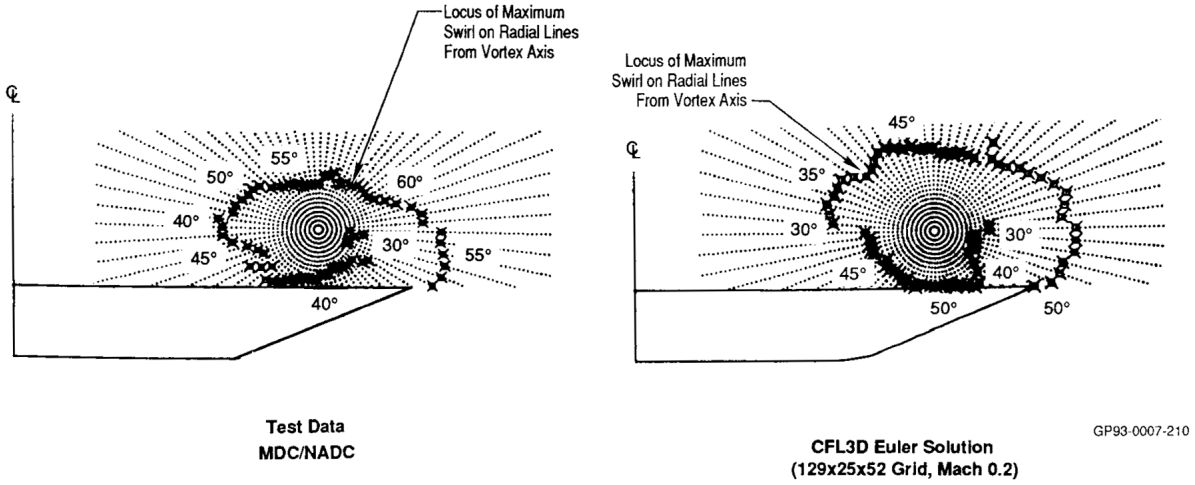

Figure 4.21: Comparison between Euler and test data for prediction of vortex shear layers for a 60° swept delta wing with sharp leading edge. The local swirl angle is annotated [62]

On wings with blunt leading edges, such as the NASA N2A Hybrid wing-body, the Euler solver was not able to predict separation. This results in a fully linear lift curve slope as seen in Figure 4.22. However, the Euler solver was found to show good agreement with experimental data for the ranges of angles of attack where the flow remained attached. Knowing that the lift curve slope of the Flying V is highly non-linear, the Euler equations do not provide sufficient accuracy to be used for simulating the vortical flow over the Flying V.

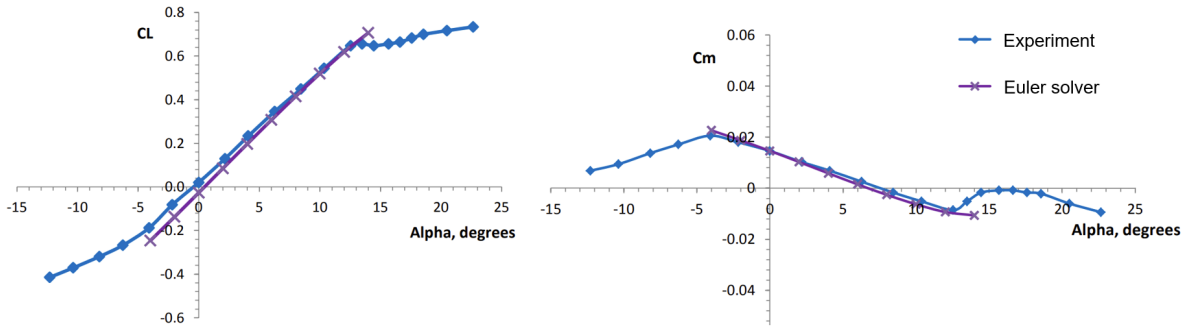

Figure 4.22: Lift coefficient and pitching moment coefficient comparison between Euler solver and experimental data for a hybrid wing-body aircraft [63]

When viscosity is to be taken into account, the Reynolds-Averaged Navier Stokes (RANS) equations can be used. RANS solvers solve the time-averaged form of the Navier-Stokes equations and are thus used to model steady flows. RANS methods solve the boundary layer equations and can therefore predict the onset of separation. They require the selection of a turbulence model, such as the $k-\omega$ model, and also require a structured mesh with sufficient mesh refinement at the surface of the model. A large number of researchers have used RANS to simulate vortical flow, also on wings with blunt

leading edges. Some notable examples are the work of Crippa [47] and Frink [64]. Crippa [47] used the RANS equations in combination with a $k-\omega$ turbulence model (coupled to the explicit algebraic Reynolds stress model (EARSM)) to model the flow around the VFE-2 wing. This wing has a blunt leading edge and 65° sweep. It was found that the $k-\omega$ model over-predicts the eddy viscosity within the vortex cores. This leads to an under-prediction of the suction peak associated with the primary vortex compared to the experimental data, as seen in Figure 4.23.

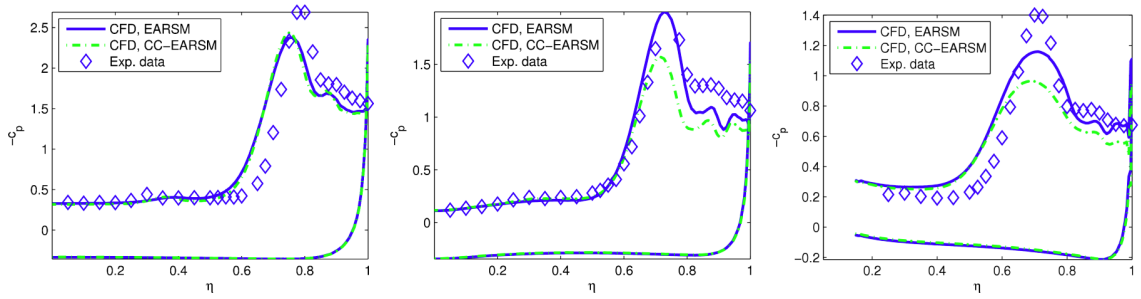

(a) $x/c_r = 0.4$ (b) $x/c_r = 0.6$ (c) $x/c_r = 0.8$

Figure 4.23: Comparison of spanwise pressure coefficient plots for 2 different RANS turbulence models at 3 chord-wise stations. [47]

Further, Frink [64] used RANS in combination with the Spalart-Almaras (SA) turbulence model to predict the vortical flow field over the SACCON model. Within RANS simulations, the choice of turbulence model and mesh size significantly impacts the accuracy of results. Different turbulence models feature different flow patterns over the aircraft (Figure 4.24) and therefore Frink also experimented with the k-ω and SST turbulence models. Frink found that it was extremely difficult to match the experimental data and correctly model the flow. He states that the correlation between the pitching moment and the experimental data was unsatisfactory, even at small angles of attack as seen in Figure 4.25. This is believed to be caused by excessive damping from over-production of turbulent viscosity. Similar results to these were presented by Chakravarthy et al. [65] who employed the SA and SST turbulence models on the SACCON wing. They found that neither of the two methods worked particularly well, with the SA model yielding slightly better results for the pitching moment, and the SST yielding better results for the lift coefficient. Apart from the SACCON wing, RANS has been used on the Flying V by Jorge [66] who also found that the numerical simulation did not match the experimental data well despite the enormous cost of a very fine mesh. This proves that, in conjunction with statements from Luckring [46], the complex flow over a blunt leading edge wing such as the SACCON or the Flying V is extremely difficult to model accurately using RANS.

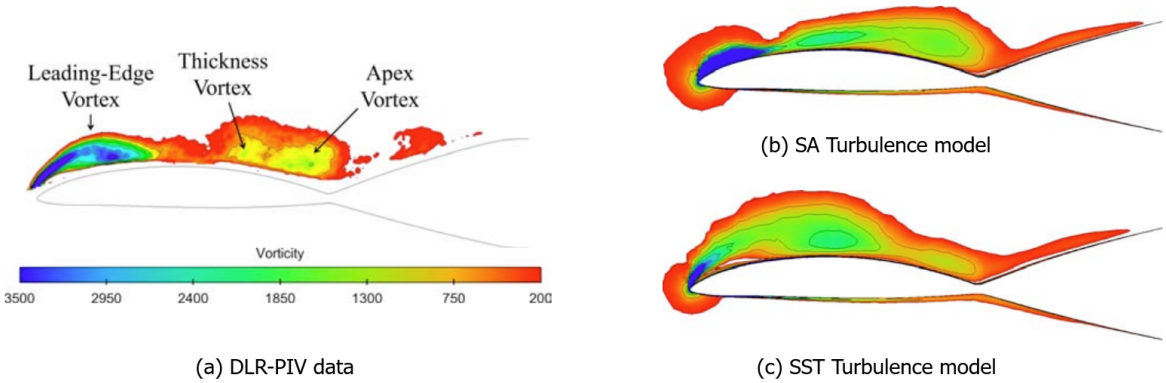

(a) DLR-PIV data (b) SA Turbulence model (c) SST Turbulence model

Figure 4.24: Effect of turbulence model on flow topology, compared with experimental PIV results on the SACCON wing. Adapted from [64]

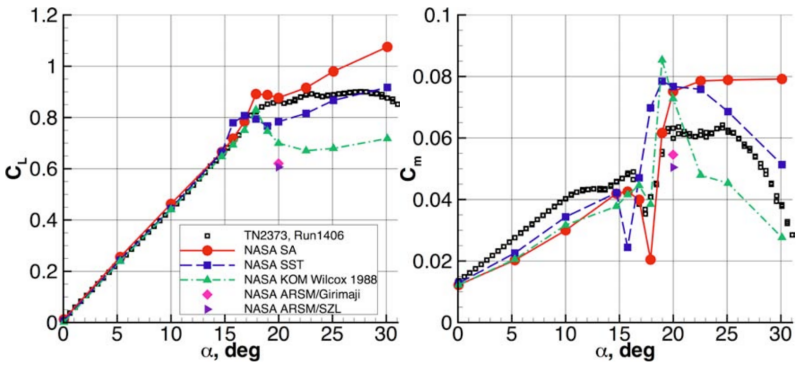

Figure 4.25: Effect of turbulence model on lift coefficient and pitching moment coefficient for RANS simulations on the SACCON wing. [47]

The final methods are the Large Eddy Simulations (LES). In LES, the large-scale turbulent structures in the flow field are resolved directly, while the smaller-scale turbulent fluctuations are modeled. By capturing the dynamics of large turbulent structures, LES can provide more insight into flow phenomena such as vortex interactions and flow separation. However, LES requires fine grid resolution to accurately capture the smallest turbulent structures, making it computationally expensive, especially for high Reynolds number flows or complex geometries. There also exist hybrid RANS-LES models such as the Delayed Detached-Eddy Simulation (DDES). In this model, a turbulence model is applied to the boundary layer region and LES is used for the separated regions. The approach is substantially less costly than LES, while it can achieve better accuracy than the RANS turbulence model for predicting separated flows [67]. It thus offers a good compromise between the accuracy of LES and the computationally more affordable RANS.

One such example is research performed by Ghoreshi [68] on the AVT-183 diamond wing with blunt leading edge presented in Figure 4.26. The AVT-183 diamond wing is based on the SACCON geometry but has a negative trailing edge sweep angle and a leading edge radius of 0.264% of the chord. The objective of this research was to determine the potential and limitations of current CFD methods for modeling vortical flow over a wing with blunt leading edge. The hybrid RANS/LES simulations revealed that attached flow can be accurately simulated, but the predictions are still not very good for high angles of attack. Ghoreyshi experimented with different turbulence models such as the Spalart-Allmaras (SA) model, Spalart-Allmaras with Rotation Correction (SARC), and Delayed Detached-Eddy Simulation (DDES) with SARC. The results demonstrated that the pitching moments found by the SARC turbulence model were more accurate compared to the SA model, at moderate angles of attack. However, large discrepancies were observed in pitching moment predictions at high angles of attack, as depicted in Figure 4.26. This research demonstrates that despite the increased cost with respect to RANS, the hybrid RANS/LES results are not always more accurate. Since LES is computationally expensive, it falls beyond the scope of this thesis.

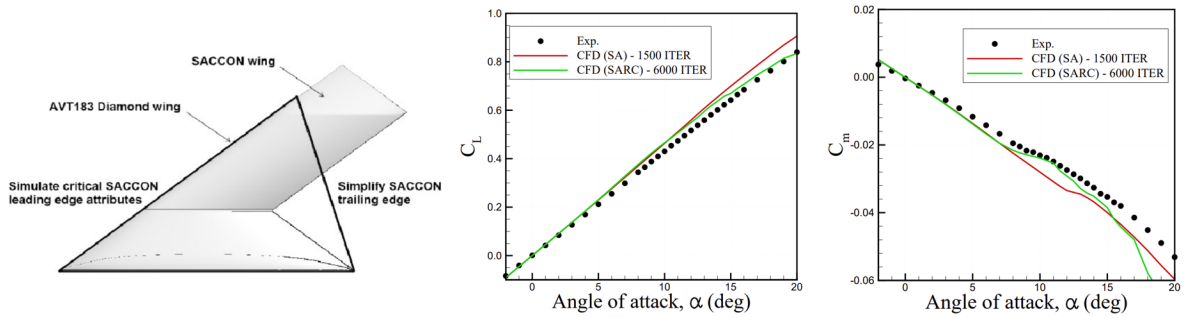

Figure 4.26: Lift coefficient and pitching moment coefficient comparison between experimental data and numerical simulation with SA and SARC turbulence models on the AVT-183. Adapted from [68]

5

Wing Juncture Fillet

The vortical flowfield that exists over highly swept wings at high angles of attack is complex, as discussed in chapter 4. For wings with a leading edge kink, extra pairs of primary vortices are formed, which interact with each other in an intricate manner. Sometimes, when the airflow in the core of the vortex has stagnated, vortex breakdown occurs. This effect has a negative impact on the flight characteristics of the aircraft, resulting in a loss of lift and abrupt nose up pitching moment. Consequently the need for flow control arises to delay these effects. In this chapter, one type of flow control is examined: the leading edge juncture fillet. The juncture fillet is a geometric modification to the leading edge at the location of a change in sweep. The chapter begins with presenting some common fillet shapes that have been previously researched. Then, in section 5.1, the effects of a wing juncture fillet on the aerodynamic forces is investigated. The effects on flow structure followed by vortex trajectory and breakdown for different fillet shapes are presented in section 5.2 and section 5.3. The chapter concludes with discussing the effects of the fillet size in section 5.4.

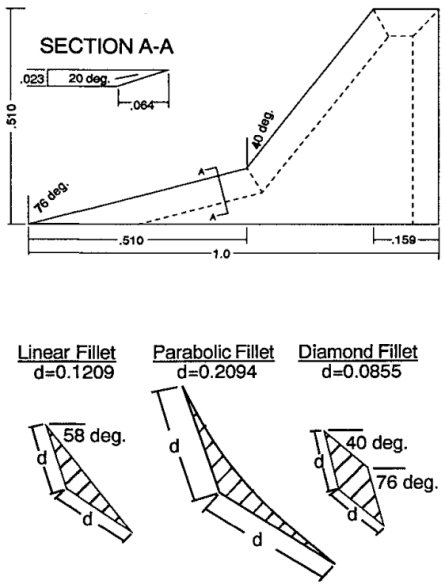

Figure 5.1: Fillet geometry used by Kern. [9]

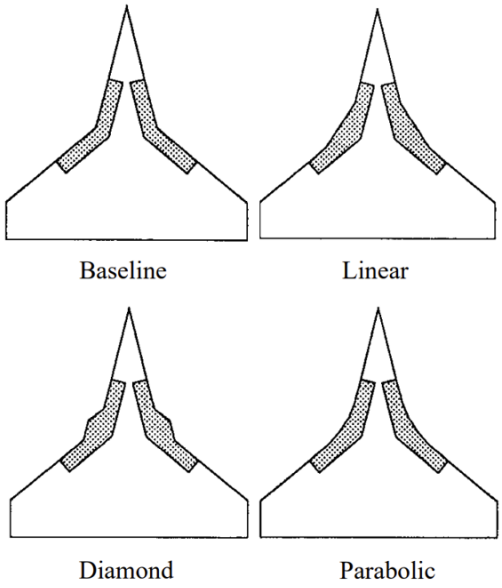

Figure 5.2: Fillet geometry used by Gonzalez. [69]

In literature, three main fillet shapes are commonly researched. Those are the parabolic fillet, linear fillet and diamond fillet presented in Figure 5.1 and 5.2. The parabolic fillet removes the discontinuity in wing sweep, while the linear and diamond fillet add new discontinuities in this region at which vortices are expected to originate. Different researchers such as Kern [9], Hebbar [10, 11, 12], Gonzalez [69, 70] and Ghee [71] have performed wind tunnel experiments and/or numerical simulations with such fillets, mostly on double delta wings with sharp leading edges. The wings presented in Figure 5.1 and 5.2 have a 76° sweep on the inboard wing (strake) and 40° sweep on the outboard wing. The fillets each are the size of 1% wing area.

5.1. Effects on Aerodynamic Forces

The different fillet shapes affect the forces and moments of the aircraft. In the research by Kern, the parabolic, linear and diamond fillet each added 13%, 13% and 14% more lift with respect to the baseline at α = 10° as observed in Figure 5.3. At a high angle of attack of 22.5° this became -4%, 13% and 18% respectively, with a reduction in lift for the parabolic fillet due to early vortex breakdown. Because the double delta wing used in this research featured a kink in front of the center of gravity, this reduction in lift also resulted in a reduction in pitching moment. Meanwhile, the pitching moment of the linear and diamond fillet increased with angle of attack. The increase in lift and pitching moment was mostly attributed to a higher suction peak at the junction. While Kern was one of the first to investigate the juncture fillet effects on a double delta wing, the results might not be very accurate due to the limitations of the numerical method used to acquire the presented results [9].

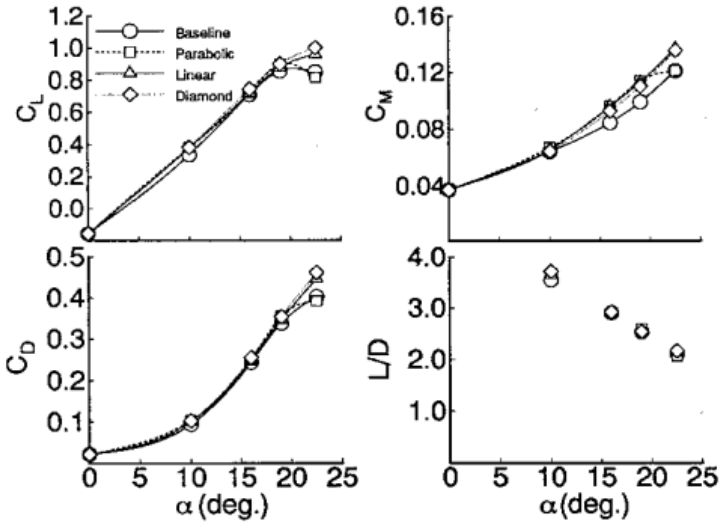

Figure 5.3: Forces and Moments for different fillets as simulated by Kern [9]

The measurements by Gonzalez were obtained by wind tunnel experimentation. He found that the parabolic fillet generated the largest lift coefficient and delayed the pitch-break the most, as seen on the lift and moment curves in Figure 5.4. This contradicts the results by Kern. The difference could be attributed to the different measurement methods and lack of accuracy of the older numerical methods used by Kern. After the pitch-break of the wing with parabolic fillet, the pitch-up moment increases quickly with angle of attack. The diamond fillet has the smoothest lift curve. The parabolic fillet resulted in an up to 39% larger lift coefficient. This was up to 29% for the linear fillet and 18% for the diamond fillet. The diamond fillet lift coefficient is larger than the linear fillet lift coefficient between α = 16° and α = 24°. The linear fillet generates more lift than the diamond fillet between α = 26° and α = 36°. The diamond and linear fillets only have small effects on the pitching moment [69]. Since the location of the wing kink on Flying V is behind the center of gravity, an increase in lift induced by the juncture fillet at its location would result in a reduction in pitching moment. This is a favourable characteristic. Therefore, it is expected that the increase in lift coefficient highlighted by Kern and Gonzalez would be favourable to postpone the pitch-break on the Flying V.

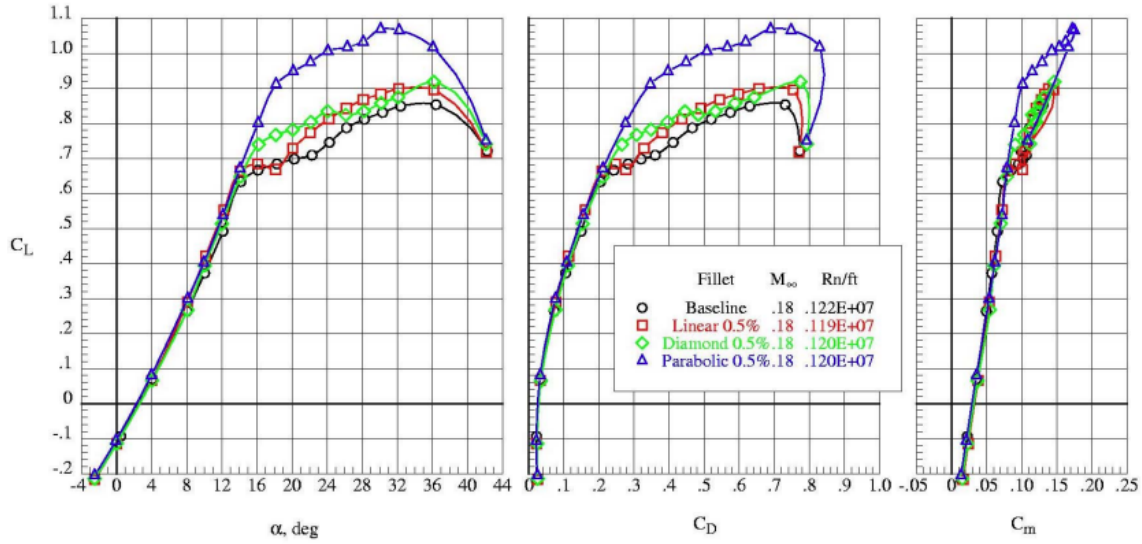

Figure 5.4: Forces and Moments for different fillets at M = 0.18 as measured by Gonzalez [69]

5.2. Effects on Flow Structure

The vortical flow structures are affected by the leading edge fillet. In the baseline configuration at moderate angles of attack (such as for α = 10° in figure 5.5), the inboard and outboard vortex exist concurrently. The outboard vortex (OBV) has a higher strength than the inboard vortex (IBV). Additionally, there is an interaction between the IBV and the OBV. The OBV is drawn towards the IBV, increasing the distance between the vortex core and the leading edge. Consequently, the connecting shear layer that sheds vorticity into the OBV must reach further. This phenomenon is called vortex-tearing.

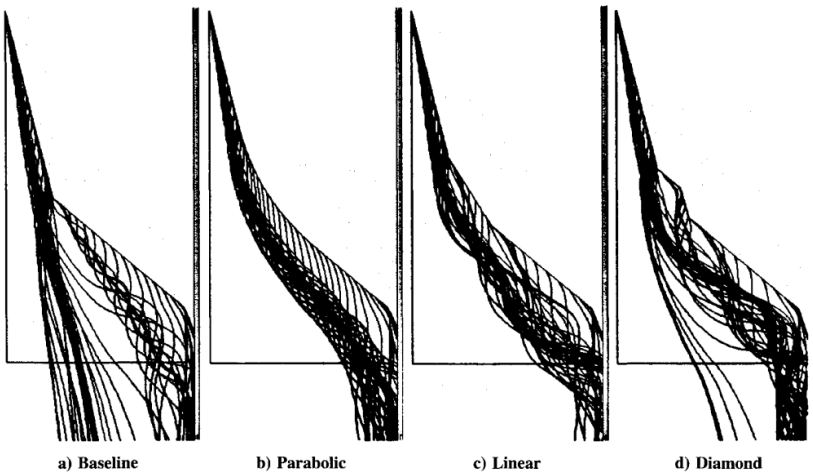

Figure 5.5: Vortical flow over a double delta wing at α = 10° and M = 0.3 for different fillets obtained with numerical simulation [9]

The parabolic fillet merges the two vortices, with the trajectory distinctly further towards the wingtip. The linear fillet caused the vortex feeding sheet to tear at the junction, generating an additional vortex. This fillet vortex first merges with the IBV, before merging with the OBV. The diamond fillet caused the same effect, the only difference being that the vortex shed by the diamond fillet merged faster with the IBV. All fillets moved the primary vortices outboard.

At high angles of attack such as for α = 22.5° in figure 5.6, the controlled primary vortices are not drawn so far outboard. The parabolic fillet again combined the vortex feeding sheets. The vorticity in the feeding sheet becomes stronger the more the sweep is decreased through the fillet. Thanks to the parabolic fillet, all the vorticity of the IBV also enters the vortex, making it more resistant to breakdown. The linear vortex generated a vortex that intertwined with the IBV. The IBV and OBV remained separated, but interacted with each other delaying breakdown too. The diamond fillet performed similarly to the linear fillet but postponed breakdown even further downstream. At angles of 27° and higher, the numerical code could not converge due to unsteadiness of the vortex breakdown point above the wing for all configurations.

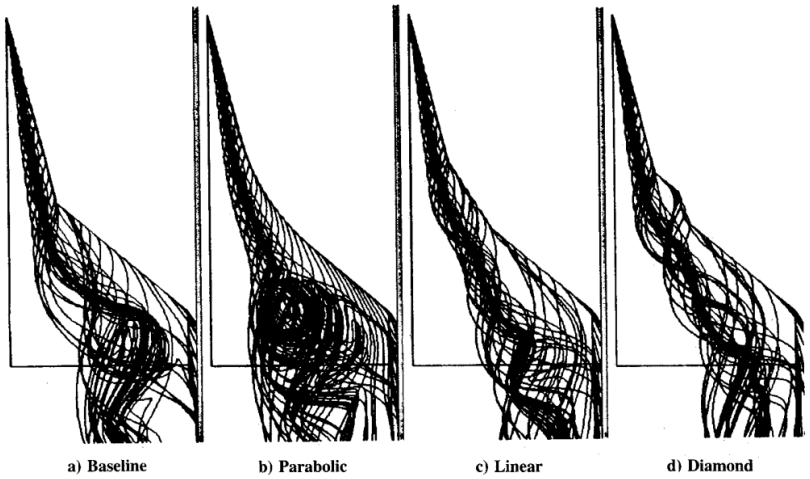

Figure 5.6: Vortical flow over a double delta wing at α = 22.5° and M = 0.3 for different fillets obtained with numerical simulation [9]

5.3. Effects on Vortex Trajectory and Breakdown

Knowing the typical flow structure, the trajectory of the vortex cores can be investigated. Hebbar states that the IBV and the OBV interact strongly, as suggested by Figure 5.7. As early as α = 10°, the IBV and OBV are well developped and coil up around each other. The IBV is initially conical, but is soon drawn outboard by the OBV. Simultaneously, the OBV also starts conical but after interacts with the IBV. The vortex cores do not merge into one single core. At the angle of α = 20°, vortex bursting occurs above the wing surface at 66% of the centerline chord. The IBV bursts first, and influenced by this, the OBV bursts soon after. Differences in burst location of the IBV are seen in Figure 5.8 for different fillet designs. The combined trajectory plots are more complex because of interaction with the newly formed fillet vortices. All fillets were found to delay the interaction as well as breakdown.

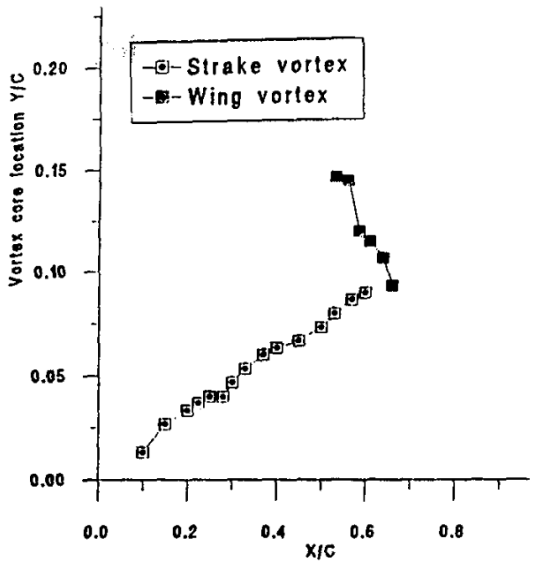

Figure 5.7: Core location IBV (strake vortex) and OBV (wing vortex) for baseline wing at α = 20°[11]

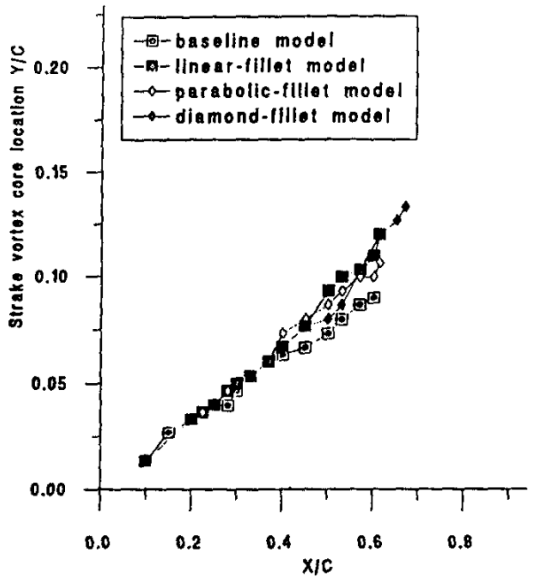

Figure 5.8: Core location of the IBV for different fillets at α = 20° [11]

Besides the vortex trajectory, the different fillets also had an effect on the location where vortex bursting occurred above the wing. The location of vortex burst with angle of attack for different fillets is given by Figure 5.9. The burst location rapidly moves forward with increasing angle of attack. The diamond fillet resulted in the largest delay in breakdown of as much as 8% chord-wise [12].

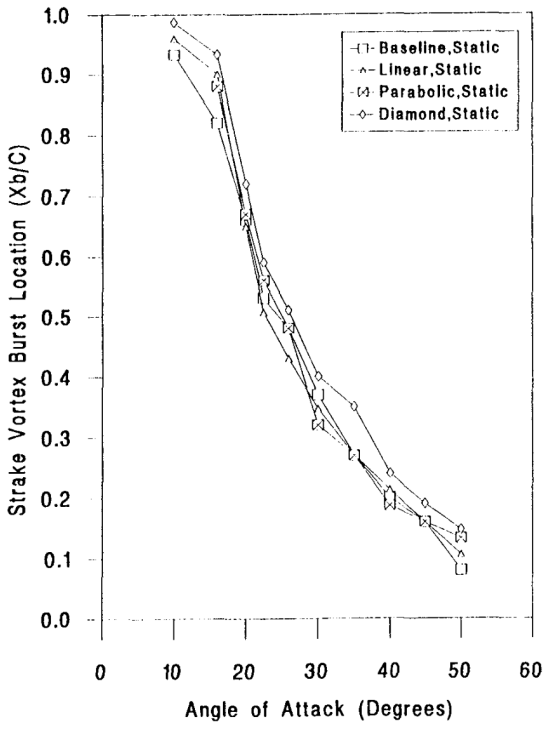

Figure 5.9: Effect of fillet shape on IBV burst location [10]

5.4. Effects of Fillet Size

Gonzalez also performed measurements for fillet shapes of different sizes with a surface area of 0.5%, 1% and 2.5%. The forces are given in Figure 5.10, 5.11 and 5.12. Gonzalez found that an increase in size leads to an increase in lift and pitching moment at angles above 14°. Drag also increases with angle of attack, but decreases for a given C_L. For the linear fillet, the size does not have a large effect on the lift after α = 30°. For the parabolic fillet, increasing the fillet size creates discontinuities. Gonzalez found this was caused by unsteady and oscillatory vortex bursting between the left and the right wing, which only happened at certain angles of attack. There is no data for the parabolic fillet of 2.5%-size because the fillet was too large to fit on the model [69]. While a lot of research has been conducted on sharp wings, no papers were found on the effects of juncture fillets on blunt wings and flying wings.

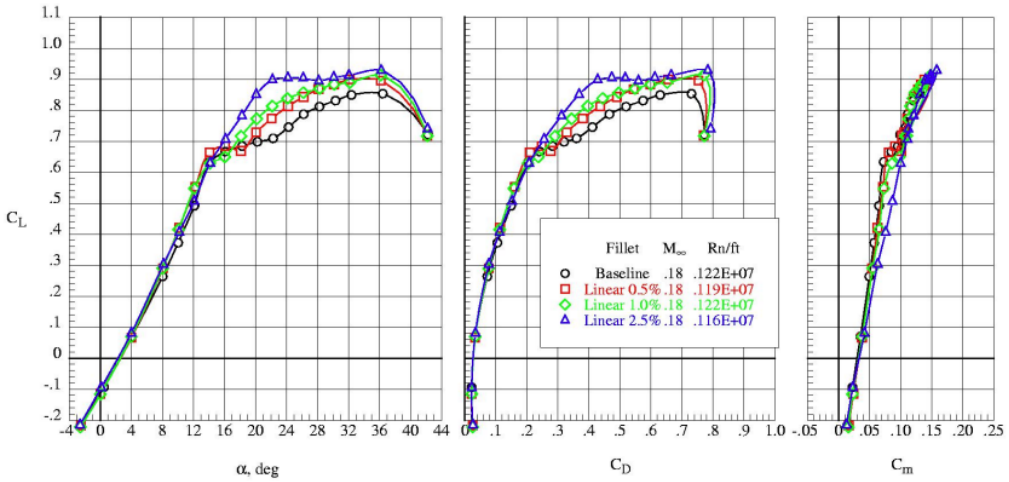

Figure 5.10: Effect of linear fillet size effect on forces at M=0.18. [69]

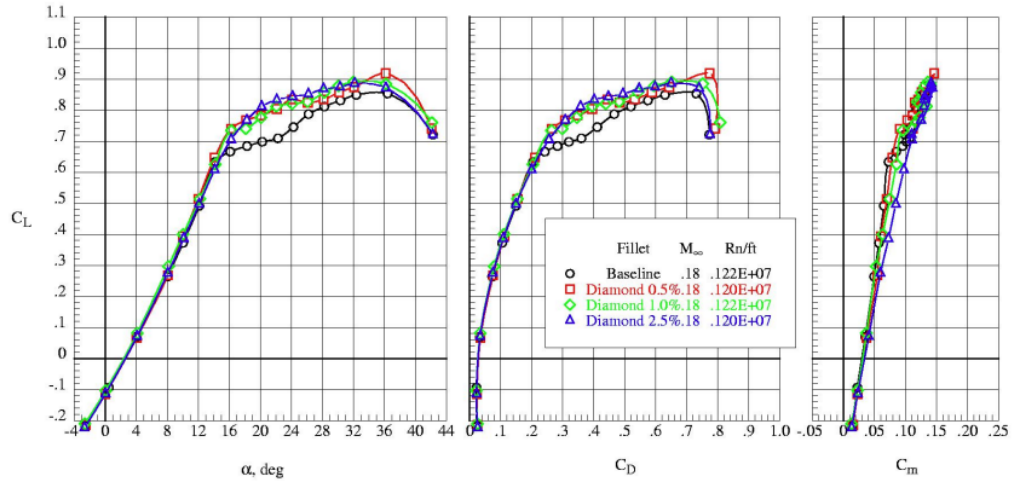

Figure 5.11: Effect of diamond fillet size effect on forces at M=0.18. [69]

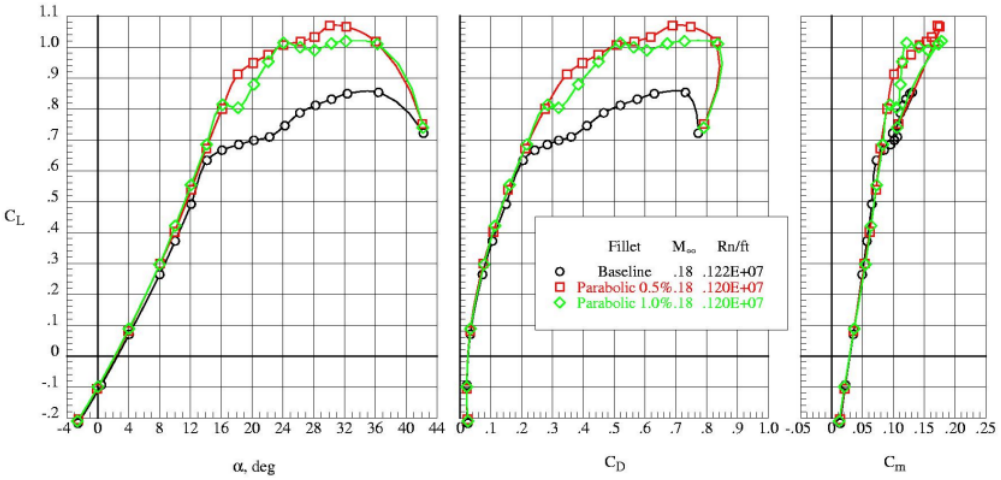

Figure 5.12: Effect of parabolic fillet size effect on forces at M=0.18. [69]

6

Wind Tunnel Experiment

Wind tunnel experimentation is a common research method used in aerospace engineering. It allows for the flow conditions to be simulated on a scale model instead of a full-scale aircraft. This is often utilised in conceptual and preliminary design to understand flow phenomena and the effect of design choices on the model. Wind tunnel experimentation can also be a more cost-effective alternative to full-scale flight testing, by allowing researchers to test a model under specific predetermined conditions.

In the research conducted with this thesis, a wind tunnel setup is used to quantify the effects of the juncture fillet design on the Flying V. This involves choosing the measurement techniques, visualisation techniques, and discussing similarity with the full-scale aircraft. All this requires thorough understanding of wind tunnel testing. This chapter begins with presenting the test facility and test model in section 6.1, followed by a discussion of the test conditions, similarity and wind tunnel corrections in section 6.2. Then, the principles of modern design of experiments are presented along with flow measurement techniques in section 6.3 and section 6.4 respectively.

6.1. Test Setup

This section presents the wind tunnel test facility and the wind tunnel model of the Flying V that will be used in the experiment.

6.1.1. Wind Tunnel Facility

The wind tunnel experiment will be carried out in the low turbulence tunnel (LTT) at the Delft University of Technology. This low speed low turbulence wind tunnel operates as a closed-throat, single-return atmospheric tunnel. It is presented in Figure 6.1. The wind tunnel takes up considerable space, with the fan and motor on the ground floor and the test section and settling chamber on the second floor. The six-bladed fan is driven by a 525 kW DC motor, enabling test section velocities of up to 120 m/s and a Reynolds number of up to 3.5 million. The tunnel's contraction ratio of 17.8 yields minimal free-stream turbulence levels as little as 0.015% at 20 m/s and 0.07% at 75 m/s. The corner vanes that rotate the flow in corners of the tunnel are cooled to control the properties of the flow. The wind tunnel features an interchangeable octagonal test section, which allows for the test section to be prepared while the tunnel remains operational. The test sections are 1.80m wide, 1.25m high and 2.60m long. The tunnel is equipped with a 6-component force balance, a 192 ports electronic pressure scanner system, hot wire anemometry and PIV systems [72].

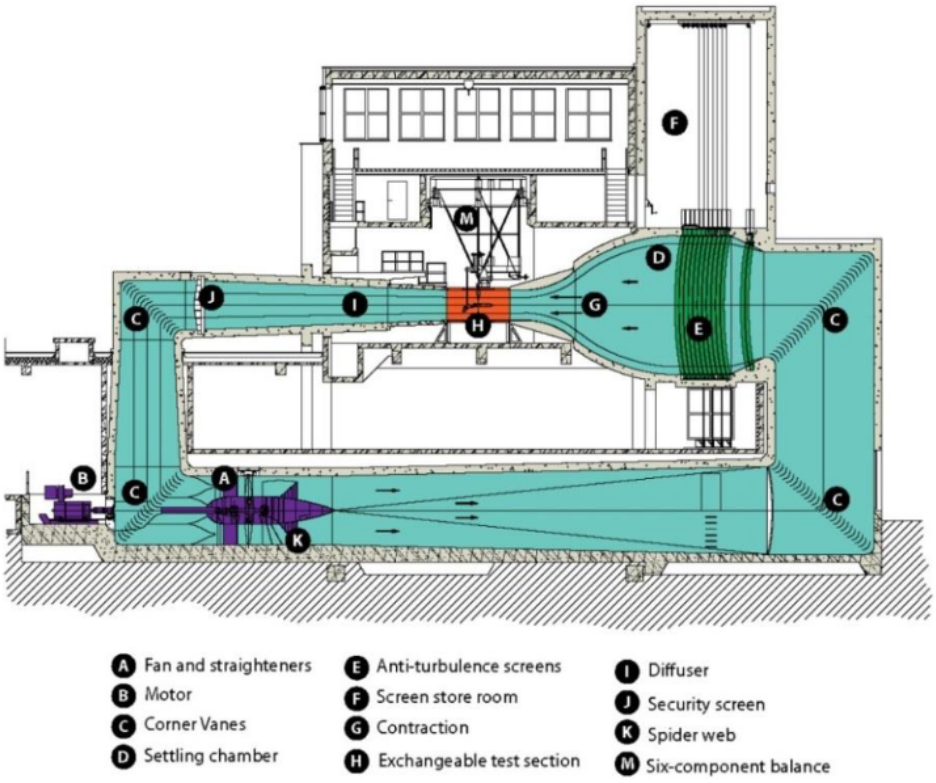

Figure 6.1: The Low turbulence wind tunnel facility at the TU Delft [72]

6.1.2. Flying V Model

The scale model of the Flying V is the FV-1000 based on the latest aerodynamic optimisation by Laar. The model has a scale of 1/54 (1.84%) and features interchangeable parts. The interchangeable parts allow for carrying out wind tunnel experiments with different geometries. One of the interchangeable parts is the juncture fillet, as seen in Figure 6.2. This part will be interchanged during the wind tunnel test campaign to evaluate the changes in the vortical structures over the Flying V for different juncture fillet designs.

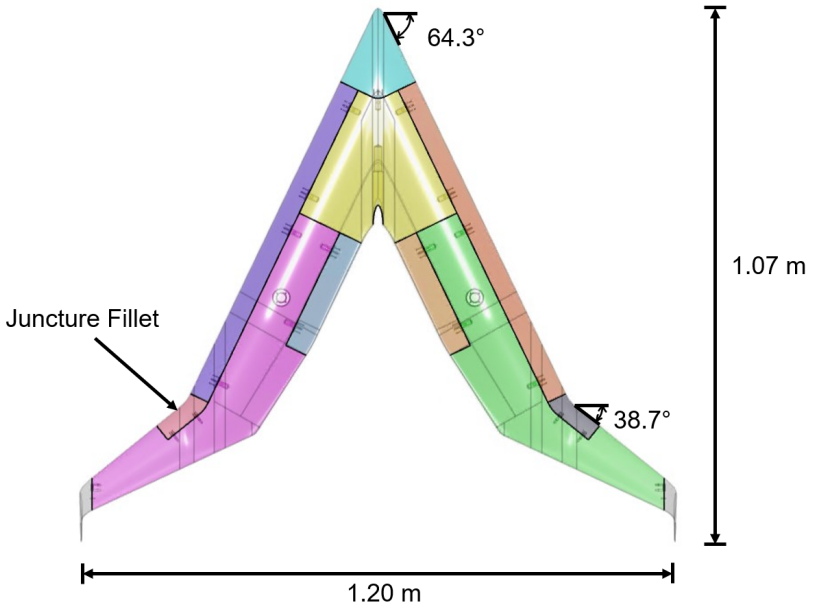

Figure 6.2: Top View of the Flying V wind tunnel model with interchangeable parts.

6.2. Test Conditions and Similarity

The wind tunnel test should be representative of the conditions that the full-size aircraft would experience in flight. In order to achieve this, a number of test conditions and similarity parameters must be determined. In order to relate results from the scaled model to the full-size aircraft, the so called similarity parameters need to be the same. There are a handful of similarity parameters, such as the Mach number, Reynolds number, Froude number and Strouhal number. Only the Mach number and Reynolds number are relevant, since the experiment does not deal with a body half-submersed in a fluid nor with any periodic motion.

6.2.1. Reynolds Number

The Reynolds number characterizes the ratio of inertial forces to viscous forces within a flow field and is defined by Equation 6.1. It is the most important similarity parameter in this study since the Reynolds number plays a role in many flow physics and aerodynamic phenomena, especially the boundary layer characteristics and separation patterns. The Reynolds number is thus expected to play a crucial role in the vortex aerodynamics around the Flying V. In order to accurately represent the flow patterns encountered by the aircraft in flight, the Reynolds number must be the same. Deviations from the free-flight Reynolds number can lead to significant discrepancies in aerodynamic forces and moments, compromising the reliability of wind tunnel results.

$$Re = \frac{\rho \cdot v_{app} \cdot c_{mac}}{\mu} \tag{6.1}$$

The full-size FV-1000 aircraft has a MAC of 18.74m. This results in a chord-based Reynolds number of 94.5 million according to Equation 6.1 using the approach speed of 74.6 m/s [73] . Knowing the wind tunnel can only maximally achieve a Reynolds number of 3.5 million, Reynolds number similarity cannot be attained. This has a number of consequences on the measurements. Firstly, the transition of the boundary layer over the surface of the wing from laminar to turbulent flow shall take place later. At lower Reynolds numbers in the wind tunnel, the wing surface shall thus have laminar flow over a larger portion of the chord. This discrepancy can alter the separation characteristics and flow attachment points, which have a large influence on the leading edge vortices. For this reason, tripping strips have been applied in previous wind tunnel tests with the Flying V [8, 33, 34]. These tripping strips artificially force the boundary layer into a turbulent state, which more closely resembles the flow in free-flight.

(a) Scaled **(b) Wind tunnel** **(c) Full-scale**

Figure 6.3: Total pressure loss on Flying V at α = 21.33°. $Re = 1.2 \cdot 10^6$ for the scaled case and $Re = 62.7 \cdot 10^6$ for the full-scale case. [66]

Besides the difference in transition, the scaled model will have a proportionally thicker boundary layer and a lower resistance to adverse pressure gradients. This greatly affects the regions of separation and attachment over the wing, which play a large role at high angles of attack. Highly swept wings are prone to leading edge separation at high angles of attack. This is significantly delayed on the full scale aircraft due to its higher resistance to the adverse pressure gradient, as can be seen in Figure 6.3 [66]. The leading edge vortices on the scale model are well developed, whereas the full-scale aircraft has only started to show leading edge vortices at the kink. Therefore, in wind tunnel testing with lower Reynolds numbers, the onset of flow separation and stall may occur at a lower angle of attack. This

can result in an underestimation of the maximum lift coefficient. These Reynolds number effects on the Flying V were quantified by Jorge [66], leading to corrections for the Reynolds number discrepancy between wind tunnel and free-flight, as are presented in Figure 6.4. The full scale aircraft can thus reach higher lift coefficients at lower drag values, and has a lower pitching moment compared to the wind tunnel model.

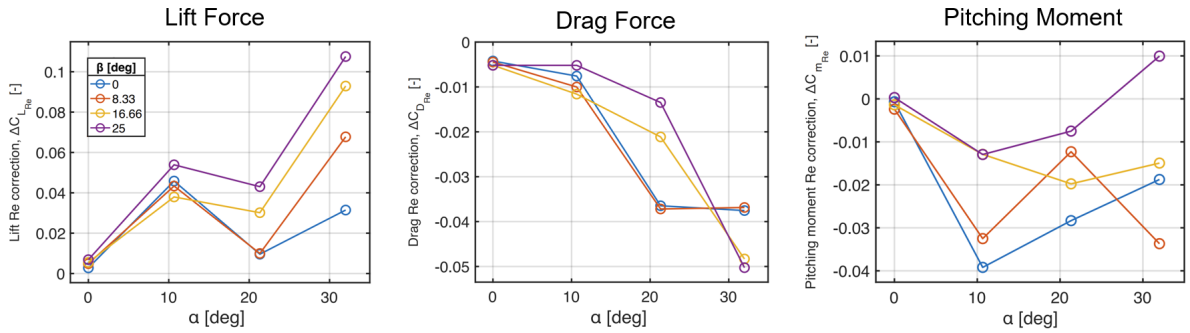

Figure 6.4: Correction for Reynolds number effects. [66]

6.2.2. Mach Number

Another important similarity parameter in wind tunnel testing is the Mach number, which quantifies the ratio of the flow velocity to the speed of sound in the fluid medium. Matching the Mach number between wind tunnel testing and actual flight conditions is essential for capturing compressibility effects and shock wave phenomena accurately. The Flying V's approach speed is estimated at 74.6 m/s in sea-level conditions at maximum landing weight. This approach speed is equal to 1.23 times the stall speed in landing configuration [73]. Using Equation 6.2, this results in a Mach number of 0.22. Since this Mach number is relatively small, the compressibility effects are not dominant. Therefore it is more important to achieve good Reynolds number similarity instead of Mach number similarity.

$$M = \frac{v}{a} \tag{6.2}$$

6.2.3. Wind Tunnel Corrections for Flying V

The presence of the wind tunnel walls and support struts can significantly influence the flow around the test model, leading to deviations in data measurements. This necessitates the application of wind tunnel corrections which subtract the effects of the walls and struts from the measured forces. Traditionally, the method of images has been used for such corrections. However, due the large differences in flow patterns with angle of attack on the Flying V, the method of images is not valid. This is because the method of images relies on the Laplace equation, which assumes that there is a large volume of irrotational flow between the model and the walls [66].

Antonio [66] proposes an improved thin-plate spline-based surrogate model for corrections, developed using RANS CFD to identify and quantify the wind tunnel effects on the flow field around the Flying V. His analysis found that the struts and walls confine the flow, leading to increased airspeed over the model. Consequently, measured lift and drag in the wind tunnel are overestimated compared to free-air conditions. This results in negative corrections for lift and drag as seen in Figure 6.5.

Furthermore, the investigation reveals a significant influence of walls on the leading edge vortices, resulting in premature vortex breakdown and lower stall angles in confined conditions compared to free-air. The walls confine the vorticity and restrict LEV expansion, while at the same time increase their suction [66]. Due to model blockage, the effective airspeed over the model is increased. The smaller airspeed after the model results in a larger adverse pressure gradient. This causes the vortices to breakdown sooner. Finally, when the vortical flow structure over the wing changes, there are irregular shifts in the resultant aerodynamic force location. This explains the irregular pitching moment corrections seen in Figure 6.5(e).

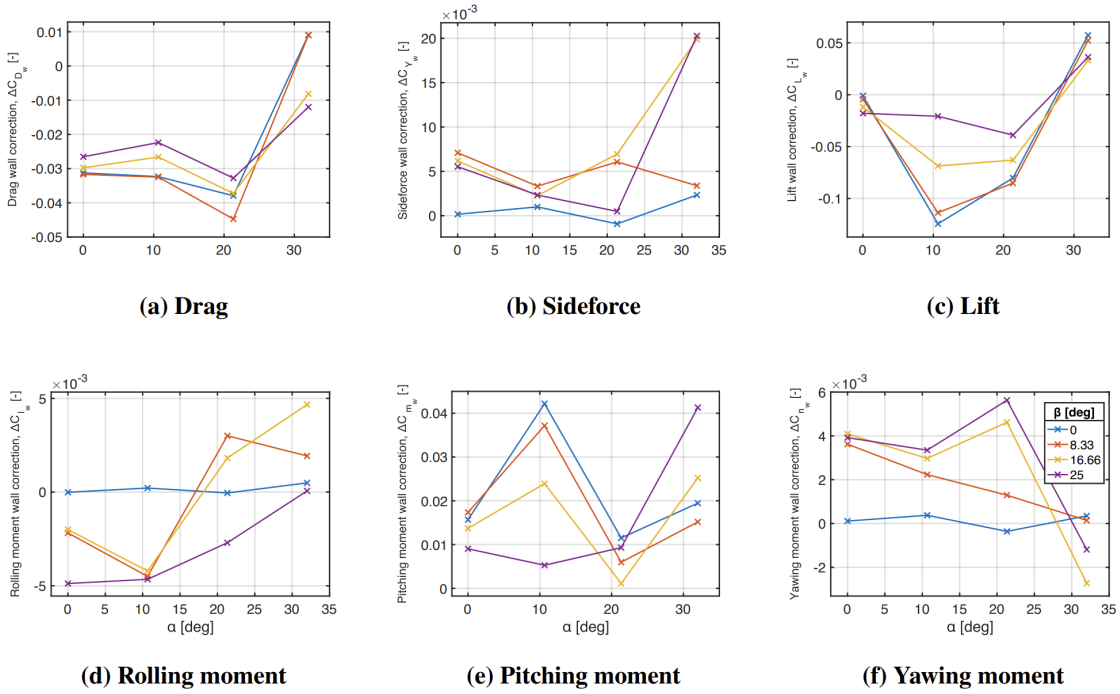

(a) Drag **(b) Sideforce** **(c) Lift**

(d) Rolling moment **(e) Pitching moment** **(f) Yawing moment**

Figure 6.5: Wind tunnel correction factors due to wall and strut effects. [66]

When using a spline interpolation on the force and moment corrections for different angles of attack and side-slip, a smooth surface is obtained, such as in Figure 6.6. While these wind tunnel corrections form a strong basis for estimating the flow on the full-scale aircraft, the accuracy of these predictions heavily relies on the reliability of the corrections. CFD simulations for highly rotational flow at large angles of attack are not very reliable as seen in section 4.5. Many non-linear aerodynamic effects are present on the Flying V and the CFD simulations were only performed for four different angles of attack. These factors combined could influence the reliability of the final results [66].

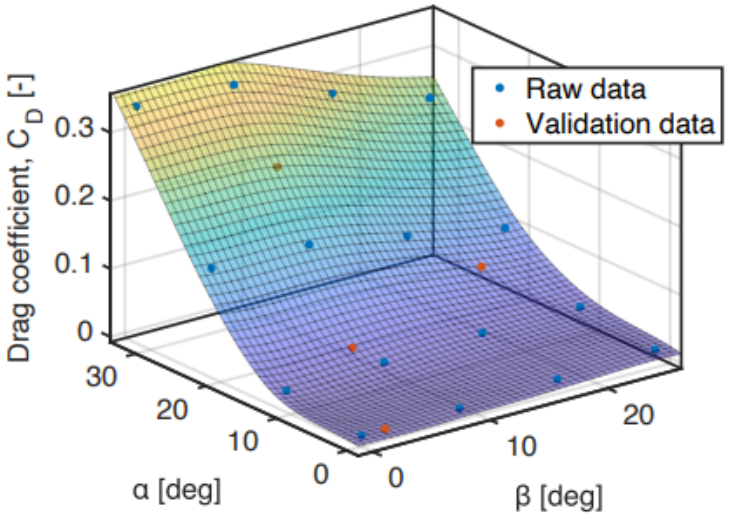

Figure 6.6: Obtained spline surface for the drag force of the scaled model [66]

6.3. Modern Design of Experiments

The design of many experimental simulations are often based on the One Factor At a Time (OFAT) method. This approach involves changing one independent variable, such as angle of attack, while keeping all other independent variables constant, such as Mach number, control surface deflection and angle of sideslip. While in this way the effects of a change of one specific variable can be precisely determined, it often leads to a large number of measurements samples to be taken in order to analyse the entire design space. Furthermore, traditional OFAT methods lack the ability to detect interaction effects, which arise from the combined influence of multiple independent variables. For example, changing the angle of attack changes the drag depending on the position of the outboard flap, indicating a two-way interaction between angle of attack and flap deflection. If this interaction differs at different Mach numbers, a three-way interaction arises among Mach number, angle of attack, and flap deflection. Such subtle high-order interactions are especially hard to detect with a OFAT approach and could be a reason for the variability in wind tunnel test results [74].

Unlike the traditional method of changing one factor at a time, Modern Design Of Experiments (MDOE) methods allow researchers to simultaneously manipulate multiple variables to efficiently explore the entire design space. This way interaction effects are better captured, while also reducing the wind tunnel test time. Design of experiments are also tightly related to the principles of replication and randomisation as explained by Barlow [75].

An experiment can be replicated to reduce the severeness of random errors. These are filtered out the more measurements are taken based on statistical principles. Contrarily, randomisation refers to taking measurement samples at random intervals or in a random order. This reduces the effects of uncontrollable factors such as sensor drift. For example, Gonzalez [69] found that when inverting the aircraft model in the wind tunnel test section and carrying out the same experiment, different results in the lift curve were found. Lower lift coefficients were measured overall. Gonzalez argues the difference could be caused by the force balance strut acting as a fence that decouples the left and right vortices of the delta wing, but this is not certain. Therefore replication is important to reveal such interaction effects which could induce a source of error to the results.

The interaction effects, if not properly quantified, could thus induce a substantial amount of error in predictions. Especially due to the increased need of precise predictions in the aerospace sector that could sometimes mean the difference between a commercially successful product or a less successful product. Previously correlations of 0.99 were viewed as sufficiently good fit to experimental data. Today those can be entirely inadequate to meet precision goals, such as in terms of drag counts. This emphasises the importance of MDOE practices and that these should be taken into consideration in the upcoming wind tunnel test campaign [74].

6.4. Flow Measurement and Visualisation Techniques

In this section, several flow measurement and visualization techniques are discussed, including tufts, oil flow visualization, smoke visualization, force balance, probe measurements (such as the 5-hole probe), wake rake, Pressure Sensitive Paint (PSP), Laser Doppler Velocimetry (LDV), and Particle Image Velocimetry (PIV).

6.4.1. Visualisation Techniques

Tufts: Tufts are simple yet effective to visualize airflow patterns around objects. These tufts consist of small pieces of yarn or ribbon attached to the surface of a model or structure. When subjected to airflow, the tufts align with the direction of the flow, providing a visual indication of flow direction and separation. Tufts are particularly useful for qualitative assessments of flow behavior, such as identifying flow attachment points, separation regions, and areas of reversed flow.

Oil Flow Visualization: Oil flow visualization involves applying a thin layer of oil or dye to the surface of a model or structure. As airflow passes over the surface, the oil or dye traces the flow patterns, revealing important information about boundary layer behavior, separation points, and flow attachment regions.

Smoke Visualization: Smoke visualization is a technique used to visualize airflow patterns off-surface. Smoke is injected into the flow field, either directly into the airstream or through smoke generators, producing visible streaks or plumes that follow the flow direction. By observing the movement and behavior of the smoke particles, researchers can gain insights into flow structures, turbulence intensity, and flow separation.

While smoke has been used by Viet [8], another noteworthy contribution on vortex smoke visualisation comes from Gutmark. Gutmark [43] used smoke in combination with a laser sheet illumination to observe the location of vortex breakdown on a delta wing. Gutmark aligned a laser sheet along the length of the vortex core, either from above the wing or from the side. Then, the location of breakdown can be seen and recorded on camera such as in Figure 6.7. The core appears as a dark area within the white vortical flow that stops at the breakdown location. While this is an effective way to visualise the vortex breakdown, it requires careful alignment of the laser sheet along the vortex core which changes location with angle of attack. For this reason Gutmark kept the angle of attack fixed at 15° while experimenting with active vortex control techniques.

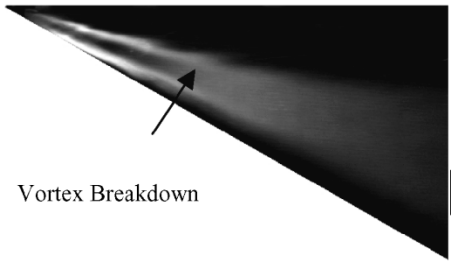

Figure 6.7: Smoke visualisation of the LEV on a delta wing as seen from above, with the aid of a laser screen parallel to the wing. [43]

6.4.2. Measurement Techniques

Force Balance: Force balance measurements involve mounting a model or test article on a balance system equipped with force sensors, such as the one fitted on the low turbulence tunnel (see Figure 6.1). As the model is subjected to airflow, the force balance system measures the aerodynamic forces acting on the model, including lift, drag, side forces and moments. Force balance measurements provide quantitative data on aerodynamic performance, allowing researchers to assess the effectiveness of different design configurations and control surfaces [75].

Pressure Taps: Pressure taps are small openings on the surface of the model that are used to measure local static pressure. Such pressure taps are usually aligned in either chordwise or spanwise direction so that the pressure distribution over the surface can be determined. Using pressure taps in a chordwise direction, regions of separation, attachment and shockwaves can be found. In spanwise direction, they can be used to detect the spanwise location and strength of leading edge vortices. Combining spanwise and chordwise directions allows for observing the interaction between vortices such as merging. This has been performed by researchers such as Luckring [38, 46, 48], Loeser [51] and Gonzalez [70] to analyse the leading edge vortices on their test model.

Probe Measurements: Probe measurements, such as those obtained using a 5-hole probe, are used to measure local off-surface flow properties, including velocity, pressure, and flow angle. The 5-hole probe, resembling of a pitot-tube, features multiple pressure ports arranged in a specific configuration, allowing for simultaneous measurement of static and total pressure at different orientations. By traversing the probe through the flow field, researchers can map out velocity vectors and pressure distributions. The path of the probe needs to be defined before the experiment, depending on the regions of interest that need to be captured. This involves programming the path into an automatic traverse system, while paying extra attention to not collide with the model [75].

Wake Rake: A wake rake is a specialized measurement tool consisting of an array of pressure taps or sensors mounted on a slender rod. The wake rake is positioned downstream of a model or test article to capture the flow characteristics in the wake region. By measuring the pressure and velocity distribution across the wake, researchers can analyze wake turbulence and gain insights into the drag build-up of the model. The pressure drag and skin friction drag can be estimated based on the velocity deficit in the wake, while the induced drag can be estimated by measuring the cross-flow energy [75, p 169].

Pressure Sensitive Paint (PSP): Pressure Sensitive Paint (PSP) is an optical measurement technique used to map surface pressure distributions on models and structures. PSP coatings contain luminescent molecules that emit light at different wavelengths in response to changes in surface pressure. By illuminating the coated surface with ultraviolet light and capturing the emitted light using a camera system, researchers can reconstruct pressure distributions with high spatial resolution, providing detailed pressure maps for aerodynamic analysis, as seen in Figure 6.8. This method has been employed by Gonzalez [70].

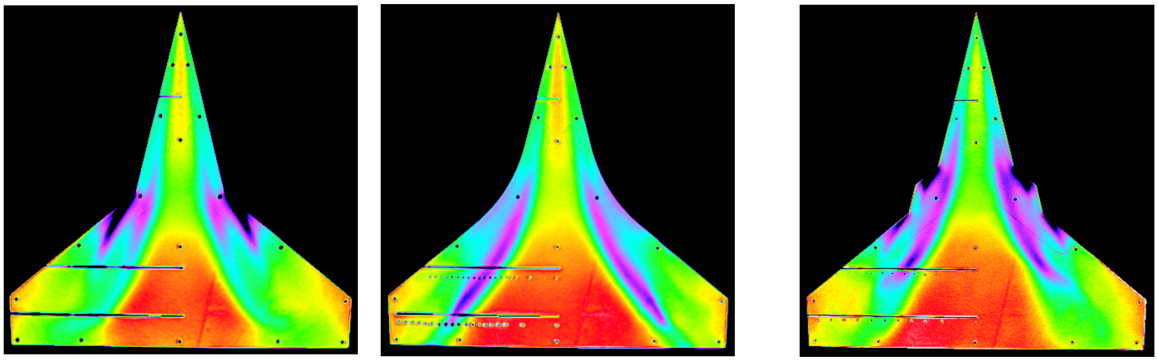

(a) Baseline (b) Parabolic fillet (c) Diamond fillet

Figure 6.8: Pressure sensitive paint results, after post-processing, for three different juncture fillets on a sharp double-delta wing [70]

Particle Image Velocimetry (PIV): Particle Image Velocimetry (PIV) is an optical measurement technique used to capture two-dimensional velocity fields in fluid flows. PIV systems illuminate the flow field with a laser light sheet and capture images of the flow using high-speed cameras. By seeding the flow with tracer particles, researchers can track particle displacement between successive image frames, allowing for the calculation of flow velocity vectors. PIV provides detailed velocity field data, enabling the visualization and analysis of flow structures, turbulence, and vorticity with as example Figure 6.9. PIV is used extensively for the quantification of vortex effects, as demonstrated by the work of Ghoreyshi and Presas [56, 76]. While PIV is able to gather extremely useful data, its setup and execution is more difficult, expensive and time-consuming than the aforementioned methods. The laser sheet needs to be precisely aligned with the model, and if different planes are to be analysed, the laser must be able to traverse to different locations. Sometimes, as found by Ghoreyshi [56], the laser reflects off the model into the camera, making it impossible to quantify the velocity vectors on some planes. After the experiment, the obtained data needs a large amount of post-processing to arrive at the desired flow contour plots.

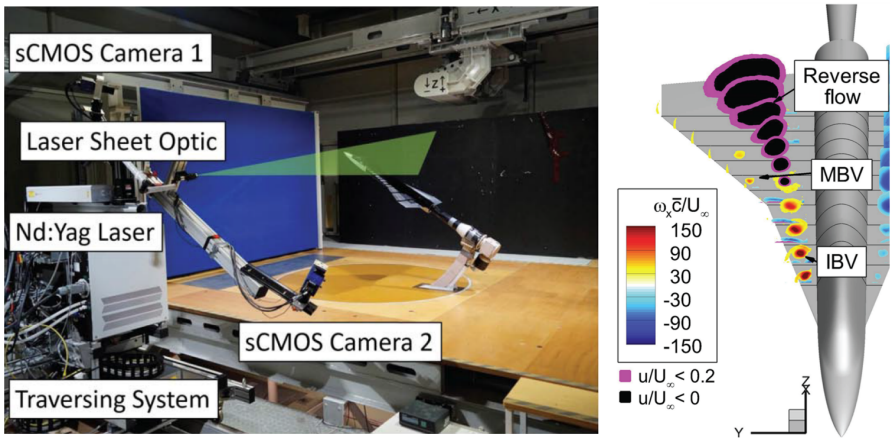

Figure 6.9: PIV setup and example of results for axial vorticity retrieved from [41]

Laser Doppler Velocimetry (LDV): Laser Doppler Velocimetry (LDV) is the predecessor of PIV, able to measure the velocity of the flow at specific points in the flow field. LDV systems use two laser beams to illuminate small seed particles suspended in the flow (such as atomised oil spray). By analyzing the Doppler shift in the backscattered light from the particles, LDV systems can determine the velocity of the flow at the measurement point. After the experiment, the wind tunnel needs cleaning to remove the seed particles contamination. Many older papers from the 1990s and early 2000s feature results obtained with LDV such as those by Gutmark [43]. However, since LDV is limited to single-point measurements at a time, it has been phased out in favour of PIV [77].

7

Research Outline

The research began with a literature study. The focus of the literature study lied in the understanding of the principles of leading edge vortices, the application of wing juncture fillets and wind tunnel experimentation techniques. The literature study aids in the next steps of the thesis to provide answers to the research questions from section 2.3.

After the literature study, the main research question shall be answered by means of a wind tunnel test campaign. For this test campaign, different juncture fillets will be designed and tested. First, different juncture fillet shapes will be chosen based on literature and their effects on the flow topology and forces over the Flying V will be determined. This will be done by creating a Computer Aided Design (CAD) model of a number of different fillet shapes in the Dassault Systèmes 3DExperience modelling software. Those will be installed on the latest Flying V parametric model of Laar [18, 19]. Their effects on the aerodynamic forces will be analysed to get a first idea of how they perform. The analysis shall be done by means of a numerical simulation using Computational Fluid Dynamics (CFD) software. Based on the results of these simulations, the three most promising shapes will be chosen.

Then, the most promising fillet shapes will be further refined using Computer Aided Design (CAD) in order to improve their performance where possible. This could be done by altering their geometry and cross-section. These modifications will be tested using a manual design loop of CAD and CFD, as much as time allows. The fillet shapes that delay the pitch-break the most will be selected, as they are of most interest for further analysis. It should be pointed out that a design optimisation is not the goal of the thesis, but rather the fillet models should be sufficiently developed such that they yield realistic and credible results for accurate comparison between different types.

Finally, the best performing fillet shapes will be tested in the Low Turbulence wind tunnel at the Delft University of Technology. The wind tunnel test campaign aims to demonstrate the differences in flow structure and quantify the pitching moment characteristics caused by the different juncture fillets on the Flying V. When the wind tunnel campaign is finished, the data of the tests will be compared with the numerical results. The results of the wind tunnel data will thus be used as a validation tool for the CFD simulations.

8

Conclusion

The need for sustainable aviation requires fundamentally new aircraft configurations to reduce carbon emissions. This, amongst progress in technology readiness, lead to an increased interest in flying wings and blended wing bodies. One of these, the Flying V, has been in development at the TU Delft since 2016. The aircraft, designed to replace conventional tube-and-wing aircraft, has its cabin and wings in a distinct V-shape. It promises to reduce fuel consumption and carbon emissions by 20% thanks to a reduction in wetted surface area.

This literature study began with exploring the concept of flying wings and the aerodynamic consequences of blunt leading edges at high angles of attack. While leading edge vortices (LEVs) form, papers proved that on blunt wings the flow was very complex and often featured a handful of leading edge vortices simultaneously acting above the wing surface. The formation of the vortices was delayed with both pitch angle and chord-wise location compared to wings with sharp leading edges. The vortices interacted with one another in an intricate manner and as the pitch angle was increased, the vortices moved upstream and often merged and gained strength until an abrupt change occurred known as breakdown. In all researched papers, breakdown was always associated with a sudden change in pitching moment and thus unfavourable. Furthermore, the formation of the LEVs was found to be promoted with increasing Mach number but delayed with increasing Reynolds number. This should be taken into account to achieve better similarity in wind tunnel testing.

Next, the concept and effects of a juncture fillet were explored. A juncture fillet is an aerodynamic modification of the wing kink, used to control the vortex flow at high angles of attack. This flow control device was found to improve the handling characteristics of delta wings with sharp leading edges, increasing its lift coefficient and often delaying the pitch-break. A parabolicallly shaped juncture fillet was found to delay pitch-break the most by merging the inboard and outboard vortices and combining the vortex feeding sheets. On other test models, the diamond fillet moved the burst location furthest aft, by up to 8%. While lots of experimentation was performed on wings with sharp edges, no research was found where juncture fillets were applied to a thick, blunt wing with leading edge kink. However, the literature study demonstrated that juncture fillets could delay the pitch-break and are thus worth pursuing.

The effects of the wing juncture fillet could be demonstrated in a wind tunnel by a combination of visualisation methods and measurement techniques. Among the four primary visualization techniques — tufts, oil flow, smoke, and smoke-laser combination — the latter was found to be the most effective in showing important vortical flow aspects such as trajectory and breakdown location. Looking at the measurement techniques, the force balance proved to be essential in capturing the pitching moment. Besides this, researchers have used many different techniques, such as pressure taps and pressure-sensitive paint. Those were deemed unfeasible for the current research due to practical limitations (model and tunnel). Therefore, it was concluded that force measurements in combination with probe measurements or PIV could be used to capture the vortical flowfield around the Flying V. Both PIV and probe measurements are capable of measuring important vortex parameters such as vorticity with PIV capturing a larger domain (surface data instead of point-wise data) at cost of complexity and time. Given practical constraints such as test time, PIV experimentation in this thesis would likely be limited to a single plane, if feasible at all.

Finally, the literature study showed that the numerical solvers available for a medium-fidelity, fast evaluation of the juncture fillet designs are scarce and lack accuracy. Since the most important aspect of this research is to quantify the effects of the juncture fillet designs, a precise simulation of each condition is not strictly a necessity, but rather is an accurate representation of the change in flow and forces for each design. Since Euler equations are not capable of predicting vortex phenomena well for wings with blunt leading edges, the Reynolds-Averaged Navier Stokes (RANS) equations were found to be best suited, despite their larger computational cost.

In conclusion, a reshaped juncture fillet could be a possible solution to delay the pitch-break on the Flying V, but this is yet to be proven. There exist numerous wind tunnel experimentation techniques to quantify the vortical flow field and determine the relationship between the juncture fillet design and the pitching moment. Using those, in combination with RANS simulation, the effects of the juncture fillet design on the pitching moment of the Flying V could be determined, bringing the Flying V one step closer to a viable design.

References

[1] ICAO. *On Board a Sustainable Future*. 2016. URL: https://www.icao.int/environmental-protection/Documents/ICAOEnvironmental_Brochure-1UP_Final.pdf (visited on 03/18/2024).

[2] H. Ritchie. *Climate change and flying: what share of global CO2 emissions come from aviation?* 2020. URL: https://ourworldindata.org/co2-emissions-from-aviation (visited on 03/18/2024).

[3] Net Zero Tracker. *Net Zero Stocktake 2023*. 2023. URL: https://www.zerotracker.net/analysis/net-zero-stocktake-2023 (visited on 03/18/2024).

[4] E. Torenbeek. *Advanced Aircraft Design: Conceptual Design, Technology and Optimization of Subsonic Civil Airplanes.* 1st ed. Wiley, 2013.

[5] P. D. Bravo-Mosquera, F. M. Catalano, and D. W. Zingg. "Unconventional aircraft for civil aviation: A review of concepts and design methodologies". In: *Progress in Aerospace Sciences* 131 (May 2022). ISSN: 03760421. DOI: 10.1016/j.paerosci.2022.100813.

[6] W. Bishop. "The Development of Tailless Aircraft and Flying Wings". In: *Journal of the Royal Aeronautical Society* 65.612 (1961), pp. 799–806. DOI: 10.1017/s0368393100075957.

[7] J. Benad and R. Vos. "Design of a Flying V Subsonic Transport". In: *33rd Congress of the International Council of the Aeronautical Sciences* (2022). Available at http://resolver.tudelft.nl/uuid:95ea413d-d5b1-4cb2-a650-828cb106dbbd. ISSN: ISSN 2958-4647.

[8] R. Viet. *Analysis of the flight characteristics of a highly swept cranked flying wing by means of an experimental test*. Master's thesis. Available at http://resolver.tudelft.nl/uuid:90de4d9e-70ae-4efc-bd0a-7426a0a669c3. Mar. 2019.

[9] S.B. Kern. "Vortex Flow Control Using Fillets on a Double-Delta Wing". In: *Journal of Aircraft* 30.6 (1993). DOI: 10.2514/3.46422.

[10] S. Hebbar, M., and A. Khozam. "Investigation into the effects of juncture fillets on the vortical flow over a cropped, double-delta wing". In: *32nd Aerospace Sciences Meeting and Exhibit*. 1994. DOI: 10.2514/6.1994-626.

[11] S. Hebbar, M. Platzer, and A. Khozam. "Experimental investigation of vortex flow control using juncture fillets on a cropped double-delta wing". In: *33rd Aerospace Sciences Meeting and Exhibit*. 1995. DOI: 10.2514/6.1995-649.

[12] S. Hebbar, M. Platzer, and W. Chang. "Juncture fillets for vortex flow control on double-delta wings undergoing sideslip". In: 34th Aerospace Sciences Meeting and Exhibit, 1996. DOI: 10.2514/6.1996-663.

[13] M.V. Ciminera. *The Aircraft Designers*. American Institute of Aeronautics and Astronautics Inc., 2013. ISBN: 978-1-62410-694-1.

[14] National Museum of the United States Air Force. *Northrop YB-49*. URL: https://www.nationalmuseum.af.mil/Visit/Museum-Exhibits/Fact-Sheets/Display/Article/858861/northrop-yb-49/ (visited on 02/28/2024).

[15] R. Martínez-Val. "Flying Wings. A New Paradigm for Civil Aviation?" In: *Acta Polytechnica* 47.1 (2007).

[16] R. Martínez-Val et al. "Conceptual design of a medium size flying wing". In: *Proceedings of the Institution of Mechanical Engineers, Part G: Journal of Aerospace Engineering* 221 (1 2007), pp. 57–66. ISSN: 09544100. DOI: 10.1243/09544100JAERO90.

[17] J. Benad. "The Flying V - A new Aircraft Configuration for Commercial Passenger Transport". In: *Deutsche Gesellschaft für Luft- und Raumfahrt - Lilienthal-Oberth e.V.* (2015). DOI: 10.25967/370094.

[18] Y. Laar. *Aerodynamic Design of a Flying V Aircraft in Transonic Conditions*. Master's thesis. Available at http://resolver.tudelft.nl/uuid:591093b2-5cdc-41c5-b564-3786f43d51db. Oct. 2023.

[19] Y. Laar et al. "Aerodynamic Design of a Flying V Aircraft in Transonic Conditions". In: AIAA SCITECH 2024 Forum, 2024. DOI: 10.2514/6.2024-2669.

[20] S. Eftekhar. *High Lift Split Flaps for the Flying-V*. Master's thesis. Available at http://resolver.tudelft.nl/uuid:0ad3c088-b6a6-472b-b60b-4b424a08e15c. Jan. 2024.

[21] J. Treat, E. Conant, and K. Nowakowski. *Take a look inside the Flying-V*. 2021. URL: https://www.nationalgeographic.com/magazine/graphics/take-a-look-inside-the-flying-v-feature (visited on 01/23/2024).

[22] J. Benad and R. Vos. *The technology behind the Flying-V*. 2022. URL: https://www.tudelft.nl/lr/flying-v/technologie (visited on 01/23/2024).

[23] M. Claeys. *Flying V and Reference Aircraft Structural Analysis and Mass Comparison*. Master's thesis. Available at http://resolver.tudelft.nl/uuid:ee7f2ecb-cdb6-46de-8b57-d55b89f8c7e6. Aug. 2018.

[24] T. Dotman. *A structural sizing methodology for the wing-fuselage of the Flying-V*. Master's thesis. Available at http://resolver.tudelft.nl/uuid:69e21e65-7168-4f83-abf5-b646bb4c7fe5. Dec. 2021.

[25] M. Desiderio et al. "Crashworthiness of the Flying-V Aircraft Concept with Vertical Drop Test Simulations". In: Aerospace Structural Impact Dynamics International Conference ASIDIC, 2023. DOI: 10.31224/3034.

[26] W. J. Oosterom. *Flying-V Family Design*. Master's thesis. Available at http://resolver.tudelft.nl/uuid:9e8f9a41-8830-405d-8676-c46bf6b07891. Apr. 2021.

[27] W.J. Oosterom and R. Vos. "Conceptual Design of a Flying-V Aircraft Family". In: AIAA AVIATION 2022 Forum, 2022. DOI: 10.2514/6.2022-3200.

[28] F. Faggiano et al. "Aerodynamic design of a flying V aircraft". In: American Institute of Aeronautics and Astronautics Inc, AIAA, 2017, p. 3589. ISBN: 9781624105081. DOI: 10.2514/6.2017-3589.

[29] M. Hillen. *Parametrisation of the Flying-V Outer Mould Line*. Master's thesis. Available at http://resolver.tudelft.nl/uuid:f4863ae4-2792-4335-b929-ff9dfdb6fed5. Sept. 2020.

[30] R. van der Pluijm. *Cockpit Design and Integration into the Flying V*. Master's thesis. Available at http://resolver.tudelft.nl/uuid:da4a8d74-32fa-45f1-9f92-d01d45fdea01. Feb. 2021.

[31] N. van Luijk. *Constrained Aerodynamic Shape Optimisation of the Flying V Outer Wing*. Master's thesis. Available at http://resolver.tudelft.nl/uuid:fc2bbe10-6796-4337-81cc-5971b324d50e. Mar. 2023.

[32] N. van Luijk. "Constrained Aerodynamic Shape Optimisation of the Flying V Outer Wing". In: AIAA AVIATION 2023 Forum, 2023. DOI: 10.2514/6.2023-3250.

[33] M. Palermo and R. Vos. "Experimental aerodynamic analysis of a 4.6%-scale flying-v subsonic transport". In: American Institute of Aeronautics and Astronautics Inc, AIAA, 2020. ISBN: 9781624105951. DOI: 10.2514/6.2020-2228.

[34] J. van Uitert. *Experimental Investigation into the Effect of Aerodynamic Add-ons on the Aerodynamic Characteristics of the Flying V*. Master's thesis. Available at http://resolver.tudelft.nl/uuid:fdfff622-792c-4d54-a048-b59abf477a11. Jan. 2021.

[35] A.J. Santoch. *Numerical Investigation of the Influence of Ground Effect on the FV Aircraft*. Master's thesis. Available at http://resolver.tudelft.nl/uuid:d34e14b2-fed5-4e4f-a448-aa0fb92e0331. Feb. 2020.

[36] R. Vos and S. Farokhi. *Introduction to Transonic Aerodynamics*. 1st ed. Dordrecht: Springer, 2015.

[37] A. R. García et al. "Aerodynamic Model Identification of the Flying V from Sub-Scale Flight Test Data". In: American Institute of Aeronautics and Astronautics Inc, AIAA, 2022. ISBN: 9781624106316. DOI: 10.2514/6.2022-0713.

[38] J. Luckring. “Reynolds number and leading-edge bluntness effects on a 65-deg delta wing”. In: 40th AIAA Aerospace Sciences Meeting & Exhibit, 2002. DOI: 10.2514/6.2002-419.

[39] M.G. Hall. “A theory for the core of a leading-edge vortex”. In: *Journal of Fluid Mechanics* 11.2 (1961).

[40] P.K. Chang. *Separation of Flow*. 1st ed. Oxford, New York: Pergamon Press, 1970.

[41] S. Pfnür and C. Breitsamter. “Leading-Edge Vortex Interactions at a Generic Multiple Swept-Wing Aircraft Configuration”. In: *Journal of Aircraft* 56.6 (2019). DOI: 10.2514/1.C035491.

[42] J. Rom. *High Angle of Attack Aerodynamics*. 1st ed. Springer-Verlag New York, Inc., 1992.

[43] E.J. Gutmark and S. A. Guillot. “Control of Vortex Breakdown over Highly Swept Wings”. In: *AIAA Journal* 43.9 (2005), pp. 2065–2069. DOI: 10.2514/1.11326 .

[44] N.C. Lambourne and D.W. Bryer. “The Bursting of Leading-Edge Vortices - Some Observations and Discussion of the Phenomenon”. In: *Aeronautical Research Council* (1962).

[45] J. Kegelman and F. Roos. “Effects of leading-edge shape and vortex burst on the flowfield of a 70-degree-sweep delta-wing”. In: 27th Aerospace Sciences Meeting, 1989. DOI: 10.2514/6.1989-86.

[46] J. Luckring. “A Survey of Factors Affecting Blunt-Leading-Edge Separation for Swept and Semi-Slender Wings”. In: 28th AIAA Applied Aerodynamics Conference, 2010. DOI: 10.2514/6.2010-4820.

[47] S. Crippa and A. Rizzi. “Numerical Investigation of Reynolds Number Effects on a Blunt Leading-Edge Delta Wing”. In: 24th AIAA Applied Aerodynamics Conference, 2006. DOI: 10.2514/6.2006-3001.

[48] J. Luckring and D. Hummel. “What was Learned from the New VFE-2 Experiments?” In: 46th AIAA Aerospace Sciences Meeting and Exhibit, 2008. DOI: 10.2514/6.2008-383.

[49] D. Hummel. “Review of the Second International Vortex Flow Experiment (VFE-2)”. In: 46th AIAA Aerospace Sciences Meeting and Exhibit, 2008. DOI: 10.2514/6.2008-377.

[50] R. Konrath, A. Schröder, and J. Kompenhans. “Analysis of PIV Results Obtained for the VFE-2 65° Delta Wing Configuration at Sub- and Transonic Speeds”. In: 24th AIAA Applied Aerodynamics Conference, 2006. DOI: 10.2514/6.2006-3003.

[51] T. Loeser, D. Vicroy, and A. Schütte. “SACCON Static Wind Tunnel Tests at DNW-NWB and 14´x22´ NASA LaRC”. In: 28th AIAA Applied Aerodynamics Conference, 2010. DOI: 10.2514/6.2010-4393.

[52] A. Schütte, D. Hummel, and S.M. Hitzel. “Numerical and experimental analyses of the vortical flow around the SACCON configuration”. In: 28th AIAA Applied Aerodynamics Conference, 2010. DOI: 10.2514/6.2010-4690.

[53] V. Kumar, A.C. Mandal, and K. Poddar. “An experimental investigation on the aerodynamic characteristics and vortex dynamics of a flying wing”. In: *The Aeronautical Journal* (2023).

[54] A. Van Meenen. *Concorde: The Ultimate Supersonic Airliner*. Unpublished. 2017.

[55] W. Chang. *Effect of Juncture Fillets on Double-Delta Wings Undergoing Sideslip at High Angles of Attack*. Master’s thesis. Sept. 1994.

[56] M. Ghoreyshi, C. Fagley, and J. Seidel. “Vortex Interaction Characteristics of Multiswept Wings at Subsonic Speeds”. In: *AIAA Journal* 61.7 (2023), pp. 2932–2947. DOI: 10.2514/1.J062605.

[57] B.W. McCormick. “A Vortex Lattice Model for Delta Wings with Bursting”. In: *SAE Technical Paper Series* 100.1 (1991), pp. 79–96. DOI: 10.4271/910991.

[58] C.H. Hsu and C.H. Liu. “Navier-Stokes computation of flow around a round-edged double-delta wing”. In: 6th Applied Aerodynamics Conference, 1988. DOI: 10.2514/6.1988-2560.

[59] H. Hoeijmakers and J. van den Berg. “Application of an Euler-equation method to a sharp-edged delta-wing configuration with vortex flow”. In: 9th Applied Aerodynamics Conference, 1991. DOI: 10.2514/6.1991-3310.

[60] S.B. Kern. “Numerical Investigation of Vortex Flow Control Through Small Geometry Modifications at the Strakewing Junction of a Cropped DoubleDelta Wing”. In: *30th Aerospace Sciences Meeting & Exhibit* (1992).

[61] D.L. Modiano and E.M. Murman. “Adaptive computations of flow around a delta wing with vortex breakdown”. In: 11th Applied Aerodynamics Conference, 1993. DOI: 10.2514/6.1993-3400.

[62] P. O’Neil, R. Barnett, and C. Louie. “Numerical simulation of leading-edge vortex breakdown using an Eulercode”. In: 11th Applied Aerodynamics Conference, 1989. DOI: 10.2514/6.1989-2189.

[63] D. Almosnino. “A Low Subsonic Study of the NASA N2A Hybrid Wing-Body Using an Inviscid Euler-Adjoint Solver”. In: 34th AIAA Applied Aerodynamics Conference, 2016. DOI: 10.2514/6.2016-3267.

[64] N.T. Frink, M. Tormalm, and S. Schmidt. “Unstructured CFD Aerodynamic Analysis of a Generic UCAV Configuration”. In: NATO RTO AVT-189 Specialist Meeting, 2011. DOI: 10.2514/6.1989-2189.

[65] S. Chakravarthy, D. Chi, and U. Goldberg. “Flow Prediction around the SACCON Configuration Using CFD++”. In: 28th AIAA Applied Aerodynamics Conference, 2010. DOI: 10.2514/6.2010-4563.

[66] A.M. Jorge. *Quantifying Wind Tunnel Effects on the Flying V*. Master’s thesis. Available at http://resolver.tudelft.nl/uuid:b9076ade-2d6e-4faf-882c-1f6115a1317a. Dec. 2023.

[67] M. Ghoreyshi et al. “Vortical flow prediction of a diamond wing with rounded leading edges”. In: *Aerospace Science and Technology* 57 (2016), pp. 103–117. DOI: 10.1016/j.ast.2016.02.011.

[68] M. Ghoreyshi et al. “Vortical Flow Prediction of the AVT-183 Diamond Wing”. In: 53rd AIAA Aerospace Sciences Meeting, 2015. DOI: 10.2514/6.2015-0292.

[69] H.A. Gonzalez et al. “Effects of Various Fillet Shapes on a 76/40 Double Delta Wing from Mach 0.18 to 0.7”. In: RTO AVT Symposium on Advanced Flow Management, 2003.

[70] H.A. Gonzalez and G.E. Erickson. “Pressure-Sensitive Paint Investigation of Double-Delta Wing Vortex Flow Manipulation”. In: 43rd AIAA Aerospace Sciences Meeting and Exhibit, 2005. DOI: 10.2514/6.2005-1059.

[71] T.A. Ghee, H.A. Gonzalez, and D.B. Findlay. “Tail Buffet Alleviation Through the Use of Wing-Strake Fillet Shapes”. In: *Journal of Aircraft* 39.1 (2002), pp. 100–108. DOI: 10.2514/2.2901.

[72] Faculty of Aerospace Engineering. *Low Turbulence Tunnel*. URL: https://www.tudelft.nl/lr/organisatie/afdelingen/flow-physics-and-technology/facilities/low-speed-wind-tunnels/low-turbulence-tunnel (visited on 02/19/2024).

[73] G.J. de Zoeten, C. Varriale, and R. Vos. “Flight Performance Evaluation of the Flying-V”. In: AIAA AVIATION 2023 Forum. Nr. 2023-3484, 2023. DOI: 10.2514/6.2023-3484.

[74] R. DeLoach. “The Modern Design of Experiments: A Technical and Marketing Framework”. In: 21st AIAA Advanced Measurement Technology and Ground Testing Conference, 2000.

[75] J.B. Barlow, W.H. Rae, and A. Pope. *Low-speed Wind Tunnel Testing*. 3rd ed. John Wiley & Sons Inc., 1999.

[76] C. Presas et al. “Flow Field Analysis of Vortex Interactions on Multi-Swept Wing Configurations”. In: AIAA SciTech Forum, 2024. DOI: 10.2514/6.2024-0904.

[77] National Aeronautics and Space Administration. *Laser Doppler Velocimetry*. Ed. by N. Hall. URL: https://www.grc.nasa.gov/www/k-12/airplane/tunldv.html (visited on 03/07/2024).

A

Velocity Contours

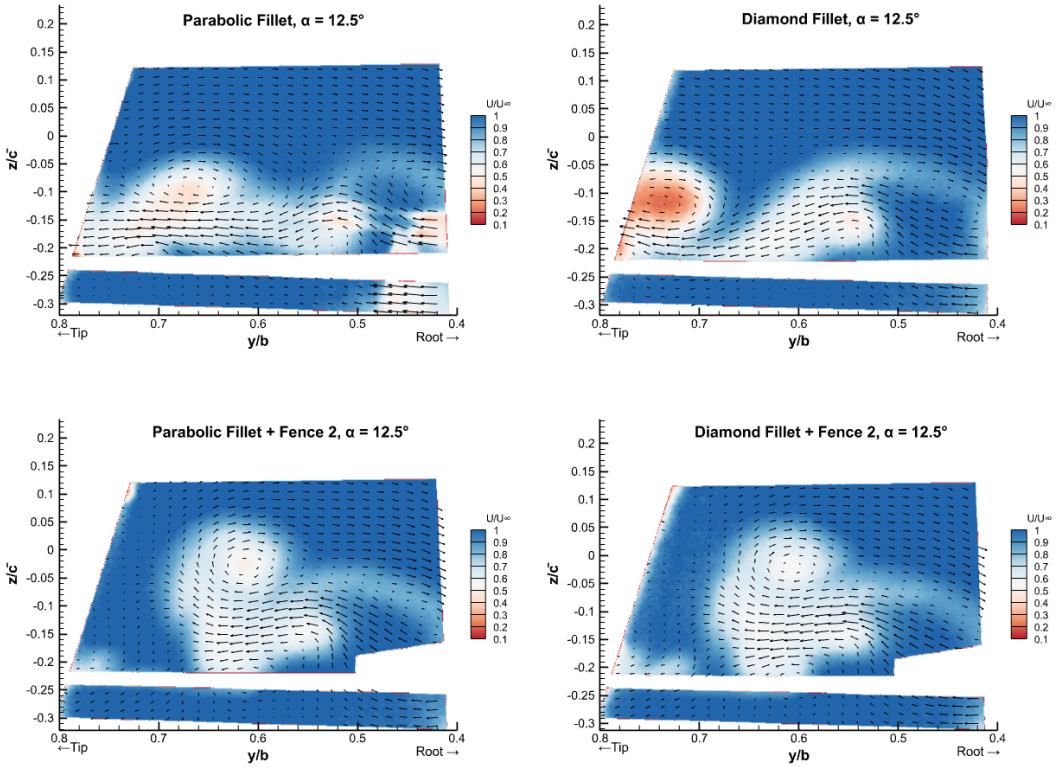

Figure A.1: Velocity contour at $\alpha = 12.5°$

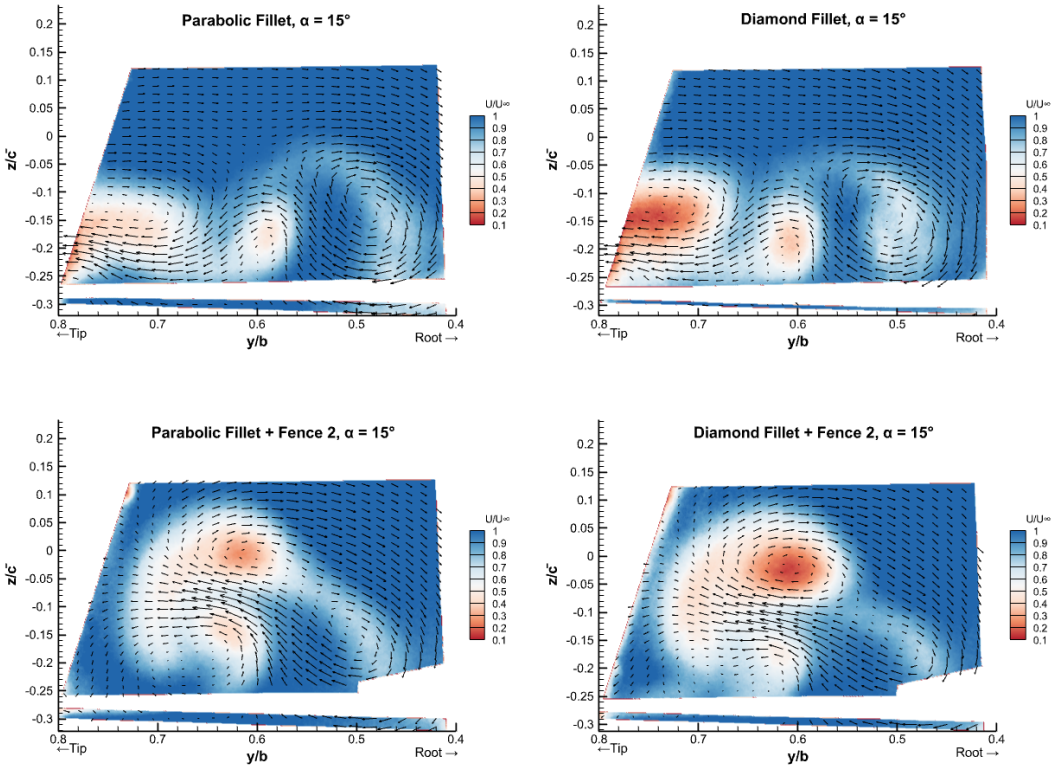

Figure A.2: Velocity contour at $\alpha = 15°$

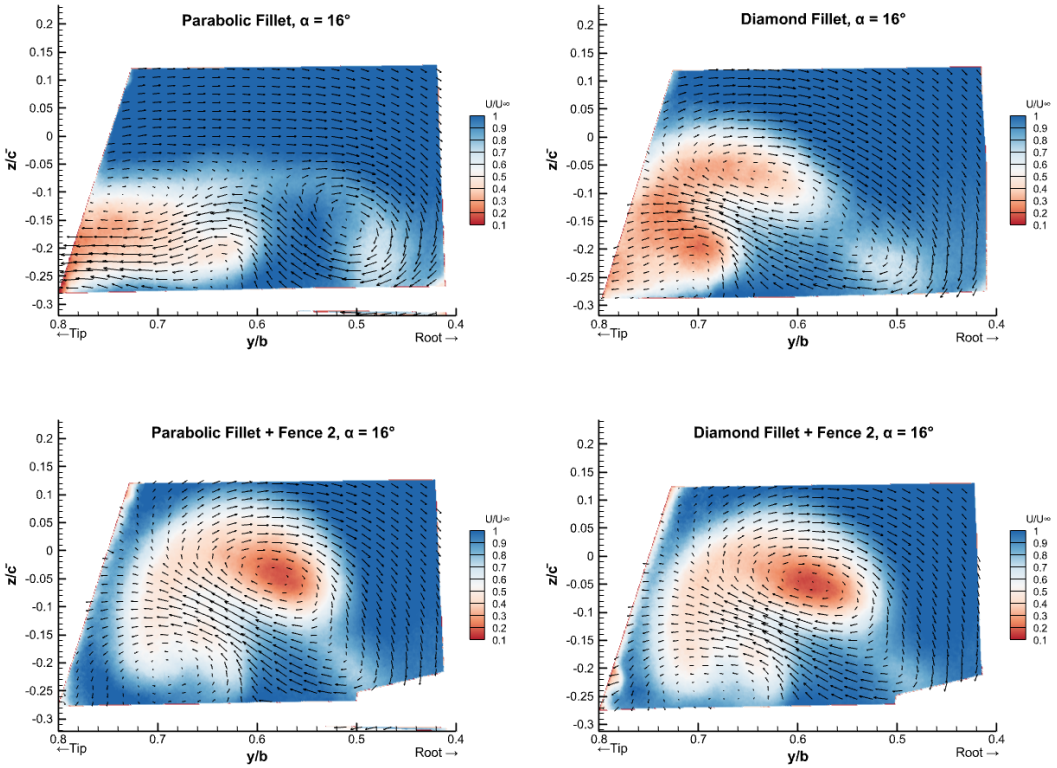

Figure A.3: Velocity contour at $\alpha = 16°$

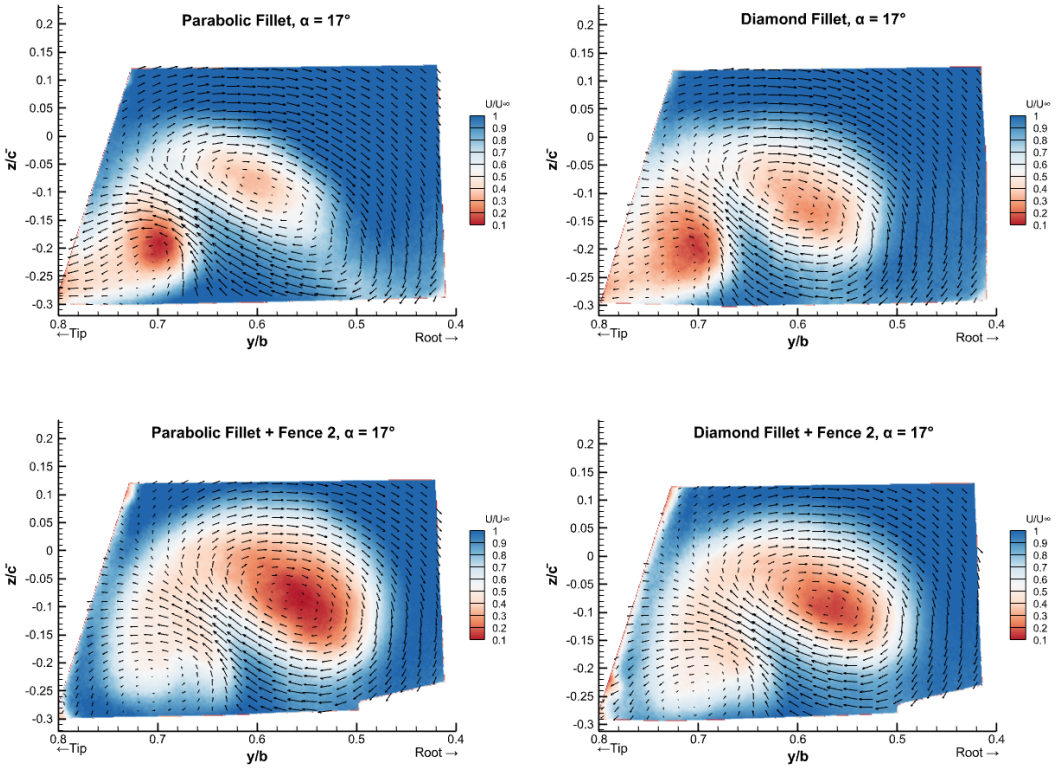

Figure A.4: Velocity contour at $\alpha = 17°$

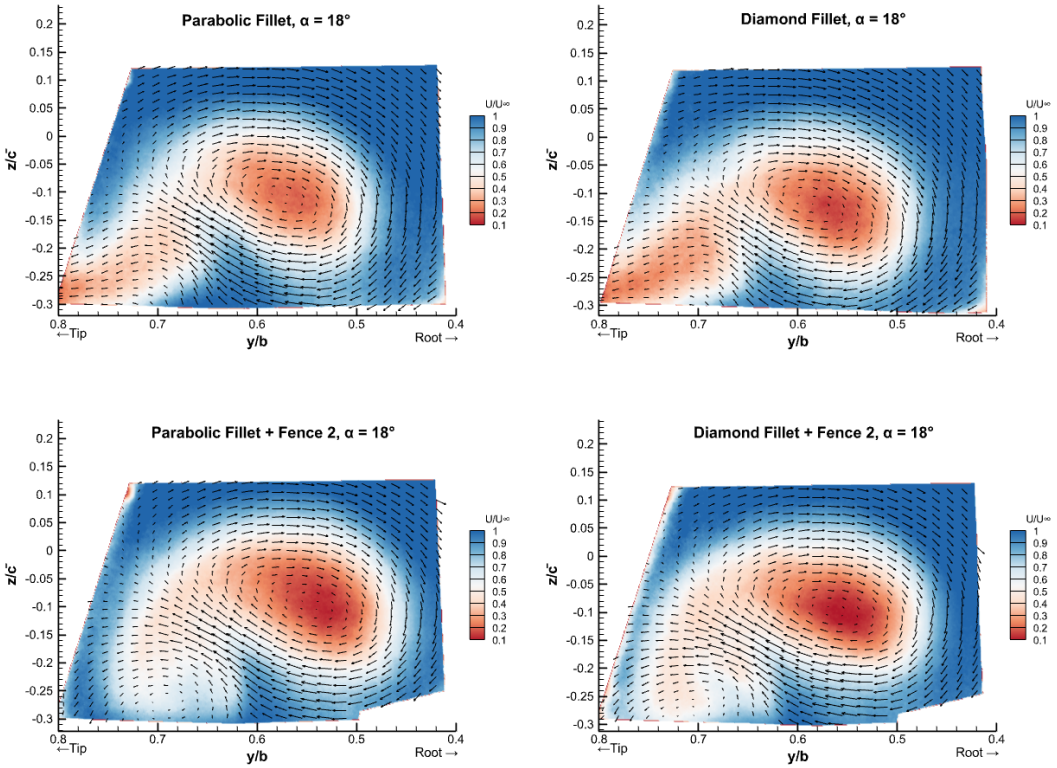

Figure A.5: Velocity contour at $\alpha = 18°$

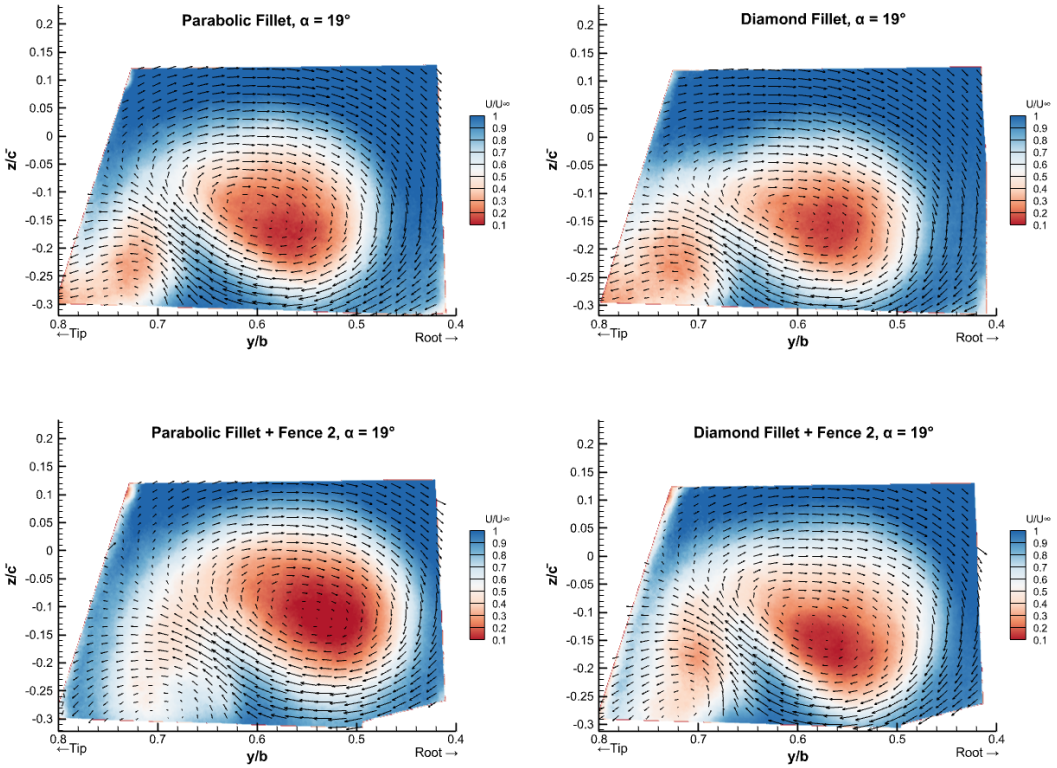

Figure A.6: Velocity contour at $\alpha = 19°$

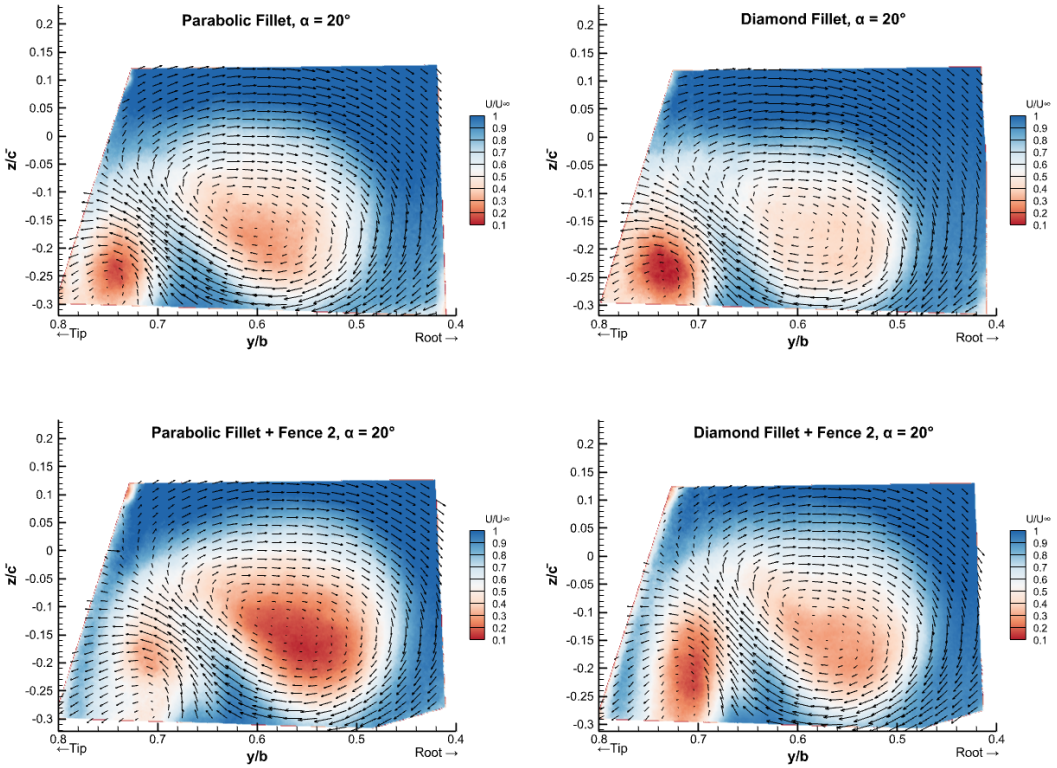

Figure A.7: Velocity contour at $\alpha = 20°$

B

Vorticity Contours

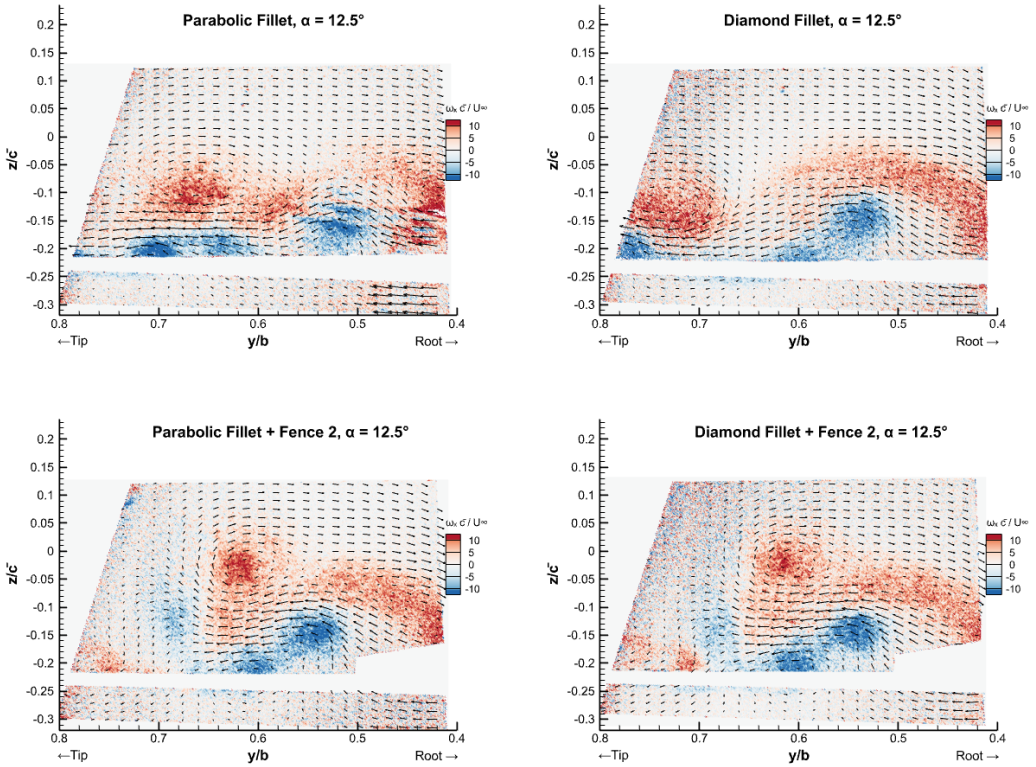

Figure B.1: Vorticity contour at $\alpha = 12.5°$

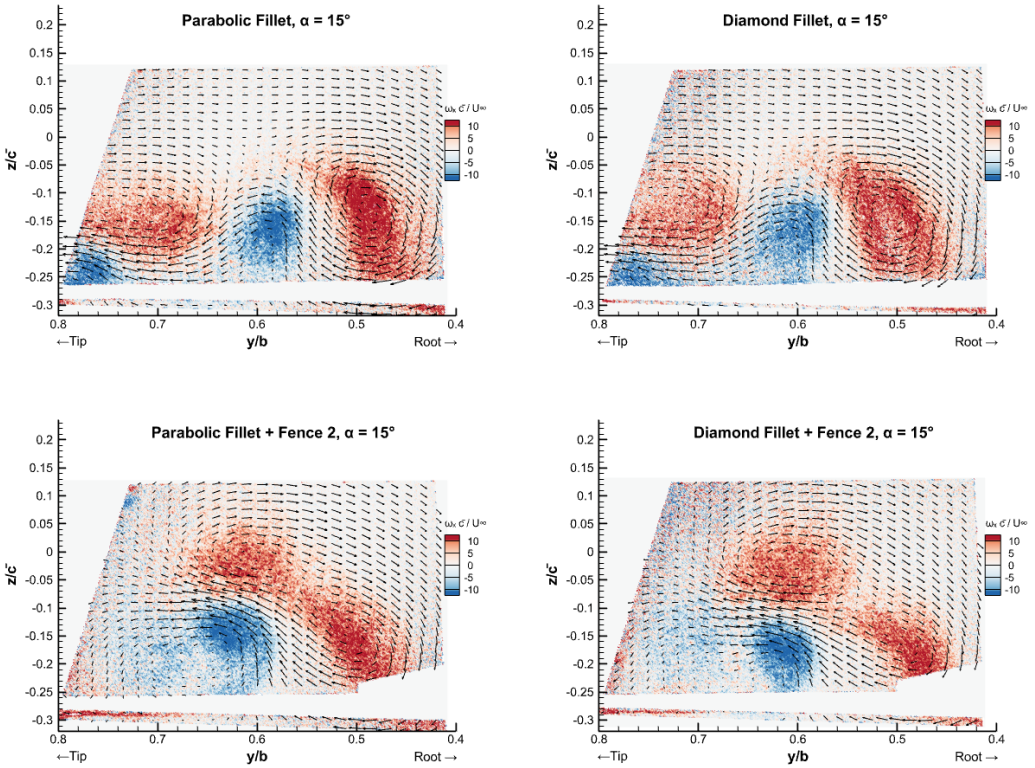

Figure B.2: Vorticity contour at $\alpha = 15°$

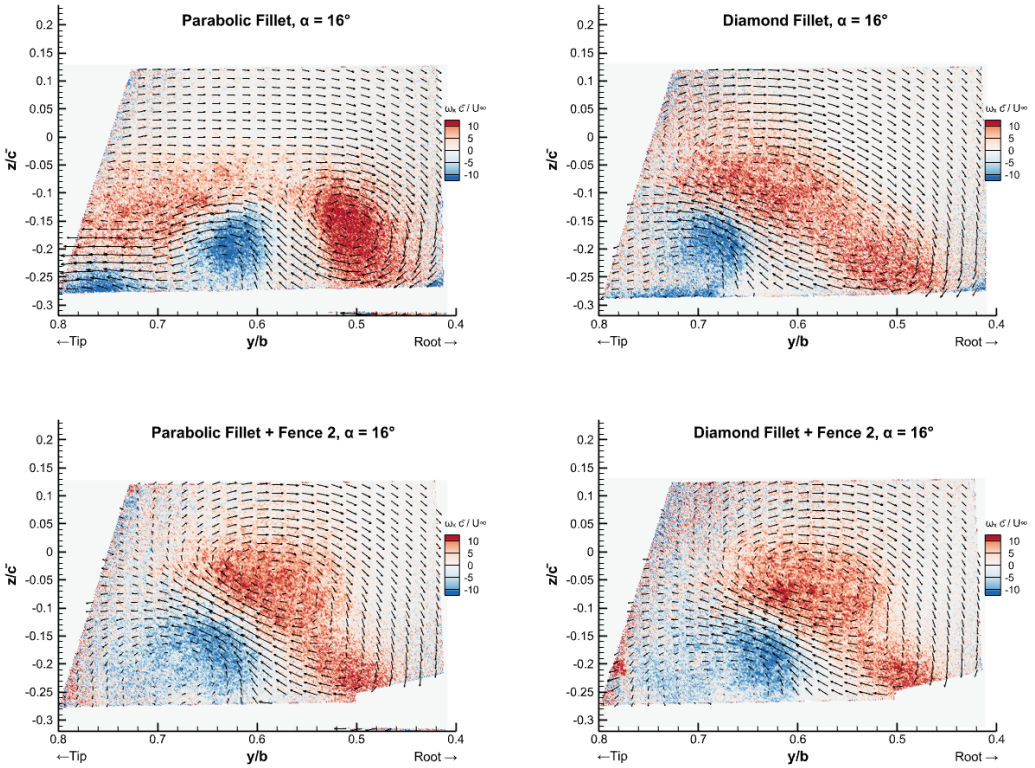

Figure B.3: Vorticity contour at $\alpha = 16°$

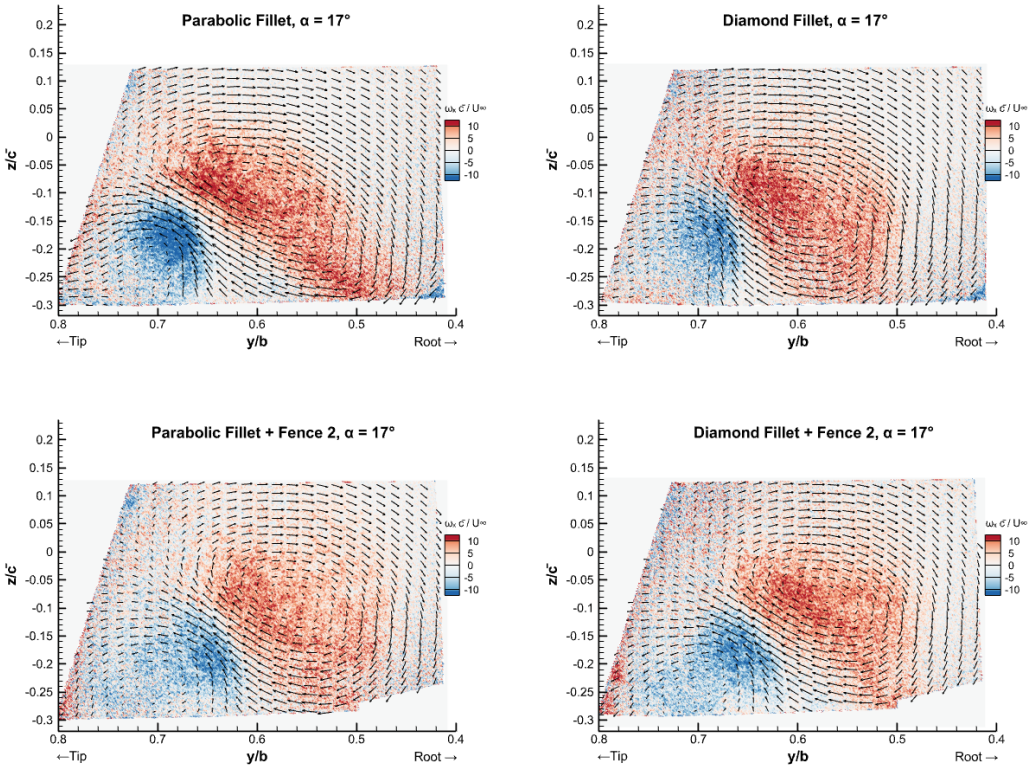

Figure B.4: Vorticity contour at $\alpha = 17°$

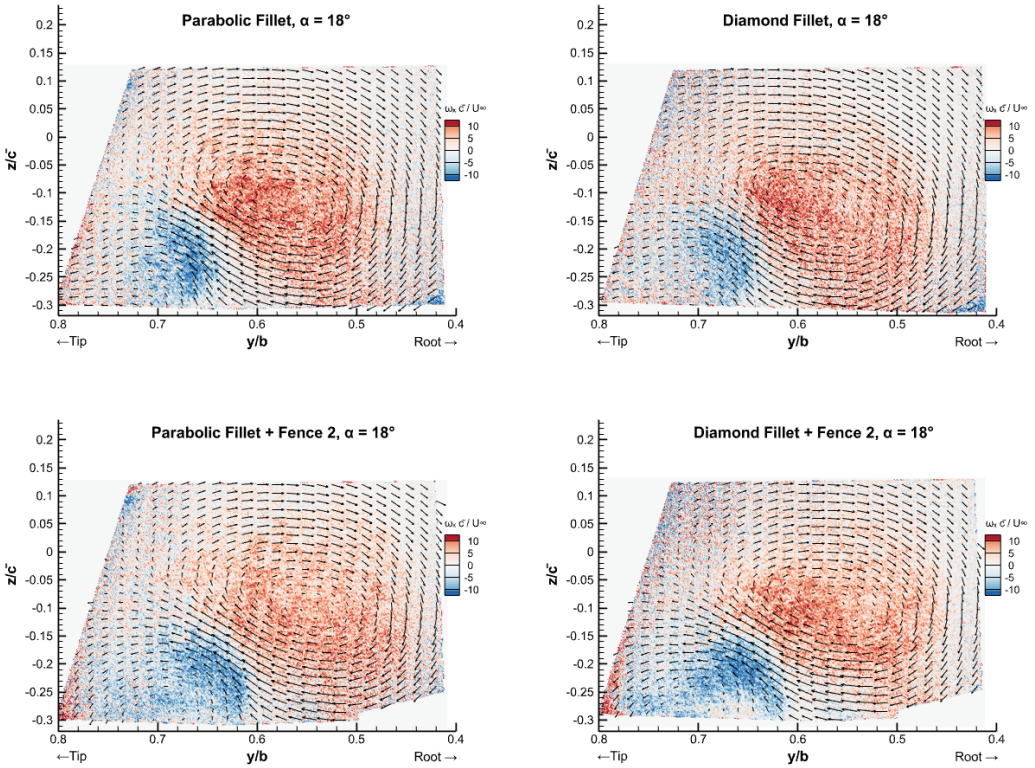

Figure B.5: Vorticity contour at $\alpha = 18°$

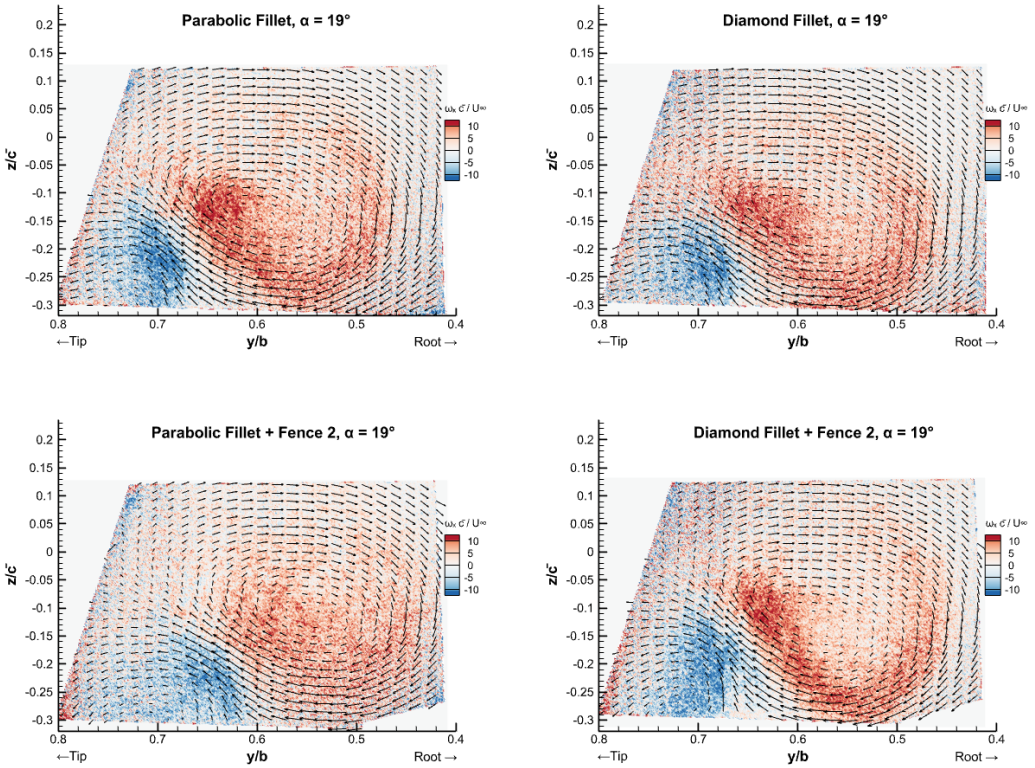

Figure B.6: Vorticity contour at $\alpha = 19°$

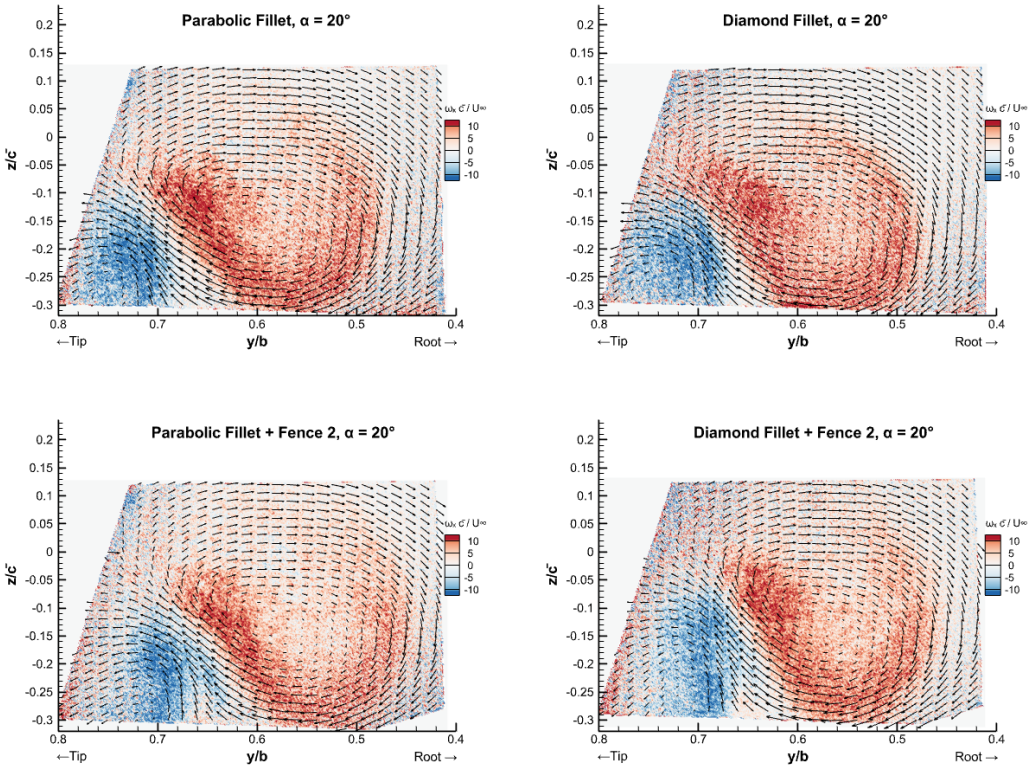

Figure B.7: Vorticity contour at $\alpha = 20°$